Imaging Electron-Driven Dynamics in Dissociative Electron Attachment to Gas Molecules

by

Ali Moradmand

A dissertation submitted to the Graduate Faculty of
Auburn University
in partial fulfillment of the
requirements for the Degree of
Doctor of Philosophy

Auburn, Alabama
August 3, 2013

Keywords: Dissociative electron attachment, spectrometer, momentum, molecule

Approved by

Michael Fogle, Assistant Professor of Physics
Allen Landers, Carr Professor of Physics
Ed Thomas, Professor of Physics
Stuart Loch, Associate Professor of Physics
George T. Flowers, Dean, Graduate School

Abstract

The design and construction of a new ion-momentum spectrometer for the study of electron-molecule interactions at Auburn University (AU) is detailed with emphasis on the phenomenon of dissociative electron attachment (DEA). Applications of the DEA process to varying fields are discussed within the background of molecular theory and the current state of experimental progress. Technical challenges associatied with the construction of a supersonic gas jet, pulsed electron beam, a COLTRIMS-like spectrometer, and list-mode data acquisition are detailed, including demonstrations of the simulation and analytic methods employed. The present apparatus is designed to provide three-dimensional data on angle-resolved fragment momenta resulting from DEA and other electron-molecule interactions. Initial data on the dissociative ionization of methane are shown for calibration. Data on DEA in O_2, CO_2, and N_2O are shown, with comparison to similar measurements and recent theoretical collaborations with Lawrence Berkeley National Laboratory (LBNL). Improvements over existing experimental data are demonstrated, while surprising results in the angular distributions of anion fragments are observed. Finally, future work with the apparatus including a focus on more complex molecular targets is discussed.

Dedicated to my parents,
Bizhan and Mehri Moradmand

تقدیم به پدر و مادرم،
بیژن و مهری مرادمند.

Acknowledgments

I believe that nothing worthwhile or meaningful is done completely alone. It is impossible to delineate in a finite space all the ways, both professional and personal, that numerous uncredited scientists, friends, and family have contributed to this work; I hope that my appreciation is apparent to all these individuals.

My first thanks go to my advisor, Mike Fogle, whose patience, persistence, and knowledge have been both reliable and encouraging throughout my time at Auburn. Professor Allen Landers' intuition and experience have also been indispensible to the progress achieved in this work. The additional members of the thesis committee, Stuart Loch, Ed Thomas, and Konrad Patkowski, gave many insightful comments and suggestions on the text, and I believe the result is much better because of them. Joshua Williams provided an unmatched combination of friendship and scientific expertise, and much of the early setup of the detection system was due to his efforts and guidance. I would further like to thank Max Cichon for his technical assistance and instructive yelling, Matt and Althea ArchMiller for giving me a place to stay (even as I write this), as well as many other friends and family who are too numerous to name, but too important to forget.

However, the most important people in my life by far are my parents. So much of life depends on good fortune, and in this respect I have been luckier than almost anyone. Their endless support and love has made it almost impossible for me to fail, and I owe everything to them. I wish everyone could be so lucky.

Table of Contents

List of Figures

List of Tables

1 — Introduction and Background

”These are the theories of lunatics.”

–Dennis Reynolds

In recent years, low energy electron interactions have been of interest to varying biological and technological applications. From the physics of atmospheric interactions to surface science and molecular biology, electron-driven processes have been the subject of extensive study. Physicists, chemists, biologists, and engineers are seeking to understand the mechanisms of breakups and rearrangments in a wide variety of molecules and the changes in material properties associatied with these transformations.

This experimental study centers around the investigation of the phenomenon of dissociative electron attachment (DEA). After completion of the construction of a unique apparatus to study electron-molecule interactions, the apparatus was calibrated with observation of dissociative ionization of methane (CH_4) . The subsequent DEA experiments included molecular targets of O_2, CO_2, and N_2O. In collaboration with a parallel DEA experiment and theoretical work at Lawrence Berkeley National Laboratory (LBNL) , several deviations from accepted theory were discovered.

This chapter will attempt to illuminate the motivation and significance of these interactions in preparation for the discussion of the specific case of electron attachment to the molecular species studied in this work. In the upcoming sections, a discussion of the purpose and applications of the research will be followed by an abbreviated treatment of the theory of molecular orbitals (MOs). Next, a more focused discussion of the interactions between electrons and molecules is presented, followed by a rough timeline of the theoretical and experimental achievements in the field, which will lead in to the description of this work's apparatus in the next chapter. Chapter 2 will discuss in detail the apparatus and the challenges involved in the design, construction, and operation of the experiment. Chapter 3 focuses on the preparatory computer simulations that determine a starting point for the experimental parameters. Included therein are simulations of the momentum distributions of anions and the ion optics used to detect them. Chapter 4 reports the data on the dissociative ionization of methane, followed by the DEA experiments on the three targets mentioned above. In each case, a discussion of either the comparison to existing results or to theoretical calculations is included. The final chapter summarizes the work and provides some insight into probable future studies with the apparatus.

1.1 Motivation and Applications

The study of low energy electron interactions with molecular targets is important because many processes beginning with higher energy photons or electrons produce secondary electrons of much lower energy which go on to interact with the surrounding material in ways that affect the material's composition and properties. Figure 1.1 qualitatively shows the effect of primary ionization in molecular targets. While cross sections for ionization and excitation are larger at higher electron energies, the secondary electrons produced from the initial ionization events are typically of low energy (<20 eV). Since the dissociative electron attachment (DEA) resonances exist at these lower energies, the ion yields at low energy from secondary electrons become dominated by DEA. For example, calculations of electron production from primary ionizing radiation in water show that the most probable energy for the secondary electrons is 9-10 eV.[1]

These low energy electron-molecule interactions turn out to have great importance in material science and engineering. The method of electron beam lithography, used to create

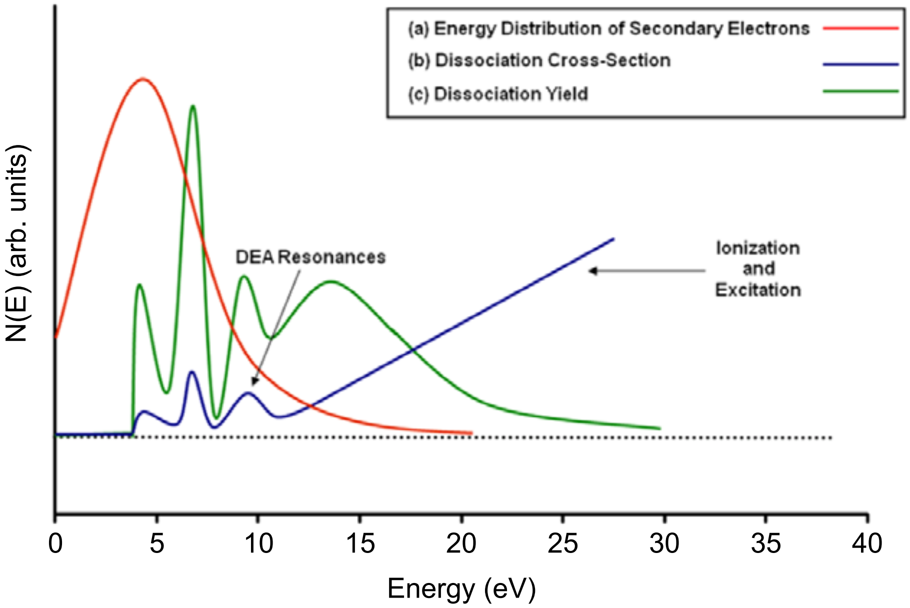

Figure 1.1: Schematic of (a) energy distribution of secondary electrons generated during a primary ionizing event; (b) the cross section for electron-induced dissociation for a typical molecule; (c) dissociation yield as a function of electron energy for a typical molecule.[2]

nanoscale structures in a resist-covered surface for use in semiconductor manufacturing, uses a high energy beam of electrons which inelastically scatter with the surface to produce secondary electrons with a wide range of energies, some of which then undergo dissociative attachment with the surrounding material.[3,4] Electron beam irradiation in the presence of polyfunctional monomers has been shown to modify properties such as tensile strength and modulus in rubbers.[5,6] Mass spectrometry has also been used to study degradation of polyethylene layers from low energy electrons leading to surface emission of anions which have been attributed to DEA and dipolar dissociation interactions.[7] Dissociative attachment has also been credited with the enhancement of the formation of silicon dioxide layers through electron impact with silicon in the presence of molecular oxygen.[8] Some exciting research involving the attachment of organic layers to semiconductor surfaces using electron induced interactions could have striking implications for the manufacturing of microelectronics.[9–11]

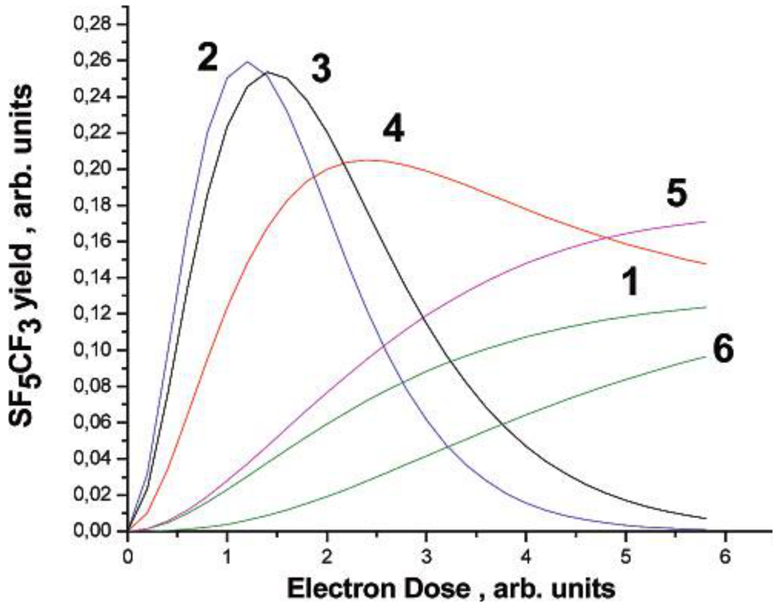

Figure 1.2: Modeled yield of SF_5CF_3 from electron irradiation of condensed mixtures of SF_6 and CF_4 attributed to DEA from 4-10 eV electrons for six different sets of the rate constants for the reactions involved in the formation of SF_5CF_3. The rate constants are α, β, κ, and γ, where α and β are rate constants for the formation of CF_3 and SF_5 radicals, respectively, while κ and γ are rate constants for formation and destruction of SF_5CF_3, respectively.[12]

In the environmental sciences, the low-energy electron interactions have a role in the disposal of nuclear and chemical wastes and ozone depletion in the stratosphere as well as contributions to greenhouse gas production. Low energy electrons can form radicals of H_2O which interact to produce corrosive species like H_2O_2, which can be harmful to cooling, storage, and waste disposal of nuclear energy byproducts.[13,14] Research on the correlation of cosmic rays to the reduction of ozone in the Earth's upper atmosphere indicate that electron attachment may contribute to the production of chlorine atoms from chlorofluorocarbons (CFCs) which go on to destroy ozone molecules.[15–18] The most potent greenhouse gas ever discovered in the atmosphere, SF_5CF_3, was observed via gas chromatograph–mass spectrometry[19] and later shown to be a product of DEA through irradiation of a condensed film of SF_6 and CF_4 (see Fig. 1.2).[12] Clearly, low energy electron interactions play a vital role in the understanding of the environmental impact of anthropogenic substances.

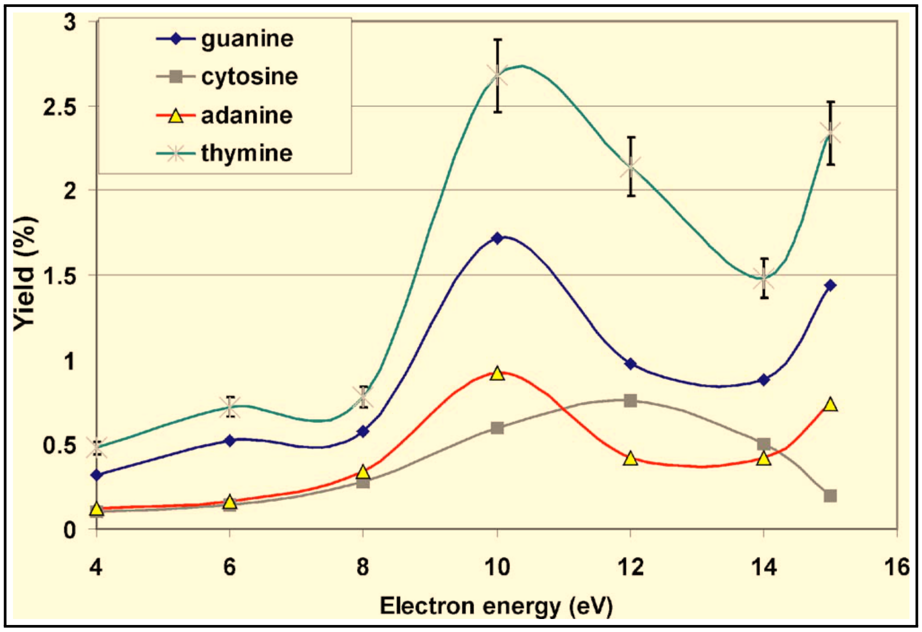

Figure 1.3: Electron attachment yield as a function of electron energy for the four DNA-bases.[20] Recent research indicates that electrons with energies below ionization thresholds can induce ion formation and strand breaks in DNA and other biomolecules. These effects have important implications for the effect of primary radiation on biological tissue.

Some of the most significant applications of these processes are in the biological sciences, where specifically DEA has been shown to play a role in the mutagenic effects of radiation therapy, strand breaks in DNA, and modification of biomaterials using electron beam irradiation. Discoveries of the significance of dissociative attachment in biomolecules have been partially responsible for a resurgence of interest in low energy electron interactions both in complex organic systems and in fundamental molecules. In recent years, single-strand breaks and double-strand breaks (SSBs and DSBs) in DNA have been understood to be caused by the low energy, secondary electrons produced by direct ionization of living cells from exposure to ionizing radiation.[21–26] Such strand breaks have been specifically attributed to DEA through electron beam-stimulated desorption of anions from thin films of DNA in the low electron energy regime.[27–31] Interestingly, these low energy secondary electrons are the most abundant secondary species created from primary ionization, with an estimated quantity of 5×10^4 electrons per MeV of primary radiation, and have also been shown to be responsible for site-specific fragmentation of DNA molecules.[20,32,33] Other studies have demonstrated

DEA in molecular constituents of DNA and RNA such as uracil[34] and phosphate groups.[35] Figure 1.3 shows, for example, the electron attachment yields from 4-15 eV electrons to the four DNA nucleobases. Even the effectiveness of radiation therapy has been researched through the irradiation of solid DNA films with electrons of energy as low as 1 eV, where SSBs are thought to proceed only via DEA.[23, 36, 37]

Other varied applications of the study of low-energy electron interactions include electron-beam irradiation of ground beef to prevent microbial growth,[38] irradiation of mail to neutralize volatile organic materials,[39] and numerous astrophysical and atmospherical considerations. The synthesis of pre-biotic molecular species has been observed from simple molecular surface ices to be driven by low-energy electron-driven interactions,[40] and measurements of Titan's ionosphere indicate the importance of negative ions in the formation of the hydrocarbon species which partly characterize that moon's atmosphere.[41]

1.2 Molecular Orbital Theory

The basics of the theory of molecular orbitals (MOs) and bonding will be discussed here in order to provide context for the data and introduce the notation and terminology commonly used in the literature for molecular interactions. The basic theory of bonding, particularly in diatomic molecules, will be followed by a description of molecular states and the group theoretical formulation of molecules which is based on symmetry and extensible to more complicated polyatomic systems.

1.2.1 Bonding

When two separate atoms approach from a large distance, the interaction between their electrons and their nuclei becomes non-negligible, and each electron is subject to the attractive potential of its own nucleus as well as the nucleus of the other atom and also repulsive potentials from the electrons in both atoms. Essentially, bonding occurs when the total attractive potentials overcome the repulsion, and the total energy of the atoms bound together

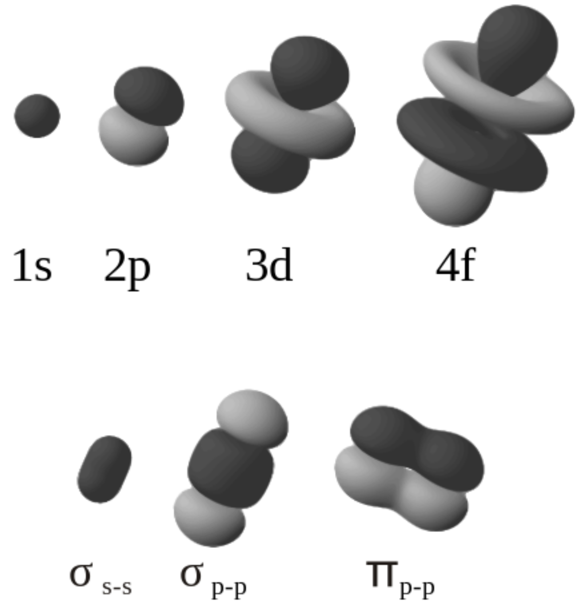

Figure 1.4: Atomic orbitals (top row) and the resultant molecular orbitals (bottom row) formed by the combination of s and p orbitals.

is lower than the energy of the atoms separately. Since the Coulomb potential between the charges is a function of distance, the total electronic energy will depend on the internuclear distance, and a bound state may exist for a stable molecular wavefunction in a limited range of internuclear distances, which determines the bond length of the molecule. In more complicated polyatomic molecules, the interaction between individual electron orbitals can affect the stability of the molecule in other parameters, such as bond angle, which also affect the geometry of the stable molecule.[42]

For individual electron orbitals in a molecule, electrons are characterized by the types of bonds they occupy, and these bonds (in molecular orbital theory) are formed in the molecule by linear combinations of the individual atomic orbitals. Since the atomic orbitals have different angular momenta $(s, p, d, f, \ldots)$, the symmetry and degeneracy of the resulting molecular orbitals depends on how these atomic orbitals interact. Figure 1.4 shows four atomic orbitals in the top row and three molecular orbitals formed by combinations of s and p atomic orbitals in the bottom row. The internuclear axis is along the longitudinal axis of the σ_{p-p} bond. When two s orbitals combine, they form a σ bond which has cylindrical

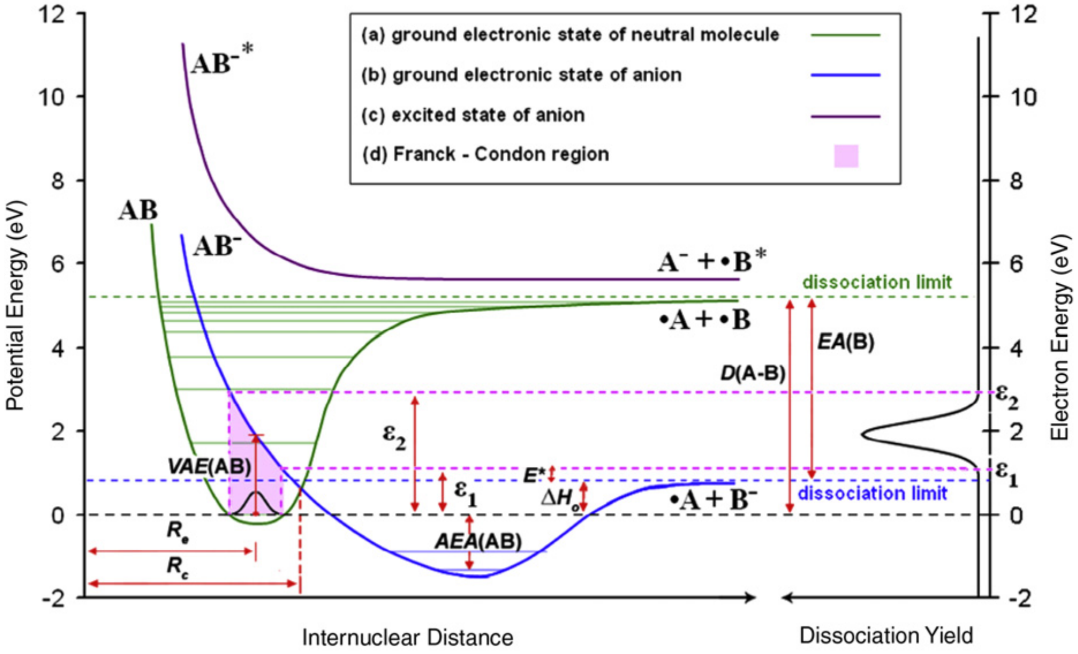

Figure 1.5: Potential energy curves for the ground state of a molecule AB (green), its anion following electron attachment (blue), and a dissociative excited state (purple). The horizontal green lines show the vibrational levels in the ground electronic state, and on the right is the dissociation yield from attachment as a function of the incoming electron energy. The energies ε_1 and ε_2 are the limits in the Franck-Condon region for the transition to the anion state. E^* is the excess energy left over from the dissociation of the anion which is partitioned between the fragments. ΔH_0 is the threshold energy required to form the fragmented anion from its neutral target state.[2]

symmetry. Two p orbitals can combine to form a σ bond or a π bond, depending on whether the p orbitals were aligned parallel to the bond axis (i.e., p_z) or perpendicular to the bond axis (i.e., p_x or p_y). The σ_{p-p} bond is, again, cylindrically symmetric, but the π_{p-p} bond is not, and these symmetries affect the symmetry of the overall molecular state.[43]

For a particular electronic state, there are also multiple quantized vibrational levels which become closer in energy separation as their energy approaches the dissociation energy of the molecule (see Fig. 1.5). This is as opposed to the harmonic oscillator model, in which the vibrational levels are evenly spaced by $\hbar\omega$, so the anharmonic potential of the molecule is typically approximated with functions such as a Morse, Lennard-Jones, or Stockmayer potential. The zero-point motion of the lowest vibrational state means that the dissociation energy of the molecule is slightly less than the depth of the potential well in which the state resides.[42] In the present experiment, it will commonly be assumed that the molecules begin in their ground vibrational state, the experimental reason for which will be made clearer in the next chapter.

For simplicity, the common method of the *Born-Oppenheimer Approximation* is utilized, which assumes that electronic transitions happen on time scales much shorter than that of nuclear vibrational or rotational motion. In this way, electronic transitions can be treated as uncoupled to the nuclear motion, and potential energy curves can be calculated by using a static nuclei model. Of course, for a given molecule, various potential curves exist due to the different electronic configurations which are possible, and transitions between the configurations via vertical, or *Franck-Condon transitions*, often cause the molecule to enter a non-stationary state, at which point it can dissociate into atomic constituents, as is the case with dissociative attachment. Figure 1.5 shows the different molecular states for a hypothetical molecule AB and the energy of an incoming electron attaching to the molecule to form a negative ion which dissociates. In Fig. 1.5, the excess energy E^* is left over after the anion's dissociation and gives the translational and internal energy of the resulting fragments. This energy plus the thermodynamic threshold energy, ΔH_0, equals the minimum energy required for the initial transition.

In reality, the potential energy curves are often surfaces dependent on multiple *reaction coordinates*,indexreaction coordinate and their shape is not always known. However, the origin of wave packets on these surfaces and their motion across them is integral to the discussion of dissociation dynamics, and the proximity of different states also plays a role in their shape and the resulting dissociative motion. The results of experiments (such as the one in this work) and the theoretical basis for the PE surfaces are highly coupled in the ultimate understanding of the interaction.

1.2.2 Molecular States

Molecular energy levels are commonly identified by their quantum numbers using notation specific to the *point group* implied by the structure of the molecule. This will be discussed further in the following section, but for homonuclear diatomic molecules and symmetric linear molecules with an inversion center, the *molecular term symbol* notation is used to designate the electronic state with the general form:

$$^{2S+1}\Lambda^{(+/-)}_{\Omega,(g/u)} \tag{1.1}$$

where S is the total spin quantum number, Λ is the absolute value of the projection of the orbital angular momentum along the internuclear (bond) axis, Ω is the projection of the total angular momentum along the axis, (g/u) represents *gerade* (even) or *ungerade* (odd) parity with respect to the inversion center, and $(+/-)$ represents even or odd symmetry with respect to reflection through a plane containing the bond axis. By analogy with the atomic term symbols $(s, p, d, f, \ldots)$, Λ may take on the symbols $(\Sigma, \Pi, \Delta, \Phi, \ldots)$ corresponding to orbital angular momentum quantum numbers of (0, 1, 2, 3, ...), respectively. The $(+/-)$ superscript denotes whether the total electronic wavefunction, including spatial and spin parts, is symmetric (+) or antisymmetric (-) with respect to reflection through a plane containing the two nuclei. From the perspective of the electronic wavefunction, this means that if two electrons in non-closed shells occupy a linear combination of two states in which their spins are aligned parallel, so that $S = 1$ (triplet state), swapping their m_l quantum numbers so that a π_+ orbital becomes π_- (and vice versa) would cause the wavefunction to pick up a factor of (-1), giving it a superscript of (-), and no change for a superscript of (+). This operation is equivalent to a reversal of the "direction of rotation" for the orbital angular momentum of the suborbital. Since states with $\Lambda \neq 0$ always contain degenerate states of both (+) and (-) parity, there can always be constructed a state consisting of a linear combination (due to orbital degeneracy) of both (+) and (-) states, so that the label

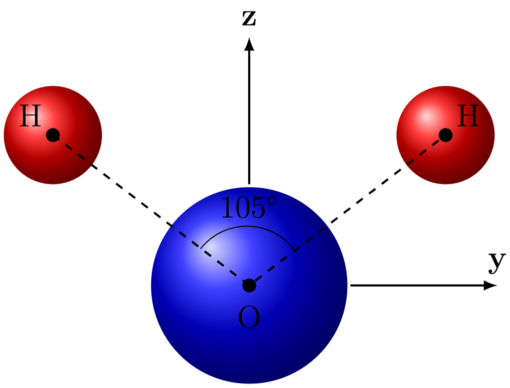

Figure 1.6: Structure of a water molecule. The x axis points out of the plane of the figure.

is typically left off. The (g, u) subscript is only used for homonuclear diatomic molecules and molecules with an inversion center, since asymmetric molecules with no inversion center have no definite parity in their electronic wavefunctions.[44]

The specific example of term symbol determination for diatomic oxygen is provided in Appendix A.

1.2.3 Symmetry and Group Theory

For molecules that are not diatomic or linear with an inversion center, inspection of the molecule's structure through the lens of group theory and symmetry considerations can offer insight into both the electronic structure and the transitional activity of the molecule. If the bond structure of a molecule is known, the effect of various symmetry operations on the molecule (e.g., rotation, planar reflection, inversion) can be determined and the molecule can be assigned to a *point group*. A point group is a set of symmetry operations that leave a point (the origin) unchanged and is useful for characterizing a three-dimensional structure based on its invariance under those symmetry operations. Common symmetry operations include the rotation through an angle $\frac{2\pi}{n}$ (where n is an integer) C_n, reflection symmetry through a horizontal or vertical plane σ_h or σ_v, inversion i, and the identity operator E. A molecule such as water, shown in Figure 1.6, is invariant under C_2 rotation about the z axis, $\sigma_v(xz)$ (reflection through the vertical plane perpendicular to the figure), $\sigma_v'(yz)$ (reflection

C_{2v}	E	C_2	$\sigma_v(xz)$	$\sigma_v'(yz)$		
A_1	1	1	1	1	z	x^2, y^2, z^2
A_2	1	1	-1	-1	R_z	xy
B_1	1	-1	1	-1	x, R_y	xz
B_2	1	-1	-1	1	y, R_x	yz

Table 1.1: Character table For the C_{2v} point group. The symbols in the first column (A_1, A_2, ...) are irreducible representations in the point group, which also correspond to molecular states formed by combinations of atomic orbitals. Each representation transforms uniquely, either symmetric (1) or antisymmetric (-1), under each of the four symmetry operations of the group, as do the molecular states associated with each representation.

through the plane of the figure), and the identity operation E(surprise). This places the H_2O molecule in the C_{2v} point group.

Symmetry operations are represented by matrices, but the form of the matrices depends on the basis which is used to construct the functions on which the matrices operate. For molecular orbitals, the bases can consist of atomic orbital functions, coordinates, or even vibrational modes in the case of vibrational states. The set of matrices implied by a particular basis is called a *representation*, and since transformations can be applied to a basis set to construct a different basis, different representations are possible for a given point group. Representations are also denoted by their dimension, meaning the dimension of the matrices in that representation. For each point group, there are several representations denoted as *irreducible*, which means that the matrices' dimensions cannot be further reduced via a similarity transformation. These special representations are given unique symbols and are used to characterize a point group in its *character table*. The character table lists the representations for the point group, the symmetry operations relevant to it, and the *character* of each symmetry operation for each representation. The character is equal to the trace of a matrix (the sum of the diagonal elements) in a given representation and the set of characters gives information about the way functions transform under a given operation.[43,45,46]

Table 1.1 is the character table for the C_{2v} point group, to which the water molecule belongs. The four classes of symmetry operations are listed in the top row and the four irreducible representations are listed in the left column. On the right two columns are functions which transform according to the representation in their respective rows. The first representation, A_1, is called the *totally symmetric representation* because its character is +1 for all four operations. This means that functions which correspond to that row are invariant under the four symmetry operations. A character of -1 would mean that functions which transform according to that representation are antisymmetric under that operation. Every point group has a totally symmetric representation which is listed first in the table. One-dimensional representations are labeled A or B corresponding to symmetry or antisymmetry under the C_2 rotation, respectively. Representations of higher dimensionality are labeled with E for two-dimensional or T for three-dimensional representations. In the case of the water molecule, one of the molecular orbitals formed is from the combination of $2s$ orbitals from the oxygen atom and the $1s$ orbitals on the two hydrogen atoms. This is symmetric under all the operations of the C_{2v} group, so it transforms under the A_1 representation. For this reason, that molecular orbital is labeled with the lower case $2a_1$. Similarly, the p_x orbital is antisymmetric under C_2 but symmetric under $\sigma_v(xz)$, so it is called the $1b_1$ orbital. These orbitals are perturbed by the molecular bonding, but their symmetry remains the same, so these labels are convenient for describing bonding orbitals in a molecule. For water, the full ground state configuration would be written:

$$(1a_1)^2(2a_1)^2(1b_2)^2(3a_1)^2(1b_1)^2 \tag{1.2}$$

Again, much information can be obtained from character tables which is outside the scope of this discussion, including infrared and Raman activity, transition states, and vanishing integrals based on state symmetries.

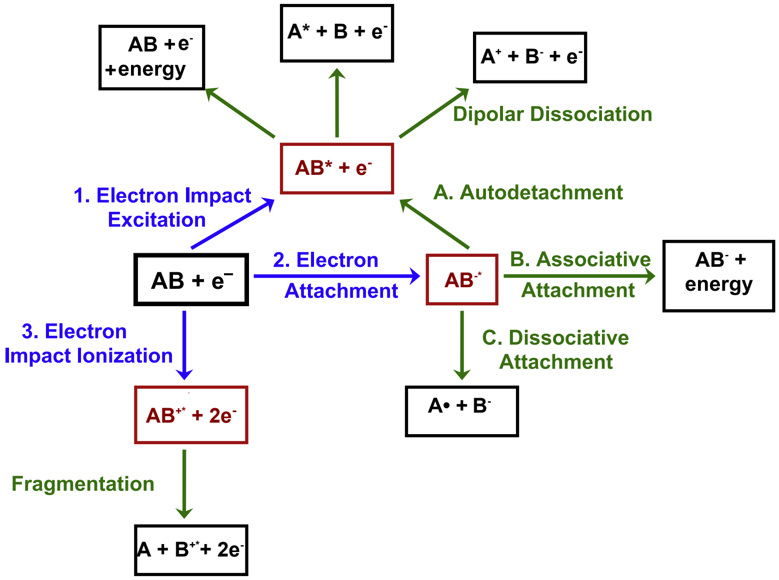

Figure 1.7: Diagram of electron-molecule interaction pathways from the initial system $AB + e^-$ (projectile and freed electrons are omitted across arrows). This work focuses on the dissociative attachment pathway, 2(C).[2]

1.3 Electron-Molecule Interactions

In a molecule, the additional degrees of freedom provided by the polyatomic system afford numerous interaction possibilities which can proceed via several pathways to produce positive or negative ions, electronically excited neutral molecules and atoms, vibrationally excited molecules, energy, and ground state neutral fragments. Figure 1.7 shows the possible interaction pathways proceeding from $AB + e^-$. This work is primarily concerned with the dissociative attachment pathway:[1]

$$AB + e^- \to (AB)^- \to A + B^- \tag{1.3}$$

In the intermediate stage of the above equation, the transient negative ion (TNI) AB^- is also capable of *autoionization*, ejecting the attached electron and leaving the molecule in its neutral electronic state. The other dissociation mechanisms, which may occur at very

---

[1] In Fig. 1.7, the dot by the fragment A indicates a molecular radical. This notation is mostly omitted in this work.

different incident electron energies, proceed without a TNI and dissociate directly into ionic and radical constituents. These processes and DEA will be discussed briefly below.

1.3.1 Electron impact fragmentation

The first of the primary ionization mechanisms in Fig. 1.7 is electron impact ionization, characterized by the equation:

$$e^- + AB \rightarrow AB^{+*} + 2e^- \tag{1.4}$$

Here, an energetic electron ionizes the neutral molecule AB by knocking an electron out of its orbital and promoting the molecule to a state which may fragment into a neutral atom and a cation or simply remain ionic. The fragmentation channel is described by:

$$AB^{+*} \rightarrow A + B^{+*} \tag{1.5}$$

Typical threshold values for the electron energy are around the ionization potential of 10 eV, while the cross sections usually peak around 100 eV electron energy.[47] At higher electron energies, this process can certainly dominate the total interaction cross section. The shape and asymptotic level of the dissociative curve determines the kinetic energy of the fragments for molecular dissociation. The process was shown to produce excited neutral states of deuterated ice water from either dissociation of excited states or via electron-ion recombination[48] as well as radicals from organic molecules like methanol.[49] Although the focus of this work is primarily dissociative attachment, some initial data will be shown on electron impact ionization of methane.

1.3.2 Electron impact dissociative excitation

The threshold for excitation is below that of ionization, with minimum electron energies for excitation typically around 6 eV. In the equation:

$$e^- + AB \to AB^* + e^- \tag{1.6}$$

the incoming electron excites a molecular electron to an excited orbital, promoting the molecule to an excited state which can then decay via several channels. Since the incident electron scatters away from the molecule retaining some fraction of its initial kinetic energy, only that amount of energy required to cause the electronic transition in the molecule is transferred, so that excitation can occur over a wide range of incident electron energies. (This effect is exploited by electron energy loss experiments to determine excitation reactions.) Following the excitation, the excited-state molecule can emit a photon, relaxing the electron back into the molecular ground state, or in condensed media, where other molecules exist in close proximity, transfer energy to neighboring molecules. This is characterized by the equation:

$$AB^* \to AB + \text{energy} \tag{1.7}$$

The energy in this case is released in the form of a photon, but any molecular dissociation can also result in kinetic energy carried away by the fragments, depending on the release of the bond energy and the charge states of the fragments.

If the excited state is on a repulsive potential energy curve, the molecule can then dissociate, leaving an excited neutral fragment and a ground state neutral.

$$AB^* \to A^* + B \tag{1.8}$$

The excited molecule can also undergo dipolar dissociation, in which the excited neutral decays into a cation and an anion, known as ion-pair formation.

$$AB^* \to A^+ + B^- \tag{1.9}$$

The non-resonant production of electron-induced anions is characteristic of this process, since anions produced by desorption of electrons above ∼10 eV is not known to proceed via other mechanisms. Above this threshold, the anion yield increases continuously, unlike the resonant dissociative attachment process. This process has been observed in molecular oxygen leading to electron-stimulated desorption[50] and gas-phase dissociation[51] with electron energies up to 50 eV.

1.3.3 Dissociative electron attachment

The process of electron attachment is thought to proceed via several mechanisms, all of which produce a transient negative ion (TNI) from a neutral molecule's interaction with an incident electron, followed by dissociation of the TNI to a neutral fragment and an anion.

$$e^- + AB \rightarrow (AB^-)^* \rightarrow A + B^- \tag{1.10}$$

The TNI (or the transition to it from the initial state) is also commonly referred to as a *resonance*, due to the resonant nature of the attachment process. Resonances are further classified as either *shape resonances* or *Feshbach resonances*, depending on whether the TNI lies energetically above (shape) or below (Feshbach) the parent state. Shape resonances are named so because the neutral parent molecule has an attractive potential with a repulsive centrifugal barrier which allows the electron to tunnel through and become bound in the molecule (see Fig. 1.8). The barrier is formed by the combined effective potential of the attractive dipole term (induced by the incoming electron) and the repulsive pseudo-potential due to the electron's angular momentum.

$$V_{eff}(r) = -\frac{\alpha e^2}{2r^4} + \frac{\hbar l(l+1)}{2m_e r^2} \tag{1.11}$$

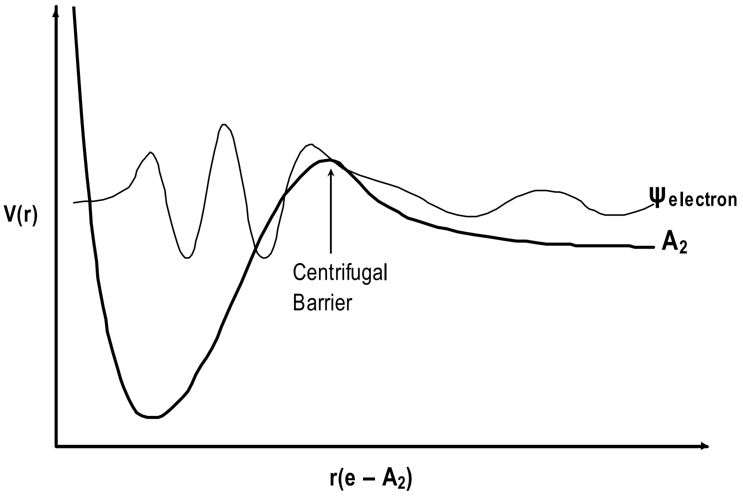

Figure 1.8: Potential energy diagram of a shape resonance for a molecule A_2 as a function of the electron-molecule separation $r(e - A_2)$. The incident electron sees a centrifugal barrier created by the molecule's repulsive angular momentum contribution to the potential.[2]

Since the barrier is formed by the non-zero angular momentum, these resonances must be caused by partial waves with $l > 0$, so that s-wave scattering does not contribute to these resonances. This type of shape resonance is called a *single-particle shape resonance.*

In another type of shape resonance, called a *core-excited shape resonance*, the electron is attached to an excited state of the neutral molecule, rather than its ground state. Again, a nonzero angular momentum component must exist to form the centrifugal barrier. In both types of shape resonances, the TNI state is energetically *above* the neutral parent state, so that the attached electron can be subsequently released via *autodetachment*, in which the electron is released and the molecule returns to the initial electronic state, possibly in an excited vibrational state. This process is only possible while the negative ion state is energetically above the ground state, so if the curves for the two states cross, the internuclear separation at that point places a limit on the autodetachment, after which the TNI can only dissociate. Figure 1.9 shows a vertical (Franck-Condon) transition to a TNI state which can autodetach before the internuclear separation increases beyond the curve crossing point.

Feshbach resonances are categorized as *core-excited* or *single-particle* (vibrationally-excited). These are caused by an electron occupying an open molecular orbital which brings

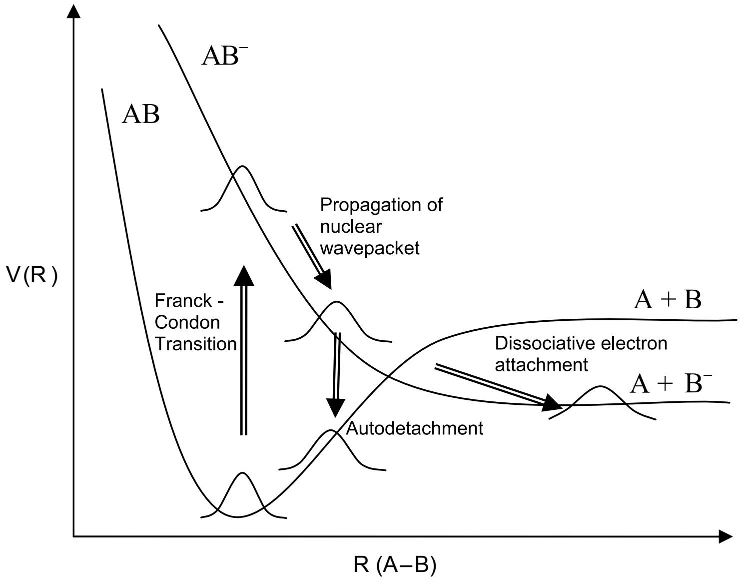

Figure 1.9: Potential energy diagram showing a Franck-Condon transition to a transient negative ion state and subsequent autodetachment or dissociation for a molecule AB.[2]

the molecule to a state which lies energetically *below* the neutral parent. The single-particle Feshbach resonances involve attachment to a higher vibrational state of the lower-energy TNI, which can then decay to the ground state of the neutral molecule via *autoionization* or autodissociation. Core-excited Feshbach resonances occur when the incident electron causes an excitation in the parent molecule, altering the PE surface seen by the electron, and causing it to be trapped in a bound state of the newly excited molecule (see Fig. 1.10). The positive nuclei in the molecule are less well-screened by the molecular electrons when one core electron is excited, so that the excited state of the neutral molecule has a greater attraction for the incident electron.

In this work, the target molecules are assumed to start from ground electronic and vibrational states, so that the observed resonances should be of the single-particle shape resonance or the core-excited Feshbach resonance type.

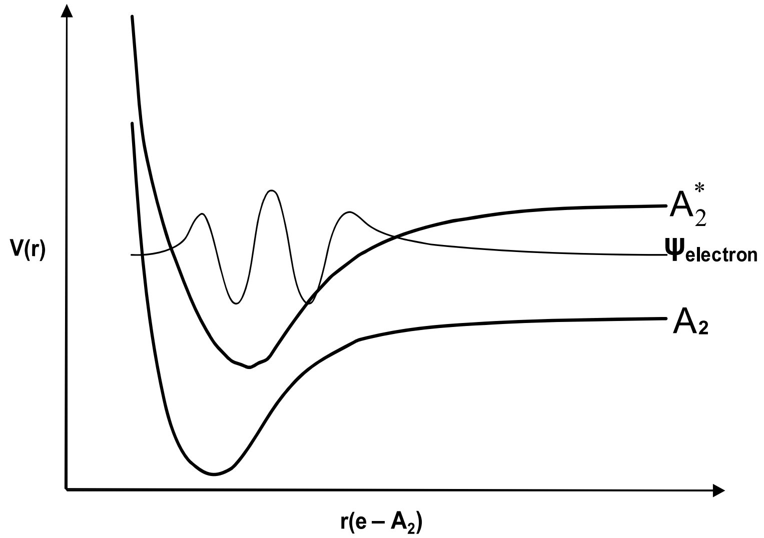

Figure 1.10: Potential energy diagram of a Feshbach resonance for a molecule A_2 as a function of the electron-molecule separation $r(e - A_2)$. The incident electron causes an electronic excitation in the neutral molecule, and subsequently becomes trapped in the potential of the excited molecule.[2]

1.4 Experimental History

Experiments and the theoretical calculations necessary to explain the results have dated back to the early days of quantum theory in the 1930s. Early experiments measured interaction cross sections by observing electron beam attenuation through a gas target,[52] while later decades saw the use of monoenergetic electron beams and movable electron detectors to measure scattering as a function of angle. This section will overview the progress of recoil ion momentum spectroscopy (RIMS) methods.

Early experiments on electron collisions with atoms and molecules commonly used movable detector assemblies to measure differential cross sections with the scattering angle of electrons. The limited range of angles afforded by these experiments led to ion momentum measurements capable of detection in all ion ejection angles. The earliest RIMS experiment used an electron beam incident upon a cylindrically confined gas target to produce recoil ions which were then accellerated with an electric field and charge-state analyzed with a magnetic field.[53] This method measured the transverse momentum of the recoil ions by

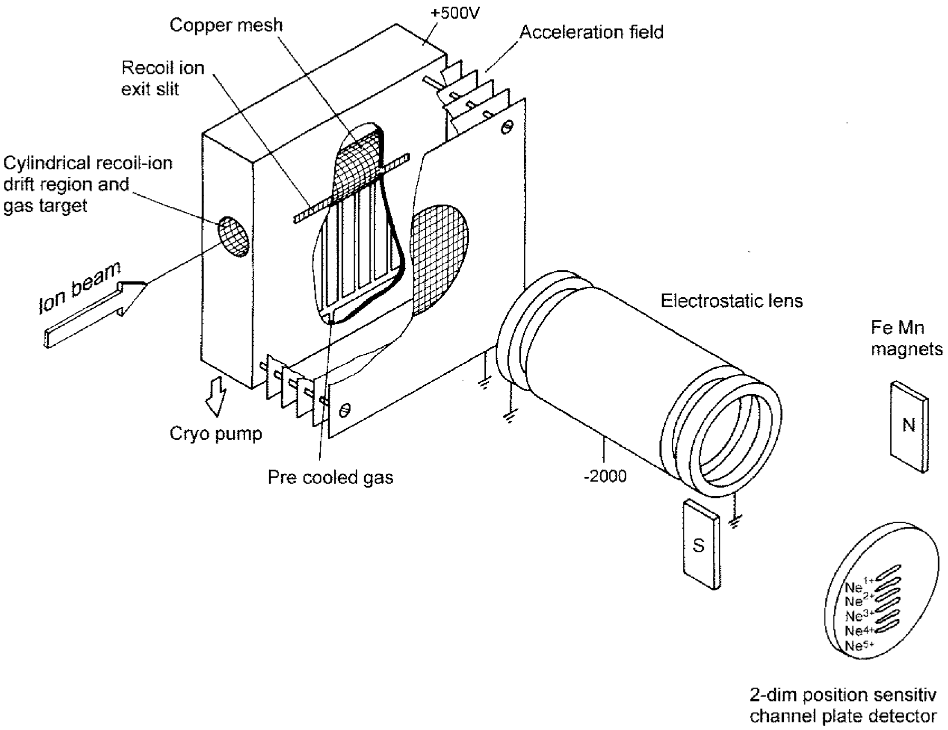

Figure 1.11: Early recoil ion spectrometer with cooled gas delivery. An electrostatic field pulls the ions produced from the ion beam toward the position-sensitive detector, and a static magnetic field separates the ion charge states.[56]

observation of the position on a microchannel plate detector. In these early experiments, where the target gas was at room temperature, the momentum resolution is limited by the thermal motion of the target. Later, significant improvements to the momentum resolution were achieved by cooling the gas target cryogenically and by using gas jets to deliver lower-energy particles.[54,55] This was shown to improve momentum resolution to below a few AU of momentum.[56] Figure 1.11 shows an ion spectrometer of this type with a cooled gas inlet.

One method of target introduction has been the use of an array of capillaries to inject the gas a few millimeters away from the projectile beam.[57,58] These methods first allowed the measurement of the longitudinal momentum transfer as well as the transverse momentum and allowed the full 4π measurement of the momentum for the recoil ions. By using position- and time-sensitive detection, momentum could be calculated in all directions and for ions of any initial trajectory.

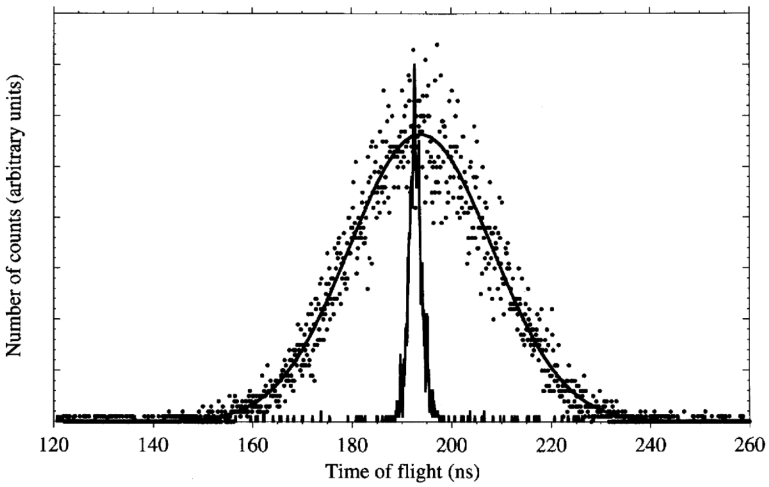

Figure 1.12: Time-of-flight distribution for ions from a supersonic gas jet and from room temperature gas. The broader distribution from the room temperature gas is due to thermal spread from larger initial (pre-collision) momentum.[56]

An important step forward in RIMS experiments involves the use of supersonic gas jet targets. For Cold Target Ion Momentum Spectroscopy (COLTRIMS), a supersonic jet is achieved by passing the gas through a small aperture which is followed by a collimating skimmer to select the center of the gas distribution. This target delivery method provides a well-localized and cold target for ion momentum measurements. Figure 1.12 illustrates the difference in ion flight times due to the thermal spread of a room temperature target. Typically for jet target delivery, a pressurized gas is passed through an aperture tens of μm in diameter, after which the gas rapidly expands into a vacuum towards a skimmer placed in line with the aperture. While most of the gas is thus pumped away, the small fraction that passes through the skimmer has very low energy. To avoid reintroduction of the target gas back into the chamber, a jet dump is used to catch the jet after it passes through the beam region and pump away the excess gas.

The particular geometry and voltage specifications of COLTRIMS spectrometers vary depending on the purpose, but they generally involve an acceleration region and a drift region. The acceleration region contains an extraction field to push ions toward the detector, and the drift region is field-free, allowing ions to further separate in time and space before

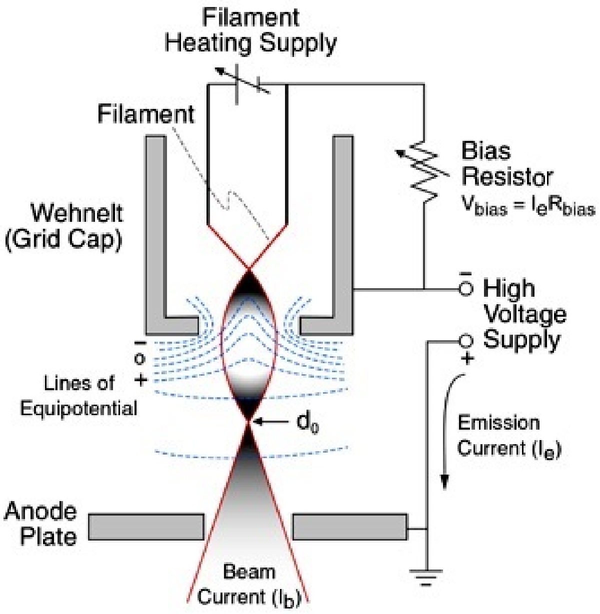

Figure 1.13: Typical design of an electron gun. Applying a voltage across a cathode causes it to heat to over 10^3 K and thermally emit electrons which are focused by a cylindrical "Wehnelt" electrode and extracted by an anode plate to form a beam.[56]

arriving at the detector. A ratio of 1:2 for the acceleration-to-drift distance was shown to produce a time-focusing effect in time-of-flight mass spectrometers by Wiley and McLaren.[59] With this "McLaren geometry", recoil ions starting at slightly different locations still arrive at the detector with the same time-of-flight, partially correcting for the effect of the finite interaction volume.

COLTRIMS has been historically used to study ion-driven and photon-driven processes, but similar studies (including the present one) have used the same spectrometer types to study electron-driven processes, while other interesting alternative methods such as velocity map imaging and velocity slice imaging have emerged in parallel. All of these methods typically use a pulsed, collimated electron beam generated by an electron gun similar in design to that shown in Fig. 1.13.

The velocity map imaging (VMI) method emerged in recent years to study photodissociation and photoionization dynamics.[60–63] In contrast to COLTRIMS spectrometers where flat electric fields are defined using transmission grids in the spectrometer, VMI uses open

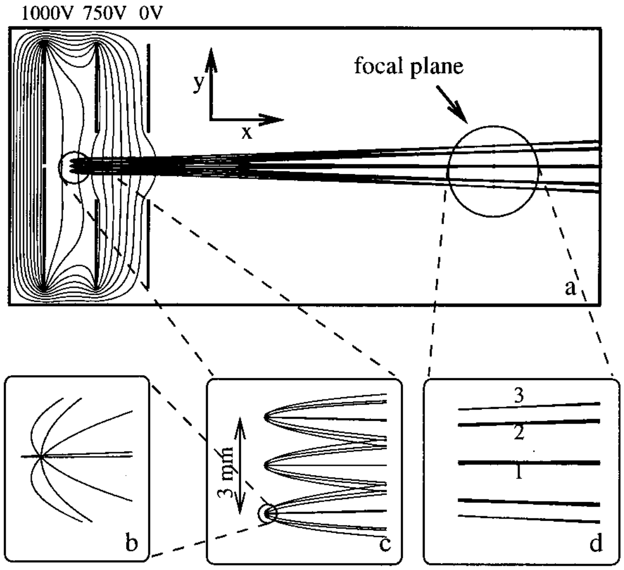

Figure 1.14: Simulated ion trajectories in a velocity map imaging spectrometer with (a) the total view, (b) and (c) zoomed-in views of the interaction point, and (d) zoomed in view of the focal plane, where the detector would be positioned.[60]

electrodes to intentionally produce lensing fields which cause all particles with the same initial velocity vector to land on the same point on the detector (see Fig. 1.14). The advantage of this method is that the finite size of the target overlap is collapsed down onto a point, improving the resolution of the final image. Also, the lensing configuration is such that transmission grids are not needed to define the electric fields, so ions are not lost or affected by interactions with grids, resulting in a higher sample rate.

Images in these experiments are often captured with the use of a CCD camera, which limits the timing resolution as compared to electronic detectors. Another disadvantage of this technique is that in order to reproduce the full 3D distribution, cylindrical symmetry is required (usually defined by a polarization vector), otherwise the distribution is collapsed into a 2D picture with no time information.

More recently, the velocity slice imaging (VSI) technique has been used to study angular distributions of dissociation fragments.[64,65] Originally designed to study photodissociation processes, it has more recently been adapted to the study of dissociative attachment.[66,67]

Velocity slice imaging involves allowing the kinetic energy of fragments to spread the distribution in time and space before the extraction field is activated. Then, instead of the detector acquiring data continuously, the detector is turned on for only a small time window in the middle of the anions' time of flight distribution, such that only anions with initial velocity parallel to the detector are imaged. An advantage of this method is that the planar angular distribution of the ions is immediately obtained from the detector image information, as the slicing of the momentum sphere is effectively done during the acquisition itself. As compared to VMI, no axis of symmetry or Abel transformation is required to reconstruct the three-dimensional data, and energy resolutions are comparable.[64] A limitation of this method (as compared to the COLTRIMS spectrometer used in this work) is that it typically uses an effusive gas target, instead of a supersonic jet, so that the large interaction volume is not completely corrected by the spatial focusing. Also, ions are accepted only according to their time of flight, regardless of their kinetic energy, so that anion distributions with differing kinetic energy are not properly comparable. This point will be discussed more in the context of the data on dissociative attachment to CO_2.

2 — The Apparatus

> ”This apparatus must be unearthed.”
>
> –*The Mars Volta*

The apparatus described here (shown in Figure 2.1) is intended to measure the post-interaction dynamics of dissociative attachment of electrons to gas phase molecules.[68] To do this, the apparatus brings together the advantages of various techniques used in the science of probing the interactions between atoms or molecules with projectiles including cations, electrons, and photons. The experiment is of a type which has been referred to in other works as a *reaction microscope*, appropriately summarizing the event-level examination of projectile interactions with a gas phase target.[69–71] By crossing a confined molecular target with a focused electron beam, the interaction is local, well-defined, and consistent to within the relatively small overlap volume. The use of a molecular jet, as opposed to a diffuse target, is a significant experimental advantage which restricts the initial kinetic energy of the target molecules, helping to resolve the angular distributions in momentum-space.

In the following sections, challenges specific to the present experiment (and others like it) will be discussed in detail. As will be explained below, experiments such as this require precise timing measurements and fast electronics on the nanosecond scale, as well as precise yet flexible control on pulse generation and spectrometer extraction voltages in order to accumulate usable data. Formation of the gas jet also requires flexibility and care to avoid a diffuse target at the interaction point. The pulsed beam of electrons must also be optimized

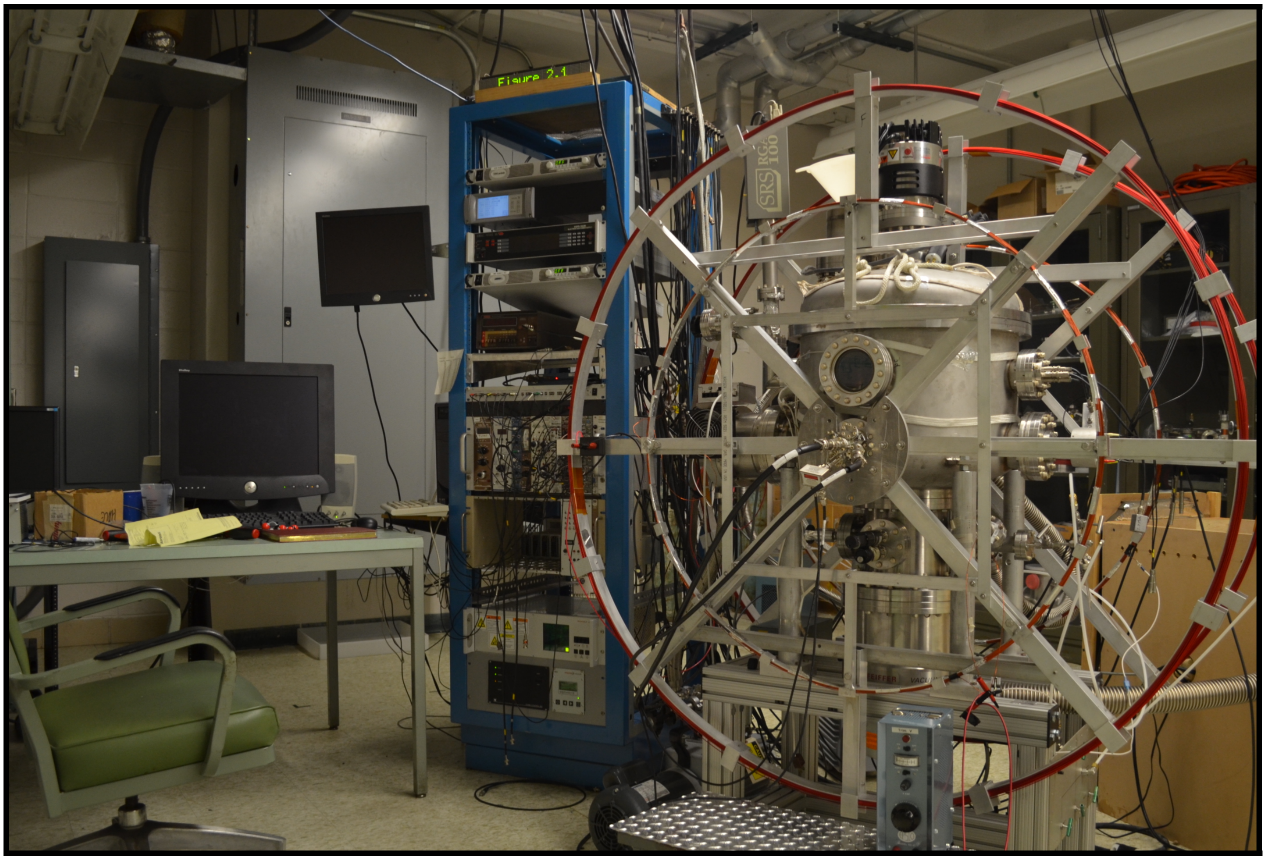

Figure 2.1: Photograph of the experiment. On the right is the vacuum chamber including the spectrometer, gas jet, and electron gun. In the center is the electronics rack, including pump and gauge controllers, power supplies, and logic modules for signal processing. On the left is the data acquisition workstation.

for the specific experiment. A trade-off always exists between higher electron current and better time resolution as limited by the electron pulse width, while the cross section of an interaction is an important consideration in determining acquisition times for large data sets. These challenges and others will be the main focus of this chapter.

2.1 Vacuum and Gas Jet

For the study of electron-molecule interactions, the importance of a good vacuum in exposing the desired phenomenon cannot be overstated. The supersonic expansion involved in the formation of the gas jet relies upon a well-evacuated region into which the gas will flow. The main chamber of the experiment will ideally contain only target molecules and electrons, such that only anions formed by the interaction are extracted by the spectrometer and detected. While in reality this is not perfectly possible, we need only that the ratio of signal to noise on the particle detector is sufficient to observe the desired interaction.

To that effect, the apparatus consists of a chamber with three main parts, each of which is maintained at vacuum by a turbomolecular pump and a backing rotary vane pump. Figure 2.2 identifies the main functioning pieces. The lower region is evacuated by a rotary vane pump from atmospheric pressure and a 1500 L/s Pfeiffer turbomolecular pump further down to below 10^{-9} Torr. This region contains the jet aperture housing, which sits on a movable stage, the specifics of which will be discussed below. The interaction between the molecules and the electrons occurs at the interaction point in the main vacuum chamber, shown at the center of Fig. 2.2, between the two yellow grids. This region is also supported by a rotary vane pump and a Pfeiffer turbomolecular pump (520 L/s) for a base vacuum pressure of close to 10^{-9} Torr. It contains the spectrometer, detector, a liquid nitrogen trap, and a residual gas analyzer (RGA) from Stanford Research Systems. Since the spectrometer separates ions based on charge-to-mass ratio, the vacuum in this region must be good enough that the time-of-flight spectrum is not contaminated by similarly charged species to the desired product. To this end, the liquid nitrogen trap is used to reduce the presence of water

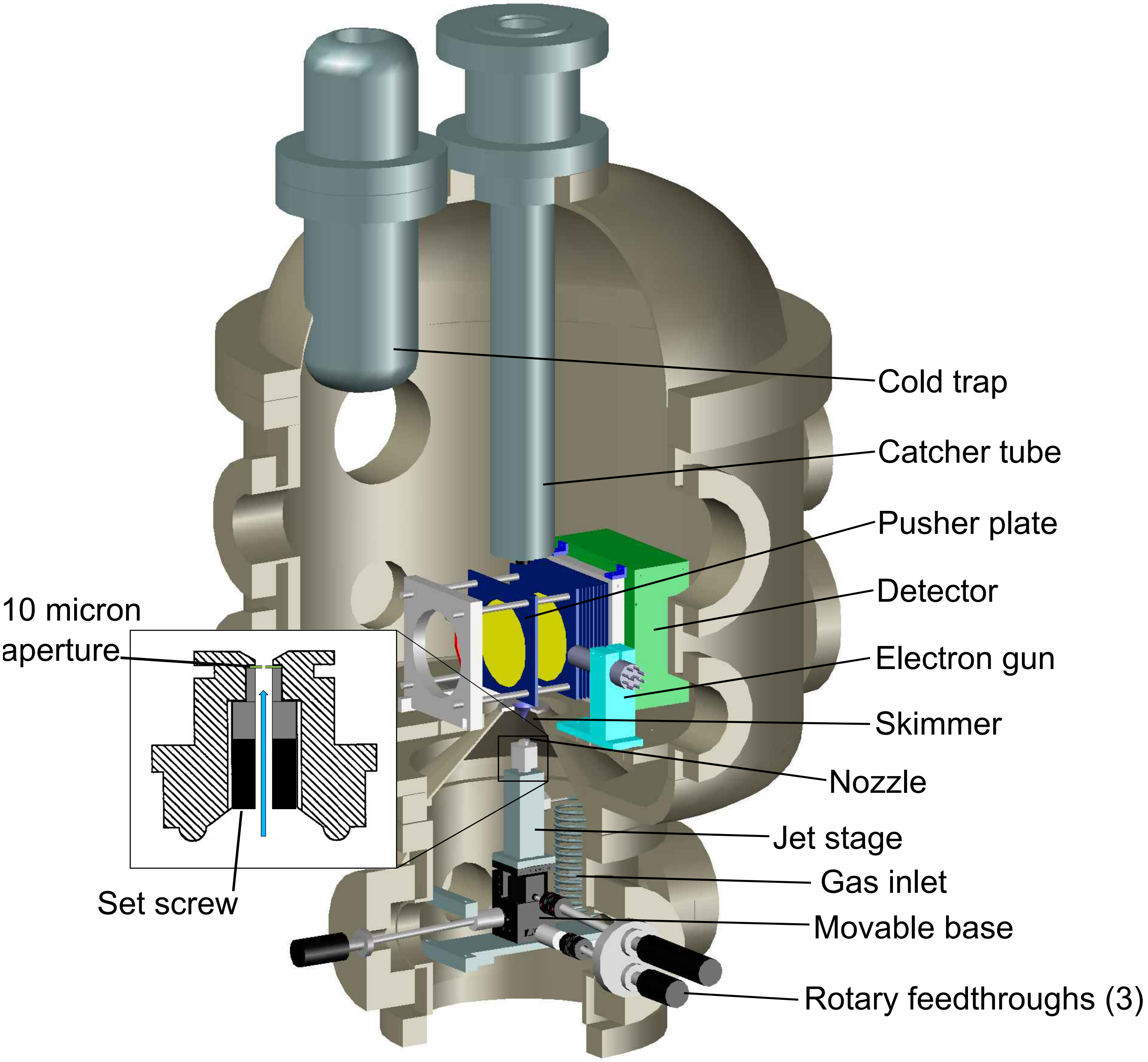

Figure 2.2: Cutaway visualization of the apparatus. A coiled gas inlet feeds into the jet stage, which is movable in three dimensions by three rotary feedthroughs. The jet aperture is housed in a screw-on VCR fitting situated atop the jet stage, and the skimmer sits directly above it. The chamber bottom separates the jet region (smaller bottom portion) from the main chamber (large middle portion) which houses the spectrometer and electron gun. The gas jet passes through the spectrometer and is deposited into the catcher tube (narrow vertical section), where the gas is pumped away. The electron-molecule interaction occurs midway between the two spectrometer plates with yellow grids, near the center of the figure.

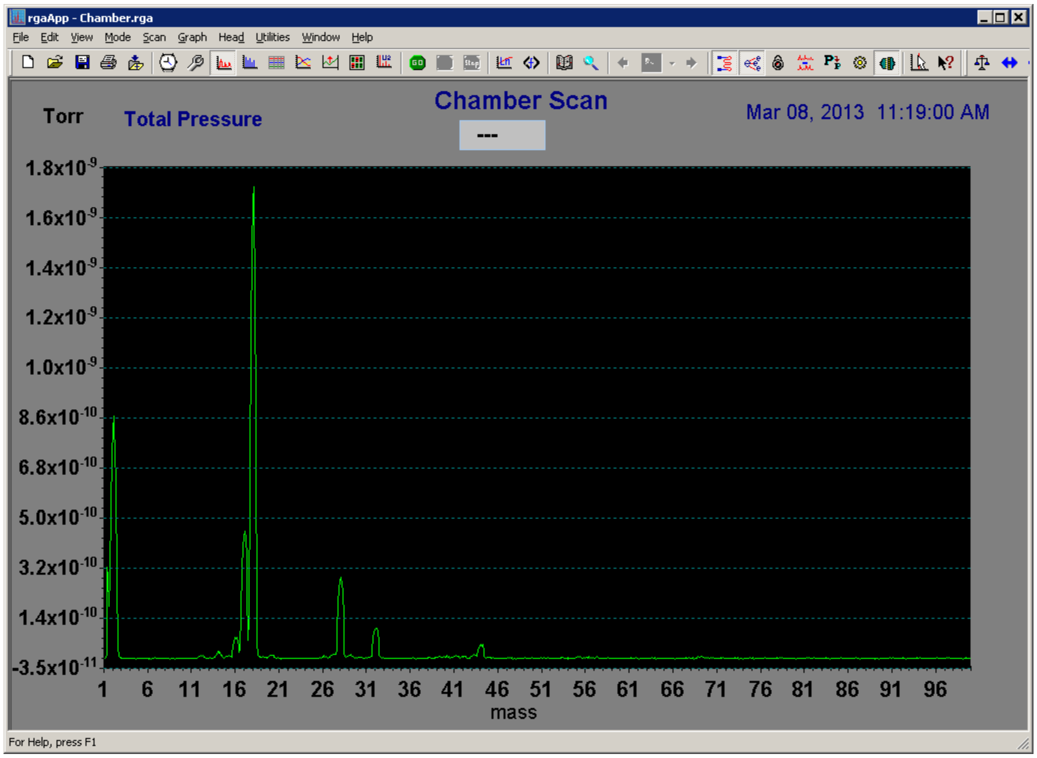

Figure 2.3: Mass spectrum of the base vacuum from a residual gas analyzer (RGA). Visible are peaks correlated to H_2, H_2O, N_2, O_2, and CO_2.

in the background gas, which can produce contaminant anions which obscure investigation of the desired reaction. The jet gas is directed into a "catcher tube" suspended vertically above the spectrometer which is pumped by a 240 L/s Leybold turbomolecular pump backed by a rotary vane pump. This small region is maintained at a base pressure of close to 10^{-10} Torr and serves to capture the molecules in the jet so that they don't return to the main chamber and disrupt the rest of the experiment.

Pressure in each of these three regions is monitored with ion gauges as well as the RGA. The RGA can be used to check for leaks in the vacuum system and to determine the constituents in the background gas for vacuum diagnostics. Additionally, since the RGA detects the background gas in the main chamber and not the jet gas (except for a residual amount), it is used to align the translating jet stage by minimizing the contribution of the jet gas species to the RGA spectrum. This optimization ensures that the jet gas is confined (not diffuse) and that the catcher actually captures the molecular beam, not allowing it to

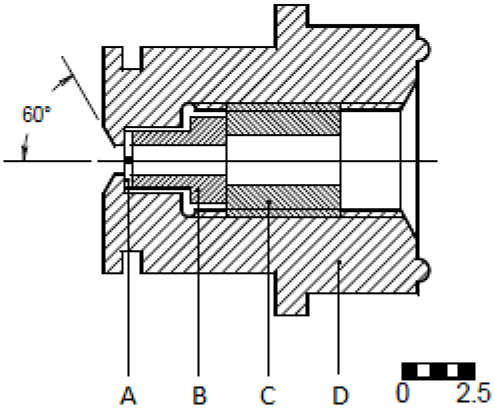

Figure 2.4: Drawing of the jet aperture design. (A) 10 μm platinum aperture, (B) pressure plate, (C) M4 set screw with axial hole, and (D) nozzle carrier Cajon part SS-4-VCR-2-5M. Scale in millimeters. This entire design forms the leftmost structure in Fig. 2.5, from which the jet gas initially emerges. Figure reproduced.[73]

be scattered back into the main chamber. Figure 2.3 shows a scan of the chamber at base pressure (without a gas jet). The main constituents of the background gas are diatomic hydrogen (mass 2), water (18), and diatomic nitrogen (28), with smaller amounts of O_2 (32) and CO_2 (44). The RGA is also useful for verifying the jet gas contents when the target is changed and the gas inlet must be purged of the previous gas target. Since the RGA analyzes gas by ionization from an electron gun, it really measures mass-to-charge ratio, so molecules like water produce a characteristic *cracking pattern* resulting from the different ionization and fragmentation pathways available in the molecule, so that water has peaks at masses 18, 17, and 16.[72]

2.1.1 Gas Jet

The supersonic gas jet is formed by pushing the target gas through a tiny aperture formed by a laser-drilled disc, after which a rapid expansion into the high vacuum jet region occurs. A skimmer mounted above the aperture selects the center of the gas distribution, where the least energetic molecules are located. Figure 2.4 shows the basic design of the aperture housing. The aperture itself is a thin disc which is held in place by a vented set screw pressing

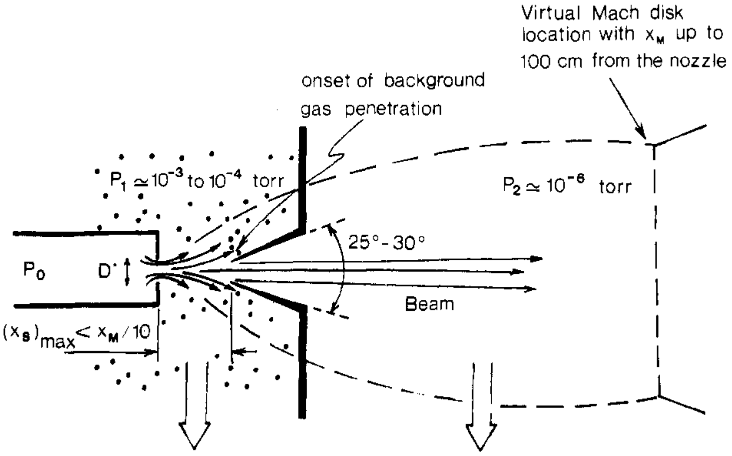

Figure 2.5: Schematic diagram of a jet aperture/skimmer showing the expansion from the stagnation region in the delivery tube into the lower vacuum region towards the skimmer. The jet source (far left) is shown in more detail in Fig. 2.4. The distance of the aperture to the skimmer is important in determining the energy distribution in the jet and the amount of gas accepted through the skimmer. Figure reproduced.[74]

onto a hollowed shaft. Figure 2.5 shows the aperture and jet design together. Since the 0.3 mm skimmer (Beam Dynamics) selects out the center of the expanded jet, the distance from the aperture to the skimmer is important in determining the energy and spatial size of the jet. The present apparatus has the advantage of a three-dimensionally translating jet stage (shown at the bottom of Fig. 2.2) which allows immediate adjustment of that parameter.

The entire assembly is housed in a modified VCR fitting held in place by a nut which screws onto the pedestal on which the aperture housing sits. Figure 2.6 shows the stage fully assembled. The pedestal is a hollow aluminum block which routes the gas from the inlet to the aperture and elevates the aperture nearer to the skimmer. In Fig. 2.6, the gas inlet is visible in the top-left of the picture and the gas line coils upward before connecting to the pedestal. This is done because, as the pedestal is movable in three dimensions, it is necessary to have a flexible line that will not produce tension when the pedestal is moved off center. Two ports in the bottom of the picture are used to provide the external control on the jet position. The jet pedestal sits on a stack of three optical translation stages which connect to knobs on the outside of the vacuum chamber via rotary feedthroughs. In the picture are

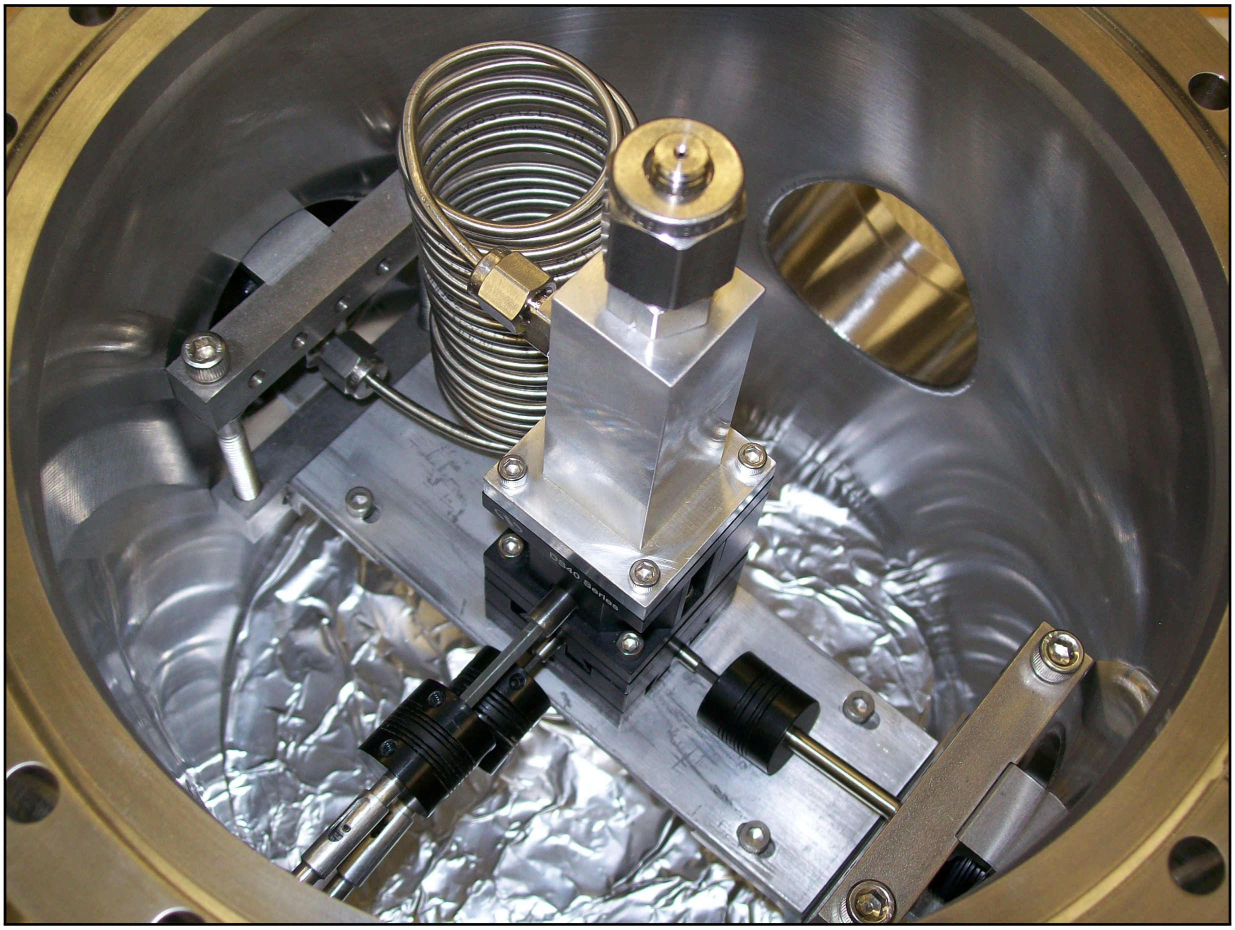

Figure 2.6: Photo of the jet region. At center is a pedestal block set on a stack of three translatable optical stages with rotary feedthroughs for external position control. At top-left is a gas feedthrough with a coiled gas line (for flexibility) leading to the pedestal block containing the aperture housing, located top center. This assembly is mounted beneath the hole in Figure 2.10.

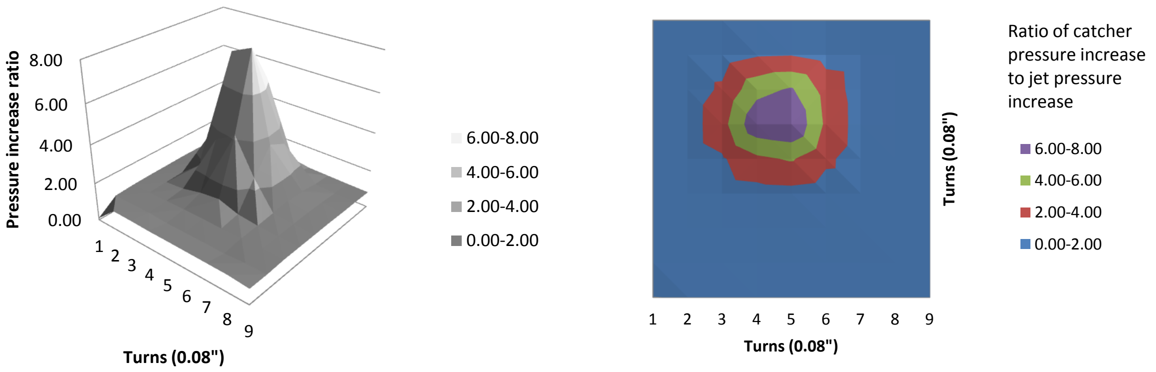

Figure 2.7: Surface plots of the ratio of pressure increase in the catcher to that in the jet region as the aperture stage is moved. The motion of the jet is quantified by whole turns of the rotary feedthroughs controlling the jet position, where one turn translates the stage by 0.08”. This pressure ratio is an indication of the amount of gas from the jet that enters the catcher tube, suggesting the proper alignment of the jet with the skimmer.

visible three flexible shaft couplings which maintain the mechanical connection while the pedestal is allowed to move. Three mechanical counters are coupled to the knobs on the outside to display the aperture’s position.

Figure 2.7 shows the ratio of the increase in pressure in the catcher to that in the jet region as the stage is moved in two dimensions. The independent variable is the motion of the stage via the knobs mentioned above where one unit is equal to one full rotation with 0.08” linear motion per turn. The stage unmoved from its center would be at position (4.5, 4.5). The plotted ratio is essentially the amount of gas which forms the jet versus the amount that is skimmed away. From the right plot, it is apparent that the ideal stage position is off center in one direction (although it can be realigned during maintenance). Helium was used as the jet gas in this test.

The aperture has a converging diameter with a minimum of 10 μm at the exit point. The skimmer sits inverted above the aperture and consists of a cone with a curved profile and a minimum diameter of 0.3 mm. Given the geometry of the jet assembly, a simple calculation gives a jet diameter of 2-3 mm at the interaction point. With a room-temperature input gas, the temperature profile of a gas jet with a 10 μm aperture could easily be expected to produce gas at a temperature lower than 15 K at the interaction region.[75] The density of the jet in the interaction region is calculated via the particle flow rate. Given the rise in the catcher pump pressure ($\sim 5\times10^{-9}$ Torr), the manufacturer's reported pump speed (270 L/s), and the estimated jet temperature (15 K), the mass flow rate $\frac{dm}{dt}$ into the pump for a molecular mass (in amu) of m is given by the following formula:[76]

$$\frac{dm}{dt} = \frac{m}{k_B T} PS \tag{2.1}$$

where k_B is the Boltzmann constant, T is the jet temperature, P is the pressure increase in the catcher (from a base of $\sim 5 \times 10^{-10}$ Torr), and S is the pumping speed. For a molecular mass of $m = 32$ (oxygen) the mass flow rate is 2×10^{17} amu/s. This translates to a molecular flow rate of $\sim 6 \times 10^{15}$ molecule/s. The density is then calculated from

$$\rho_{jet} = R_{O_2} \frac{1}{v_{jet} A_{jet}} \tag{2.2}$$

where A_{jet} is a geometric estimate of the cross-sectional area of the jet (1.5 mm diameter) at the interaction region, based on nozzle/skimmer sizes and separation. R_{O_2} is the molecular flow rate calculated above, and v_{jet} is the estimated velocity of the jet (based on earlier measurements of the flight time and displacement of ions from the interaction point) to be roughly 10^5 cm/s. The jet density then is about 10^{12} molecules/cm^3 for O_2.

2.2 Electron Beam

A pulsed beam of electrons is generated using a Kimball Physics ELG-2 electron gun, shown in Fig. 2.8 (along with the spectrometer and gas jet), which consists of a gun head mounted inside the chamber with wires leading to a custom feedthrough for connection to an external power supply and controller. The gun head contains a filament with a tantalum disc cathode which undergoes thermionic emission upon application of a small voltage (1.2–1.6 V). The gun head also houses an anode which accelerates electrons away from the filament and a grid which, when biased negatively, suppresses emission of electrons from the filament. The grid's

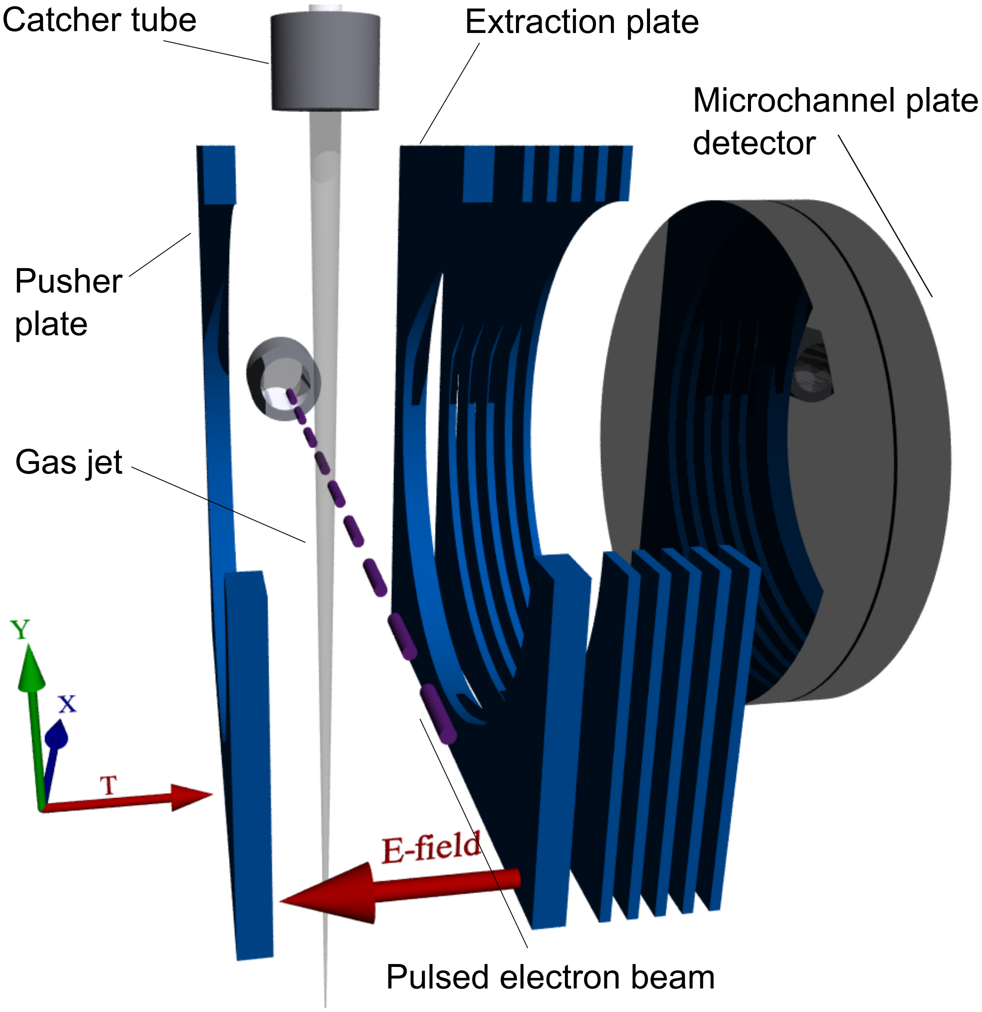

Figure 2.8: Cutaway illustration of the spectrometer. The pulsed electron beam (along the X direction) intersects the gas jet (along the Y direction) in the center of the spectrometer. The pusher plate and extraction plate define a flat electric field which is pulsed on after the electron bunch clears the spectrometer. Anions are extracted onto the microchannel plate (MCP) detector by the pulsed field.

primary function is to produce a pulsed beam of electrons instead of a constant stream. This is necessary because electrons from the beam must not be in the interaction region while the electric field is turned on, lest they be extracted towards the detector and reflect off of surfaces in the chamber, producing undesirable signals on the detector. In order to produce a pulsed beam, the grid is biased at a negative voltage high enough to suppress any significant electron emission (usually 10–12 V), and a positive power supply (Tennelec TC 952A High Voltage Supply) is pulsed to bring the grid voltage back to 0 V for a short window in time, so that electrons are emitted only during that window. Similar to the spectrometer, the pulsing is done by using the TC 952A to provide a constant voltage to a DEI HV-1000 fast-switching pulse generator which uses a controlling gate signal from a separate pulse generator to switch the voltage from the TC 952A off and on.

Typically, the bunches of electrons are 100 ns in length, although they may be as short as 30 ns. Ultimately, the greatest source of systematic uncertainty in the time-of-flight of the anions comes from the electron bunch width. The time-of-flight of any anion is calculated with respect to the beginning of the electron gun pulse, since the electrons is the catalyst for the anions formation, but the starting time of any particular electron is only known to within the electron pulse width. The time-to-digital conversion (TDC) card, which receives the detector signals and digitizes their times of arrival, has 0.5 ns resolution and the timing and acquisition electronics are accurate to within nanoseconds; The uncertainty about where in the electron bunch the interacting electron came from is the largest source of systematic uncertainty. Thus, it is obviously advantageous to minimize the bunch width in order to optimize the momentum resolution, but a smaller bunch width also reduces the electron current and thus the event acquisition rate.[1] The choice of the electron bunch width is, then, a comprimise between resolution and acquisition time.

A focus electrode and two pairs of steering electrodes allow some control over the direction and shape of the electron beam, although an external magnetic field generated by two

---

[1] Typical instantaneous electron beam current is $\sim$1 μA, so that the number of electrons passing through the interaction region is $\sim 10^6$ for each cycle.

pairs of concentric Helmholtz coils confine and direct the beam through the center of the spectrometer. More detail on these coils will be given below.

The electron gun power supply (Kimball Physics EGPS-1022B) allows for control of the gun's beam current, grid voltage, anode voltage, electron energy, and steering/focusing parameters. The beam current is controlled by adjusting the voltage applied across the cathode to alter emission and varying the anode voltage to affect electron extraction. The electron energy has a nominal range of 1 eV–2 keV with ±0.5 eV energy resolution.[2] The electron gun power supply adjusts the electron energy by adding the electron energy setting to all the other voltages, such that the voltage difference across the cathode and other relevant electrodes is unchanged, but the emitted electrons have the appropriate energy with reference to ground. Although beam energies of below 3 eV are attainable, high beam current at these low energies becomes a challenge to achieve. In order to monitor the beam current, a biased Faraday cup with a suppression grid absorbs the electrons after they exit the spectrometer.

2.2.1 Faraday Cup

The Faraday cup is mounted on the opposite side of the spectrometer from the electron gun and catches electrons after they pass through the region of interaction with the gas jet. It consists of a conductive cup held at a positive voltage and an electrically separate suppression grid held at ground. An array of 9 V batteries biases the suppressor at a constant 90 V. Since the vast majority of electrons pass through without interacting with a molecule, it is important to disallow the electrons scattering from the chamber walls and other surfaces. Depending on the electron energy, problems such as scattering and secondary electrons can cause a bare cup to emit electrons back into the spectrometer, so a grid covering the front face of the cup produces an electrostatic field which helps to prevent electrons from escaping the cup. A Keithley 614 electrometer is connected to the power supply to moniter the current

---

[2] The energy setting and resolution were verified by comparing the anion yield against known peaks in the dissociative attachment cross section for species such as H_2O, where a broad resonance peaks around 6.5 eV, and the sharp onset of a dissociative attachment resonance in CO_2 at 4 eV (discussed in Chapter 4).

drawn, which makes the cup useful also as a tool to measure beam current and position. Since the electron beam's current can vary significantly depending on factors such as cathode temperature, beam energy, magnetic field, and bunch timing, the advantage afforded by a direct measurement of the beam current is important to maintaining experimental stability. At the energies used in this experiment, a constant beam current is typically in the 1–10 μA range, while the pulsed beam is approximately a factor of 10^{-3} less.

2.2.2 Helmholtz Coils

Particularly for low energy beams, electrons are sensitive to stray magnetic fields and Coulomb repulsion. In order to combat this, a stronger axial magnetic field is generated by a set of Helmholtz coils aligned with their axis along the direction of beam propagation. As shown in Fig. 2.9, a pair of coils with radius 0.75 m is made of 132 turns of 14 gauge wire (for each coil) which typically carry a current of about 7 A. Power is provided to the pair with a TDK-Lambda GEN100-15 power supply at a typical setting of around 70 V. The coils are centered about the interaction region of the spectrometer to utilize the uniform magnetic field created at the center point on the axis of the Helmholtz pair. The pair of coils are separated by slightly less than their radius, so the pair does not exactly match the Helmholtz configuration but is near enough for the purpose of electron beam confinement. The magnitude of the magnetic field at the center point is given by

$$B = \left(\frac{4}{5}\right)^{\frac{3}{2}} \frac{\mu_0 N I}{R} \tag{2.3}$$

with radius R, number of turns N, current I, and vacuum permeability constant μ_0. The value is calculated to be ∼11 G for the given parameters. While not shown in Fig. 2.9, a second smaller set of coils was later added to augment the field strength. This second set has R=0.51 m, carries a current of ∼6 A, and is powered by a TKD-Lambda GEN100-7.5 power supply. The combined field at the interaction point is typically in the 20–25 G range.

Figure 2.9: Illustration of the apparatus with Helmholtz coils attached. The coils are attached to the chamber around the electron gun feedthrough, approximately coaxial with the electron beam.

In practice, while the experiment is not very sensitive to the particular value of the magnetic field, that the field exists is important to collimate the electron beam as well as sweep away stray ions from striking the detector and contributing to noise in the final data. In principle, the trajectory of any anions is also affected by the magnetic field, so a calculation of the cyclotron period is warranted.

$$T = \frac{2\pi m}{Bq} \tag{2.4}$$

with anion mass m, magnetic field strength B, and charge q. For O^- in a field of 25 G, the period of rotation is over 400 μs, while typical flight times for these ions are less than 10 μs, so the effect is not considered significant.

2.3 Spectrometer

The spectrometer consists of a series of aligned plates which produce a pulsed, uniform electric field to extract anions created at the interaction point. Figure 2.8 shows a cutaway view of the spectrometer. The coordinate system in the figure is the same as that used throughout the analysis and presented data, with T used to refer to the time-of-flight axis. The pulsed beam of electrons moves in the positive X direction and is captured by a Faraday cup on the far side of the spectrometer. In the center of the spectrometer, the electron bunch intersects the supersonic gas jet, occasionally producing a dissociative attachment anion product.[3]

The real detection rate is usually on the order of hundreds of events per second, including background events, and this can vary due to its dependence on several factors including the actual interaction cross section, electron beam current, gas jet target density, repetition rate, beam overlap, and detection efficiency. The detection efficiency is limited by the transmission grids (~90% open area) and the efficiency of the MCP stack (~60%). With two transmission grids, this amounts to ~50%. The repetition rate (discussed more in the timing section) is typically 40 kHz. The pulsed beam current is typically ~10 nA, but can vary considerably with beam energy. The jet density is on the order of 10^{12} molecules/cm^3 for O_2. The overlap is not measured directly, but a rough estimation (approximating each beam as a 2 mm diameter cylinder) would give the volume of the bicylinder (overlap volume) as $\frac{16}{3}$ or $\sim 5mm^3$. The expected event rate could then be estimated as

$$rate = \sigma \times \rho_M \times \rho_e \times V \times v_e \times \epsilon \times D, \tag{2.5}$$

where σ is the DEA cross section, ρ_M is the molecular density, ρ_e is the electron density, V is the beam overlap volume, v_e is the electron velocity, and ϵ is the detector efficiency.

---

[3] With a pulse rate of 40 kHz and an acquisition sample rate of roughly 300 Hz, the vast majority of electron bunches do not produce a detected anion, so the probability of the desired DEA interaction actually occuring, and being subsequently detected, is quite low for a single cycle.

The Gas Jet section gives the molecular density as $\sim 10^{12}\,\mathrm{cm}^{-3}$, and the electron density can be calculated from the beam size, beam current ($\sim$100 nA), and interaction cross section σ (roughly 10^{-19} cm^2 for CO$_2$ at 4 eV). The factor D is the duty cycle factor. Since the electron beam is pulsed, the expected rate of anion production is reduced by the fraction of the repitition period during which the interaction can actually occur. In this case, this fraction is the ratio of the electron bunch width to the cycle period. Then, the rate can be expressed as

$$
\begin{aligned}
rate &= \sigma \times \rho_M \times \left(\frac{I_e}{v_e \pi r^2}\right) \times V \times v_e \times \epsilon \times D && (2.6)\\
&= \sigma \times \rho_M \times \left(\frac{I_e}{\pi r^2}\right) \times V \times \epsilon \times D && (2.7)\\
&\approx (10^{-19}\,\mathrm{cm}^2)\left(10^{12}\,\frac{1}{\mathrm{cm}^3}\right)\left(\frac{10^{-6}\,\mathrm{A}}{\pi(10^{-2}\,\mathrm{cm}^2)}\frac{1}{10^{-19}\,\mathrm{C}}\right)(5\times 10^{-3}\,\mathrm{cm}^3)(0.5)\left(\frac{10^{-7}\,\mathrm{s}}{2.5\times 10^{-5}\,\mathrm{s}}\right) && (2.8)\\
&\approx 300\,\mathrm{Hz} && (2.9)
\end{aligned}
$$

Two plates spaced symmetrically about the interaction point produce the flat electric field which initially extracts the anions towards the detector. In Fig. 2.8, these are the two leftmost plates, with the left plate pulsed to a negative voltage (usually around 50 V) and the right plate held at ground (0 V). This provides a field which points to the left and extracts the anions to the detector on the right. Between the acceleration region and the detector exists a field-free drift region composed of several grounded plates to shield the region from stray fields (see Fig. 2.10). This area allows the anions originating from the interaction point to continue spreading out spatially in order to increase the resolution in all three coordinates. Since anions are created from a molecular dissociation, they emerge from the interaction with some finite kinetic energy, and thus spread out in time-of-flight and in space depending on the direction of their initial momentum vector. This effect is purposely taken advantage of by delaying the extraction pulse such that the momentum sphere of the anions expands

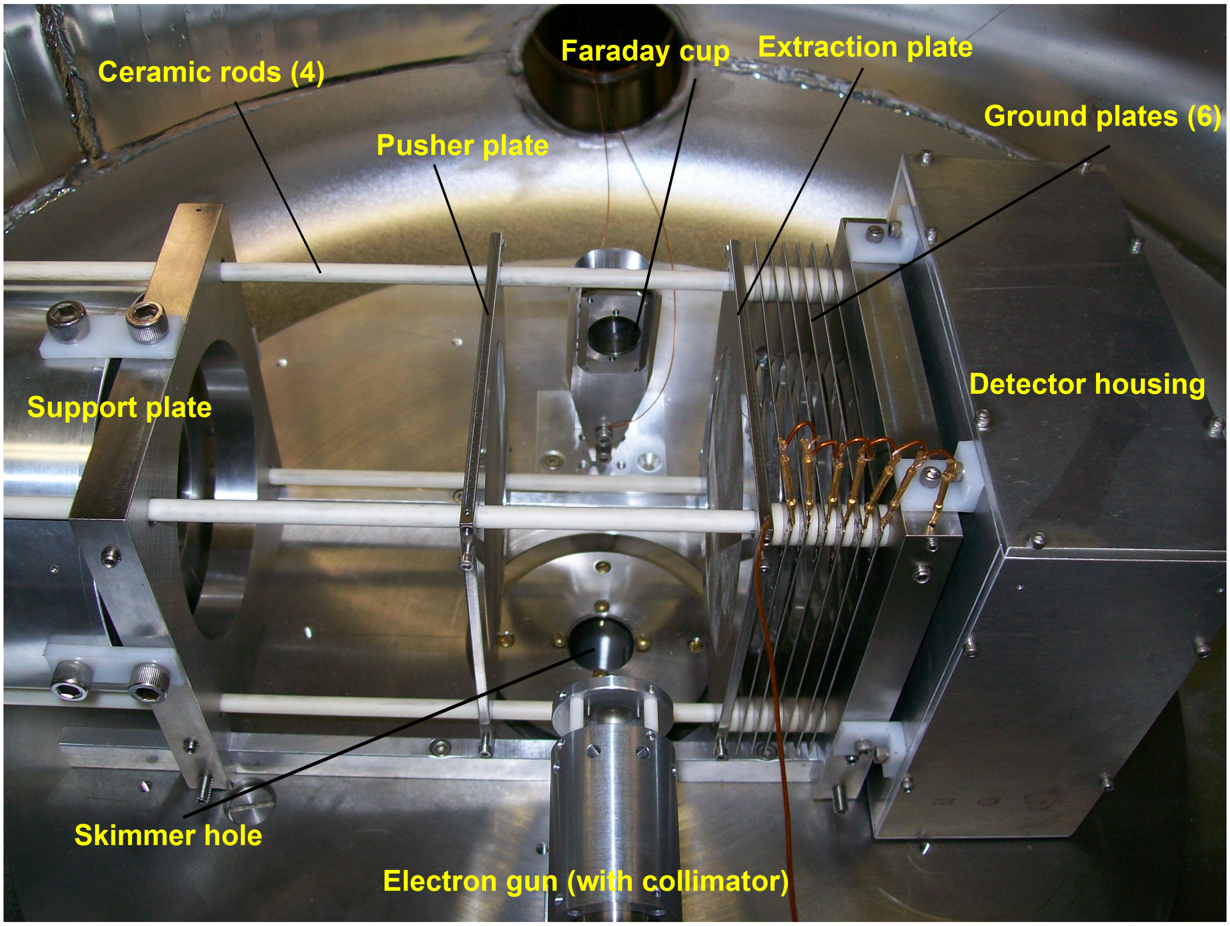

Figure 2.10: Photo of the spectrometer region. At the bottom is the electron gun head (covered with a collimator), on the far left is a support plate, left of center is the pusher plate (electrode), right of center is the extractor plate, followed by a series of grounded plates to define the field-free drift region, and far right is another support plate with the detector boxe mounted. The jet emerges from the hole in the center of the photo (see Fig. 2.6), and just above center is the Faraday cup.

prior to the extraction, as long as all the anions (regardless of initial direction) are still able to be confined to the detector.

Since the electric field used to extract the ions after the interaction must only be on when the electron beam is not in the interaction region, the spectrometer plates must be pulsed to coincide with the electron beam trigger. Since fast switching is required, often at higher voltages, a DC power supply is used to charge a fast-switching pulser which is then connected to the spectrometer. An Ortec 556 High Voltage Power Supply provides a constant voltage which is usually in the 20–50 V range. This constant voltage is supplied to a DEI PVX-4140 pulse generator which switches the supplied voltage on and off according to a gate signal generated by a separate pulse generator, the SRS DG535, which will be discussed more later. The DEI pulser is capable of switching voltages up to 3500 V, although the actual voltages for the spectrometer in this experiment are typically much lower.

It should also be noted that the two plates that define the interaction region in Fig. 2.8 as well as the front face of the box containing the detector each have an electrically conductive transmission grid installed which defines a flat electric field boundary while allowing the passage of the majority (∼90%) of ions. Given that a detected anion must pass through these grids in order to be detected, only about 81% of the produced anions have a chance of being detected. Still, even these ions are subject to the detection efficiency of the microchannel plate detector, which will be addressed below.

As simulations will show, the choice of extraction voltage and delay time are also important considerations for the spectrometer configuration. The spectrometer must be configured such that there is a single-valued function that relates the time-of-flight of an anion to the momentum of that anion in the time-of-flight direction, regardless of the anion's initial direction. Only in this way can the apparatus ensure both complete 4π collection and data resolvable into momentum information. These concerns will be addressed in further detail in the Simulation chapter.

2.3.1 Detection and MCPs

Particles are detected by extraction onto a microchannel plate (MCP) detector with a delay-line anode position detector. Ions first hit the stack of two MCPs and produce a shower of electrons which then trigger a signal on the delay-line anode. The design and operation of MCPs will be further discussed below. Signals from the MCPs and delay-line anode are used to calculate positions and times of impact for the ions in software.

Microchannel plates are designed to amplify a signal produced by incident ions and photons via a cascading series of secondary electrons triggered by the initial incident particle.

The plates are manufactured by drawing a glass tube with an etchable core through a vertical oven to produce a 1 mm diameter fiber. The fibers are then bundled together in a hexagonal array and redrawn such that the glass fuses and the etchable core material remains in the bundle. The process is repeated until a bundle of desired thickness is produced, at which point the fused bundle is sliced at a bias angle of roughly 8°. The slices are then polished and etched to produce the channels and the plates are baked in a hydrogen oven, coating them in a semiconducting surface which can produce secondary electron emission.

On the left in Fig. 2.11, the hexagonal boundaries resulting from bundling the fibers are visible. On the right, a closer view of one of the boundaries shows the hexagonal arrangment of the channels, while the channel diameter appears to be roughly 25 μm. Although not visible in the image, the channels do not run perpendicular to the plane of the image, but rather at a small angle resulting from the bundle having been sliced at a bias. This helps to ensure that when a particle enters a channel, it more quickly strikes the inside wall of the channel and is less likely to pass through the channel without colliding. Since particle must enter a channel to be detected, the open area ratio also impacts the transmission of the MCP. Typical ratios are around 0.6, meaning that a particle incident on the surface of the MCP has a 60% chance of entering a channel rather than striking the surface of the plate. Since the total transmission of the spectrometer grids, as stated previously, is around 80%, this makes the total detection efficiency about 50%. While this retards the acquisition rate, the data are unaffected, since all anions still have the same probability of detection.

In the present experiment, an anion enters one of many channels which run through the thickness of the plate and strikes the inner surface of a channel. This emits secondary electrons that subsequently collide with the inside of the channel as well, producing still more secondary electrons. A large voltage difference (~2200 V) is maintained across the plates so that electrons produced in the channels are pushed towards the back of the MCP. The process continues until the electrons exit the back of the plate, at which point the number of electrons leaving is typically $\sim 10^7$ for a single incident anion. This amplification makes

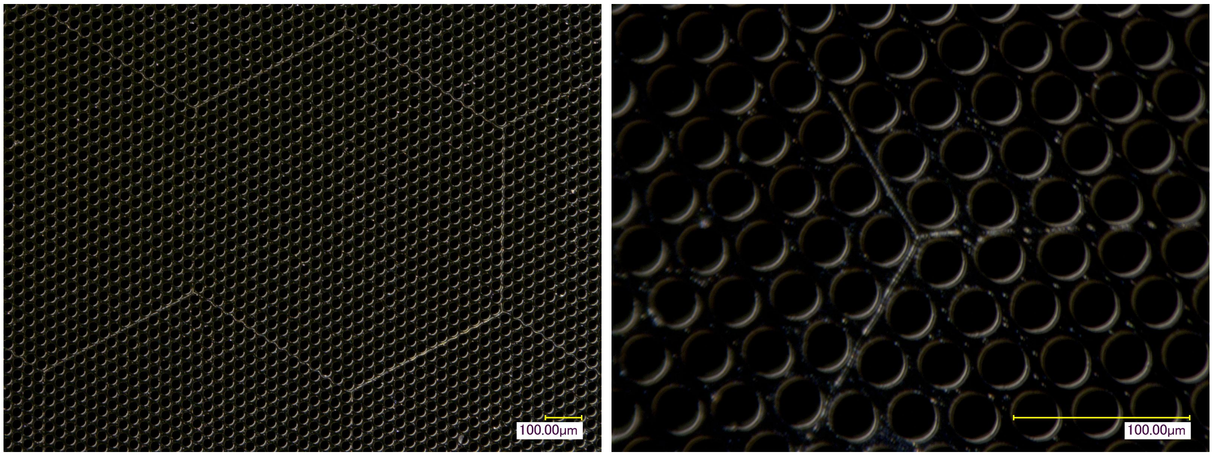

Figure 2.11: Optical microscope images of a microchannel plate surface. The channels are roughly 30 μm in diameter and are arranged in a hexagonal array. While the holes look perpendicular to the figure plane, they are actually biased at an angle of 8° from the perpendicular so that incoming particles strike the inner wall of the channels.

possible the detection of a single anion by the delay-line anode detector. This experiment utilizes a stack of two MCPs arranged with their channels running counter to each other so they form a v-shaped pattern along the edge-on cross section of the stack. This is also known as a chevron configuration.

2.3.2 Delay-Line Anode

A delay-line anode detector (Roentdek DLD80) is used to discern position information of anions incident on the MCP in this experiment. The detector utilizes the finite propagation time of the signals across a wire to determine the origin of a pulse along the wire's length. In each direction, x and y,[4] a differential pair of copper wires is wrapped helically from one corner around the detector to the opposite corner. The two wires in the pair are electrically isolated but close enough together that a shower of electrons from the MCP will form a pulse on both wires.[5] The pulse propagates away from its origin in both directions and reaches the ends of the wires at different times depending on the original location of the pulse. Thus, if

---

[4] Figure 2.8 illustrates the coordinates used throughout this work

[5] The two wires are labeled "signal" and "reference", although they only differ in that the signal wire is maintained at 50 volts above the reference wire. The differential circuit maintains the signal integrity along the length of the wire, and an electronic subtractor generates the final signal.

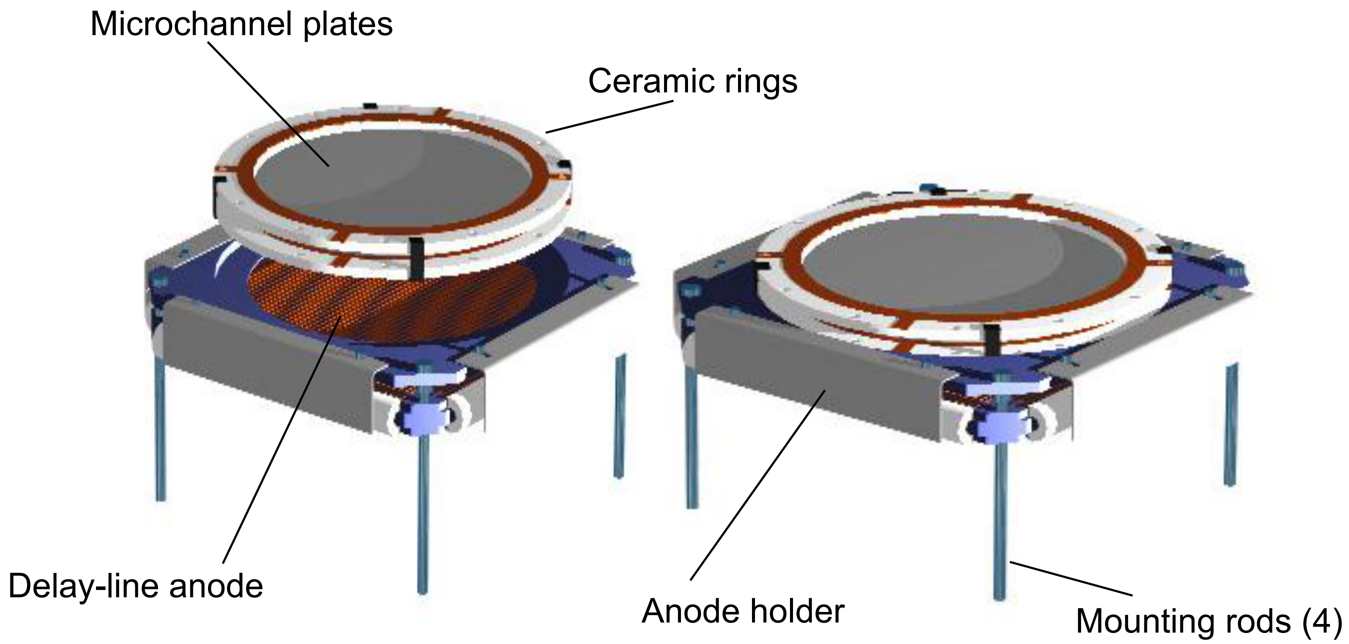

Figure 2.12: Assembly of delay-line detector with microchannel plates. The stack of plates sits over the delay-line anode grid in the assembled configuration. The plates are held in place with a pair of ceramic rings clipped together, and the entire detector assembly is mounted inside its housing via four mounting rods.

the signal originates far on one end of the wire, the signal will reach one end sooner than the other and indicate that the anion was incident nearer to that end.[6] This configuration exists for each direction so that two-dimensional position information is obtained for each ion. Again, Fig. 2.8 specifies the coordinates used throughout this work.

The configuration of voltages on the MCP and anode depends on the charge polarity of the particles to be detected. In the current negative-collection configuration, the front MCP, which is the first part of the detector that an incident particle sees, must be set at a high positive voltage (200–300 V) in order to accelerate anions toward the detector with enough energy to eject the secondary electrons. The back MCP then must be biased above that by 2100–2200 V in order to activate the MCP to accelerate secondary electrons in the plates, as described above. Then, the anode reference wires are held at a voltage still 100 V above the back MCP so that the electrons are accelerated from the MCP to the anode wires, while the signal wires are another 50 V above the reference wires. In addition, the "anode holder", the metal support structure around which the anode wires are wrapped, must be held at a voltage near to the back MCP to avoid stray fields in the region. Of course, this configuration means that only negatively-charged particles can be detected in the present configuration, which is well-suited for electron attachment measurements.

Figure 2.12 shows the construction of the MCP and delay line detector.[7] The stack of two MCPs are held together by two ceramic rings with electrical contacts and spring clips for structural support. The stack is placed on top of the delay-line anode holder inside a shallow recess to form the operational assembly of the detector unit.

In order to apply the voltages to the MCPs and anode wires, two dual-channel iseg NHQ 214M power supplies are used to maintain the bias voltages. One channel of one supply maintains the back MCP at 2200 V, while the front MCP is maintained at 300 V by connecting it to ground through a 3.7 MΩ resistor, forming a voltage divider which keeps the

---

[6] The specifics of the calculation are best left until the basics of the electronics and acquisition systems are described.

[7] Figure taken from "MCP Delay Line Detector Manual", Version 9.22.1003.1, RoentDek Handels GmbH

front MCP at the proper voltage without the use of a separate power supply. Although there are two sets of reference and signal anode wires, the voltage settings for both are equivalent, so one supply channel is used to bias both the reference wires to ∼2600 V and another channel biases both signal wires at ∼2650 V. The last power supply channel is used to bias the anode holder at ∼2500 V.

2.3.3 Timing

The reliable measurement of post-interaction momenta requires both pulsing schemes and measurement capabilities in the nanosecond regime. Figure 2.13 shows the basic timing scheme of the experiment. The largest single source of systematic timing error typically results from the timing width of the electron bunch, usually on the order of 100 ns. Since electrons from anywhere in the bunch can result in the observed interaction and the measurement presumes a point source of electrons in time, the spread in the flight times owing to the electron bunch width folds into the uncertainty in the ion momenta. In practice, the ion flight times are close to 10 μs, so ±50 ns uncertainty in the ion creation times is not necessarily a great concern.

The heart of the pulsing scheme is the SRS DG535 Pulse Generator, which can deliver sub-nanosecond triggers to pulsers for the spectrometer ion extraction plates and electron gun grid as well as synchronized signals to the analog electronics which receive the detector signals. The DG535 triggers on an internal clock at an adjustable rate of repetition usually set around 40 kHz. This device is the origin of the gating signals which coordinate the timing of the experiment by triggering various pulse-switchers and logical gates. At the beginning of each cycle, an outgoing pulse signals a pulser to bring the electron gun grid to 0 V, thus allowing passage to electrons arriving at the grid during a set window, after which the pulse ends and the beam is cut off. After a set interval of time, called the *delay time* or *drift time*, a pulse from the DG535 then triggers a pulser to bias the spectrometer plate to the set voltage to extract the ions formed by dissociation. After enough time has passed to ensure

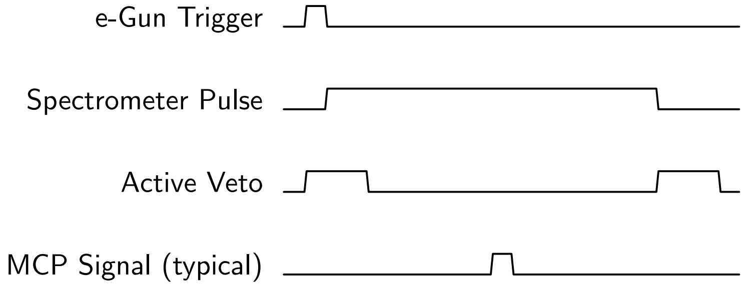

Figure 2.13: Timing diagram for the pulsing sequence. The electron gun trigger (width ∼100 ns) is the reference point starting the timing sequence, setting the time zero. The spectrometer pulse is activated shortly after the electron gun pulse (lasting ∼10 μs), and a signal veto covers the time during which the spectrometer pulse is turned on and off to ignore interference effects caused by the rapid pulsing of the spectrometer field. A typical MCP signal would arrive ∼5–8 μs after the electron gun trigger.

that all anions have left the interaction region, usually ∼15 μs, this pulse then ends and the entire cycle begins over again, after one period of the cycle has passed. Between the end of the electron gun pulse and the beginning of the spectrometer pulse, anions formed at the interaction point are allowed to drift away from their original position given their post-interaction kinetic energy. This delay time is crucial to producing a detector image with enough resolution to see the internal structure of the momentum distribution. This necessity also illustrates the difficulty in imaging interactions with a very small release of kinetic energy.

The flexibility of the pulsing setup is important to overcoming various challenges particular to the experiment. For instance, the pulse on the spectrometer pusher plate causes a corresponding noisy signal on the MCP wire which drowns out any signal caused by actual hits on the detector. Since there is no immediate way to extract the real signal out of the noise during this part of the pulsing cycle, an effective "dead time" in the acquisition window is created just after the spectrometer pulse's beginning and end. In practice, this effect is not very prohibitive for ions heavier than H^-, since flight times tend to be far away from the noise in time. Still, an electronic veto is implemented so that false signals are not delivered to the acquisition system every time the spectrometer pulses. The specifics of the veto will be made clearer within the context of the electronics system in the following section.

2.3.4 Electronics

The analog electronics system serves as a bridge between the raw signals from the detector and the acquisition computer.[8] Signals from the MCP and delay-line anode are interpreted only by their relative positions in time as they arrive at the acquisition machine, so maintaining consistent signal pathways across all channels while being aware of delay contributions from the electronics themselves is a necessity. The ultimate destination of the signals originating from the detector is the time to digital converter (TDC) PCI card which detects and records pulses arriving from the electronics and relays them to the acquisition software in the computer. Figure 2.14 illustrates the flow of the signals through the electronics system. In the center is the TDC card which receives the processed signals from the detector in addition to copies of triggering signals for the electron gun and spectrometer which will be used to determine the ion flight times.

The signals which originate with the MCP are connected to a Roentdek FAMP8 fast amplifier with 8 signal channels with adjustable gain and complementary outputs. The amplified signal is sent to a Phillips 715 constant fraction discriminator (CFD). The role of the CFD in the signal processing is important since the TDC will only consider the time of signal arrival and not the amplitude of the signal. To simply assign arrival times by noting the time at which a pulse reaches a particular voltage level would not be ideal, since the trigger time would depend on the variable peak height of the pulses. Rather, a CFD utilizes electronic comparators and a logical AND gate to instead trigger a pulse when it reaches an adjustable fraction of its total height. This causes pulses to be triggered at the same time regardless of their particular peak height. Since the experiment relies on accurately measuring the pulse times, a CFD is necessary to properly compare the signal times as well as providing the TDC

---

[8] The electronics system is housed in a Nuclear Instrumentation Module (NIM) bin which connects the power supply and logic modules via BNC and LEMO connectors.

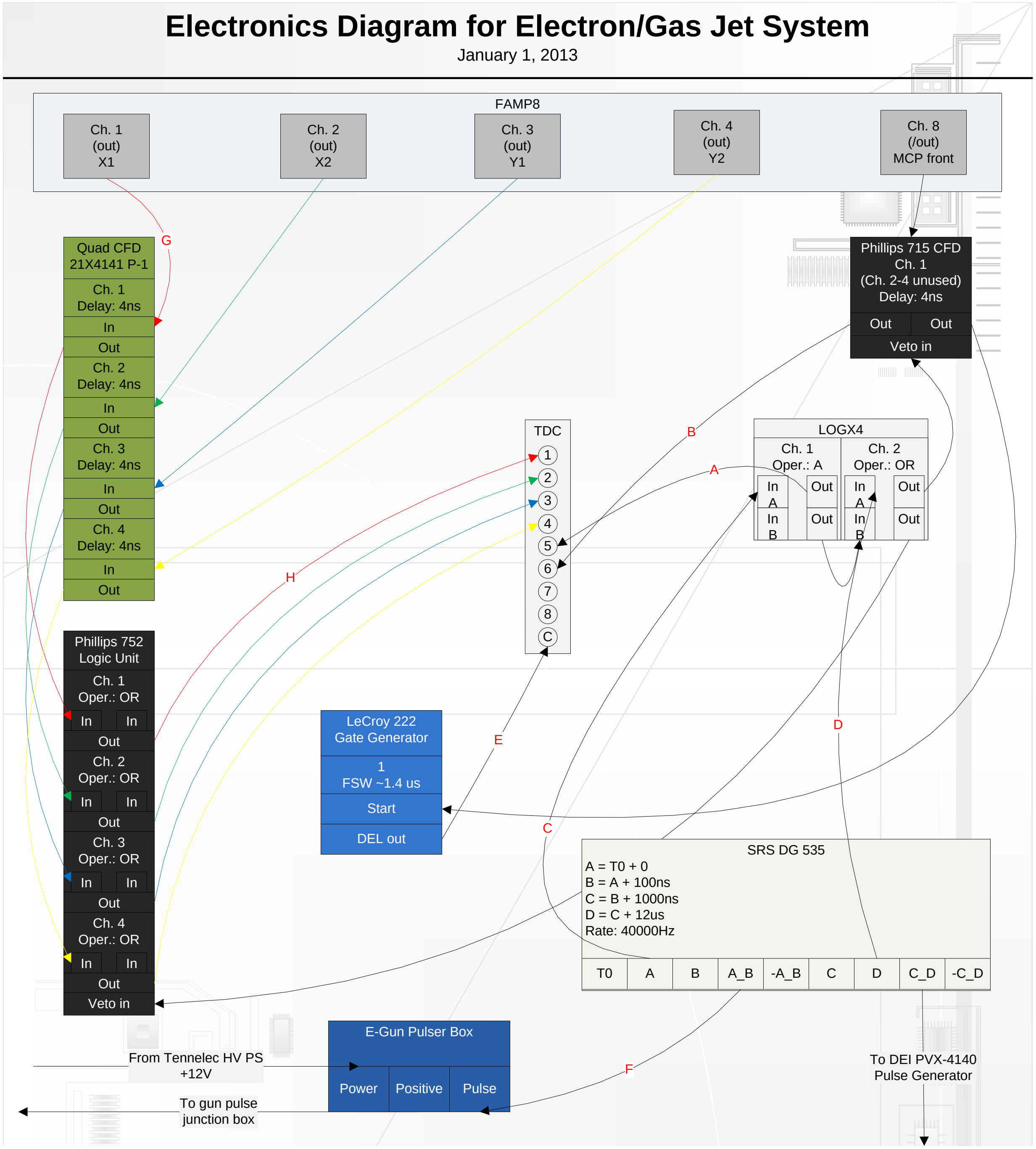

Figure 2.14: Data flow diagram of the electronics system including main components. The signals from the detector (G) are amplified by the FAMP8 and are relayed to constant-fraction discriminators (CFDs, in olive and black) to set a discrete time value for each pulse. The resulting pulses (H) are then sent to the TDC card (at center). The DG 535 timing box triggers (C and D) a veto signal (based on the turning-on and off of the spectrometer pulse) from the LOGX4 logic box which voids output in the CFDs while the veto is high. The DG 535 also triggers (F) the electron gun pulser box to control the electron beam. The Lecroy 222 (light blue) creates a delayed MCP signal for common stop mode, defining the acquisition window.

with sharp-edged pulses with normalized heights. An important part of utilizing the CFDs is properly tuning their triggering thresholds to exclude line noise and random pulses while not excluding real events from inclusion in the data.

The signals from the delay line anode, which originate as a signal and reference pulse, are sent through an electronic decoupling box which produces a single, differential signal which is then sent to the FAMP8 amplifier. Similar to the MCP signal, the four delay line signals (x_1, x_2, y_1, y_2) are also sent to separate channels of a CFD, after which they are sent to a Phillips 752 Logic Unit which is used as a simple pass-through for its veto capability. The CFD used for the MCP signals features a veto input which allows the suppression of signals that arrive during a particular part of the pulsing cycle. This is necessary to combat the interference mentioned in the Timing section. Using the LogX4 module in Fig. 2.14, a short pulse ($\sim$100 ns) is generated when the electron gun is fired, and then again when the spectrometer pulse is turned off, creating a two-peaked pulse pattern. This is illustrated with the other main timing components in Fig. 2.13. When this logic-level signal is relayed to the veto input of a CFD or logic module, that module inhibits output while the veto pulse is high. Thus, noisy signals which arrive while the veto is high will be ignored by the electronics, leaving an acquisition window in between the two veto peaks where actual detection can occur. The actual acquisition window is 10–15 μs long, while flight times for a particular ion species vary by less than 1 μs, so capturing all the ions within the window is usually not of great concern.

Since the CFD used for the delay-line signals does not have veto capability, the signals are passed after discrimination onto the Phillips 752 Logic Unit where the veto is implemented. After the logic unit, the four delay-line signals go to the first four channels of the TDC card where the times are recorded. By contrast, the MCP signals go through the Phillips 715 CFD where they are also vetoed, and the resulting signals are relayed onto channel 5 of the TDC card. The TDC operates in a *common stop* mode in which a received signal must be split and delayed, after which the delayed signal triggers the TDC to look back in time through its memory and write any events to the data file. This will be further explained in the section on acquisition, but for now it should suffice to say that a copy of the MCP signal from the CFD is also sent to a gate and delay generator (LeCroy 222) and then sent to the last channel of the TDC, labeled channel “C”. The delay generated therein need only be long enough to cover the acquisition window created by the electronic veto discussed above.

Before continuing, an aside about the DG 535 is warranted. The DG 535 is a versatile pulse generator and timing box which forms the heart of the experiment’s timing system. It can deliver two pulses per cycle of controllable position and width, (A-B) and (C-D), as well as their complementary pulses (the same pulses with negative voltage). In addition, it can provide short pulses of fixed width at the beginning and end of the two pulses, effectively signaling the rising and falling edges. Since some electronics need to be triggered at the beginning of a pulse, such as the veto electronics triggering at the beginning of the electron gun trigger pulse, these additional outputs are useful. Now, the A output of the DG 535 signals the rising edge of the electron gun trigger pulse (A-B), so it is used to trigger channel 1 of the LogX4 to form the first pulse in the veto. The veto needs to end when the spectrometer pulse (C-D) ends, which is signalled by channel D of the DG 535. This signal, then, is sent to the LogX4’s channel 2 along with the signal from its own channel 1 to form the second pulse in the veto via a logical OR gate.

The signal from channel A to the LogX4 also has a copy of it sent to channel 5 of the TDC. The TDC is set to interpret channel 5 as its time start channel, meaning that the signal arriving at that channel needs to come at a fixed time for each cycle because it is the “time zero” against which all the other signal times will be measured. The flight times are calculated by subtracting the MCP signal time from this channel 5 time. The acquisition section will elaborate on this point. This method is based on the idea that the time of ion formation is the same as the time that the electrons are released from the gun, which is not exactly correct. However, the transit time of the electrons from the gun to the interaction region is very small compared to the ion flight times, even at low electron energies, so this is not of concern. And, in any case, this delay would be a constant time added to all flight times as an offset, so the effect folds into a larger offset which is the result of electronic delays and signal propagation times which are accounted for in offline analysis anyway.

The first pulse generated by the DG 535 during each cycle is the electron gun trigger which comes from its channel (A-B). This pulse triggers the electron gun pulser box (HV-1000) to send the positive voltage to the electron gun pulse junction box which biases the grid from negative voltage back to zero volts and allows electrons through. Any anions formed from the electron beam/gas jet interaction would be produced at approximately this time. After a controllable time delay, during which any created anions with nonzero kinetic energy would begin to drift away from the interaction point, channel (C-D) triggers the spectrometer pulse generator (PVX-4140) to switch on the spectrometer's electric field. The anions at this point would be extracted towards the detector by the field until they leave the acceleration region and enter the field-free drift region where they will maintain their momentum until landing on the front face of the detector. The pulse (C-D) is made long enough to ensure that any anions will be out of the acceleration region before time D, after which the field is again turned off until a full period of the cycle has passed.[9]

As noted above, the signals from the MCP and delay-line anode take a finite amount of time to travel through the electronics system before being detected by the TDC. Since only the time *difference* between pulses is used to determine ion flight times and positions, this electronic delay has no effect so long as all signals have the same offset. To this end, it is important that all the cables which carry the signals from the detector to the electronics system have the same length, so as not to introduce differing delays for the various signals. Specifically how this is related to the calculation of ion flight times and positions will be discussed in the following section.

---

[9] For a cycle rate of 40000 Hz, the period would be 25 μs.

2.4 Acquisition and Analysis

As the final destination of the analog signals from the electronics, the TDC card is the beginning of the data acquisition system and a bridge to the data collection software. The software CoboldPC[10] 2008 interfaces with the TDC, writes the data to a *list-mode* file, and plots histograms for online diagnostics and preliminary analysis. The list-mode file contains an array of the individual events written sequentially, where each event consists of a series of numbers which represent the time of arrival of a pulse. As stated above, the times are with respect to the "zero time" defined by the electron gun trigger signal. An *event*, then, is one ion incident on the detector which is represented by an MCP signal indicating its time of arrival and four anode wire signals which are used to determine the ion's position. The anode wire signals arrive shortly after the MCP signal and their relative positions in time are used to calculate the anion's position. Recording and handling the data in list mode is a significant advantage to analysis and diagnostics as compared to using histogrammed data without access to the raw signal information. This allows the methods and calibration used to calculate detector positions and times of flight to be altered offline without reperforming the experiment.

Since the TDC records and writes raw data in list mode, the CoboldPC acquisition software must do the job of constructing physically meaningful values like ion time-of-flight (TOF) and position. The signal from the MCP is used as the time reference for the anode signal calculations, so t_{x1} represents the amount of time taken after the MCP signal is received for the signal from the x_1 wire to arrive, t_{x2} represents the time until the signal from x_2 arrives, and so on. Thus, the x and y positions of an ion on the detector are given by

$$x = v_\perp(t_{x1} - t_{x2}) \quad \text{and} \quad y = v_\perp(t_{y1} - t_{y2}) \tag{2.10}$$

---

[10] RoentDek Handels GmbH

where $v_\perp$ is the signal propagation speed across the anode wire grid. For the 80 mm diameter detector used in this experiment, which has a wire pitch of 1 mm, the propagation time for one pitch is 1.95 ns, so that $v_\perp$ is approximately 0.5 mm/ns. This means that the signal propagates across the face of the detector at a rate of 0.5 mm for every ns after the initial signal is generated. Calculating the position from the time difference gives the position of the particle with the origin at the center of the detector. Although the software requires all four anode signals to be received in order to calculate a position, this is somewhat redundant since the position from the edge of the detector in one direction can be calculated from just one signal, but the redundancy allows for a check against positions implied by random pulses which pass through the electronics system. Figure 2.15 shows the hit frequency on each anode channel when an MCP signal is detected. These data help to determine if the analog electronics are set properly to allow all the necessary signals to be detected while rejecting as much noise as possible.

While the time difference between anode signals is used to calculate anion positions, the time *sum* is a constant which depends on the total length of the wire. Since this is unchanging, the time sum can be used to determine whether pairs of signals in the x or y direction are actual ions or simply chance occurances of random pulses near to each other in time. Figure 2.16 shows the time sums as a function of position on the detector. The time sums should be very nearly constant across the detector for real signals, allowing them to be distinguished from the noise. Typically, the vast majority of events have a time sum within a very narrow range of values, usually around 50 ns. While the actual value of the time sum does not matter, since delays in the electronics and cable lengths add to it arbitrarily, the distribution of values for the time sum should be single-peaked and narrow.

Since random signals and line noise are an inevitable part of the data acquisition, some filtering is required to expose the desired structures in the data. In order to calculate a reliable ion flight time and position, the MCP signal and all four anode wire signals are

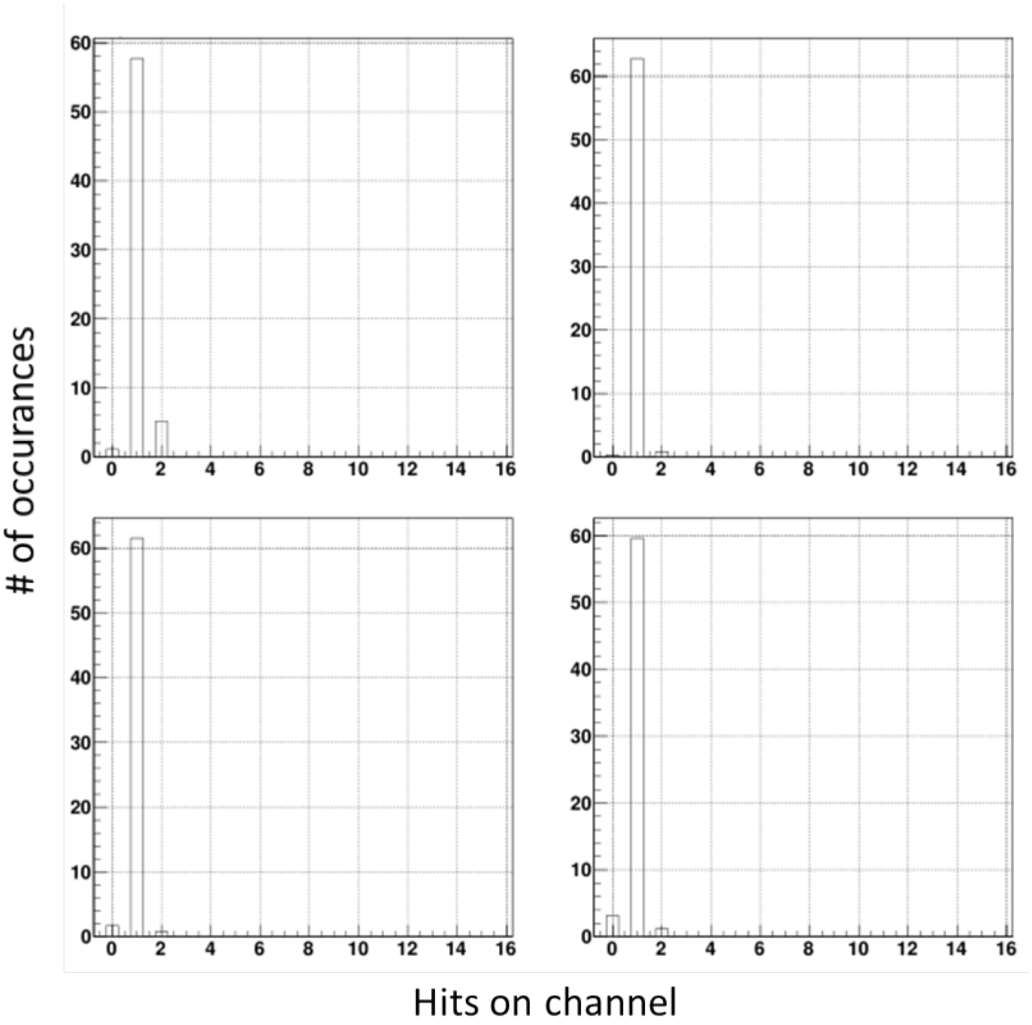

Figure 2.15: Histogram of hits on anode channels: x_1 (top-left), x_2 (top-right), y_1 (bottom-left), y_2 (bottom-right). The x axes indicate the number of hits on each anode wire (for each signal received on the MCP), while the y axes are the number of occurences of each number of hits for every MCP signal received. Ideally, every hit by the MCP would result in one hit on each anode wire, meaning that MCP signals actually result in anode wire signals and that noisy anode signals don't cause double-triggering (as indicated by values greater than one). As a diagnostic, the vast majority of entries should be in the "1" bins.

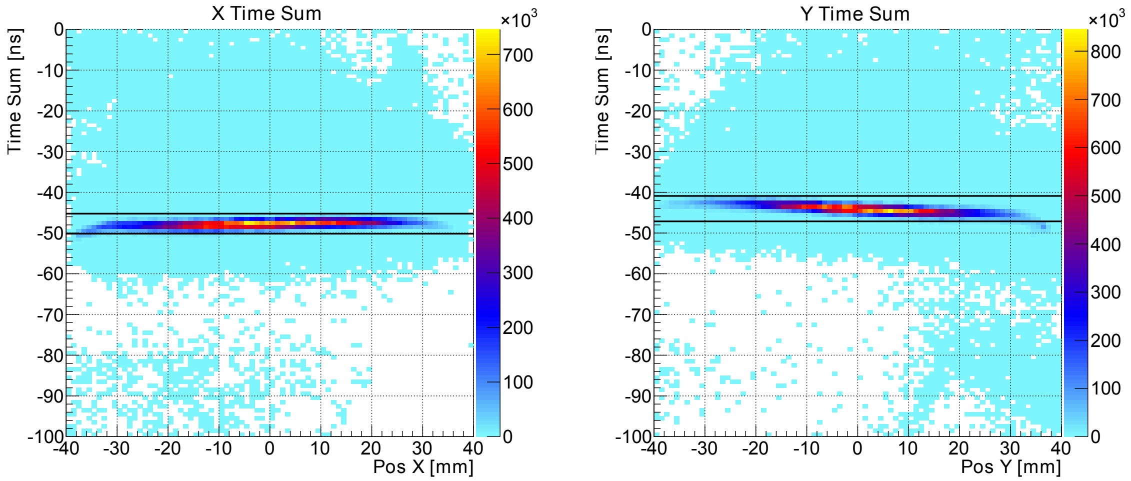

Figure 2.16: Time sum plots for X (left) and Y (right). The sum of the signal times on a particular wire (X or Y) should be constant across the detector for real events, so a gate can be set to distinguish these real events from noise. The areas between the horizontal black lines contain the data that are kept during the analysis. The raw signal times are negative because they are measured with respect to the MCP signal time as the TDC looks back in time through the acquisition window.

required. Each of the five signal channels are monitored independently to ensure that all channels are usually triggering concurrently.

The CFD thresholds are manually adjusted and must be tuned such that the maximum number of actual events are collected while random signals are rejected. To this end, each of the anode channels x_1, x_2, y_1, y_2 is assigned a value 2^n with $n = 0, 1, 2, 3$, respectively, forming a binary string of value between 0 and 15. Then, as a diagnostic, a histogram of the decimal value of each event is filled to demonstrate which channel, if any, requires adjustment. For example, a value of 9 would indicate that all signals arrived *except* for channels x_2 and y_1, which have values 2 and 4, respectively. A value of 15 indicates that signals on all four anode wires and the MCP signal were detected, which is the ideal scenario.

Once the acquisition software and detector electronics are prepared, the data specific to the experiment may be observed. In a dissociative attachment experiment with one ionic product, this usually consists of a time-of-flight histogram, images of the ion positions on the detector, and plots which relate the position to the flight time for each dimension. For multi-particle coincidence measurements of dissociative ionization products, additional data correlating the individual fragments' flight times and positions is of interest. Most of the momentum and energy calculation is performed offline, but these basic figures provide a good view of the preliminary data and also help determine whether the simulated experimental parameters regarding pulses and timing, which will be discussed in the next chapter, form a viable configuration.

3 — Simulation and Analysis

> ”It’s funny, you live in the universe, but you never do these things until someone comes to visit.”
>
> –*John A. Zoidberg*

At this point, it should be apparent that the performance of the spectrometer is sensitive to differences in parameters such as ion kinetic energy, mass, target size, and the specific timing of the pulsing scheme. A configuration that works for one particular anion with its corresponding energy and mass is not guaranteed to work for another species. Therefore, simulations of the spectrometer operation are required to make an educated guess about the best settings for a desired experiment. This is done using several different software packages, including mainly SIMION, an ion-optics simulation program, and Microsoft Excel, which is used to run a classical trajectory simulation of the ion flights using custom spreadsheets. The particular conditions required by the simulation to produce a workable configuration will be the central focus of this chapter, and it may be that, for a given spectrometer geometry, *no* particular configuration is viable, and the geometry of the spectrometer must be physically changed, which is a more invasive and time-consuming procedure. Thus, the predictions afforded by simulating the experiment in this way are of great importance. The specifics of the analysis method used for the presented data are given in Appendix B. The data visualization package ROOT,[77] as well as the analysis software LMF2Root,[78] and the acquisition program Cobold PC[79] will be integral to this discussion.

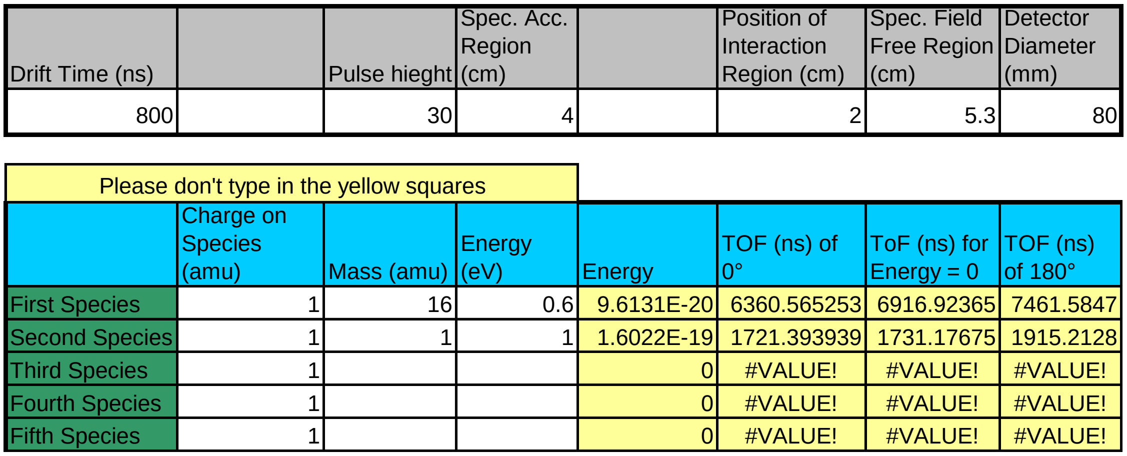

Drift Time (ns)		Pulse hieght	Spec. Acc. Region (cm)		Position of Interaction Region (cm)	Spec. Field Free Region (cm)	Detector Diameter (mm)
800		30	4		2	5.3	80

Please don't type in the yellow squares

	Charge on Species (amu)	Mass (amu)	Energy (eV)	Energy	TOF (ns) of 0°	ToF (ns) for Energy = 0	TOF (ns) of 180°
First Species	1	16	0.6	9.6131E-20	6360.565253	6916.92365	7461.5847
Second Species	1	1	1	1.6022E-19	1721.393939	1731.17675	1915.2128
Third Species	1			0	#VALUE!	#VALUE!	#VALUE!
Fourth Species	1			0	#VALUE!	#VALUE!	#VALUE!
Fifth Species	1			0	#VALUE!	#VALUE!	#VALUE!

Figure 3.1: Section of Excel ion flight simulation spreadsheet. The spreadsheet creates ions of the desired energy at the interaction point, applies the designated electric field, and calculates the position, momentum, and acceleration of each ion at every time step (0.5 ns) to simulate the flight. Ions are flown in an isotropic circle so the spread of the distribution due to ejection angle is also simulated.

3.1 Spectrometer Simulations: Excel and SIMION

In order to simulate ion flight times and their corresponding positions on the detector, a custom Excel spreadsheet (developed at Auburn University by Joshua Williams) is used to calculate the electric field and the resulting force on the ions at minute time steps (0.5 ns) such that the ion trajectories are determined incrementally. The spreadsheet takes into account the basic geometry of the spectrometer while ignoring the full, three-dimensional environment surrounding the interaction region which includes asymmetric contributions to the field shape by other electrically conductive components of the experiment. These components will tend to perturb the field slightly from the ideal configuration presumed by the Excel simulation, so that effects such as field leakage, fringe effects, and non-uniformity are not accounted for. Generally, these effects are small and the Excel simulation serves as a

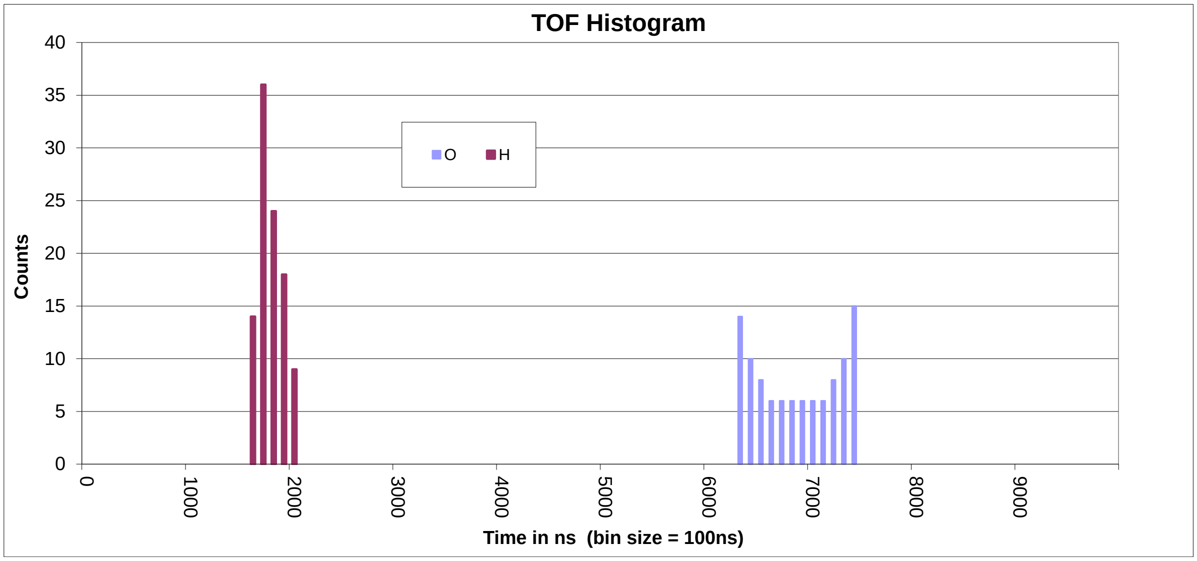

Figure 3.2: TOF histogram from Excel simulation. The two distributions correspond to two species being flown in the spectrometer: H^- with 1 eV kinetic energy (red) and O^- with 0.6 eV kinetic energy (blue). The higher mass species will arrive at the detector later (with a longer flight time) and with a broader distribution in time due to the lower acceleration in the spectrometer. In order to maximize time resolution, the distribution should have a spread of 0.5–1 μs.

quick and effective tool to determine approximate spectrometer characteristics before more comprehensive methods are used.

Figure 3.1 shows the front end part of the spreadsheet where information about the spectrometer geometry and pulse configuration is entered (top row). This configuration assumes an extraction field that stays on until the ions have left the acceleration region, so the pulse length is not declared explicitly.[1] The lower box contains information about the ions, several different species of which can be flown. The present experiment is primarily concerned with single anions, so only one mass is specified in the second column. A mass of 16 (amu) is used to simulate oxygen anions with an initial kinetic energy of 0.6 eV. Protons of 1 eV kinetic energy are also included for comparison. The spreadsheet then flies ions in

---

[1] An alternative method is to pulse the field briefly to “kick” the ions, giving each the same impulse regardless of initial direction, for which a short pulse duration would be specified.

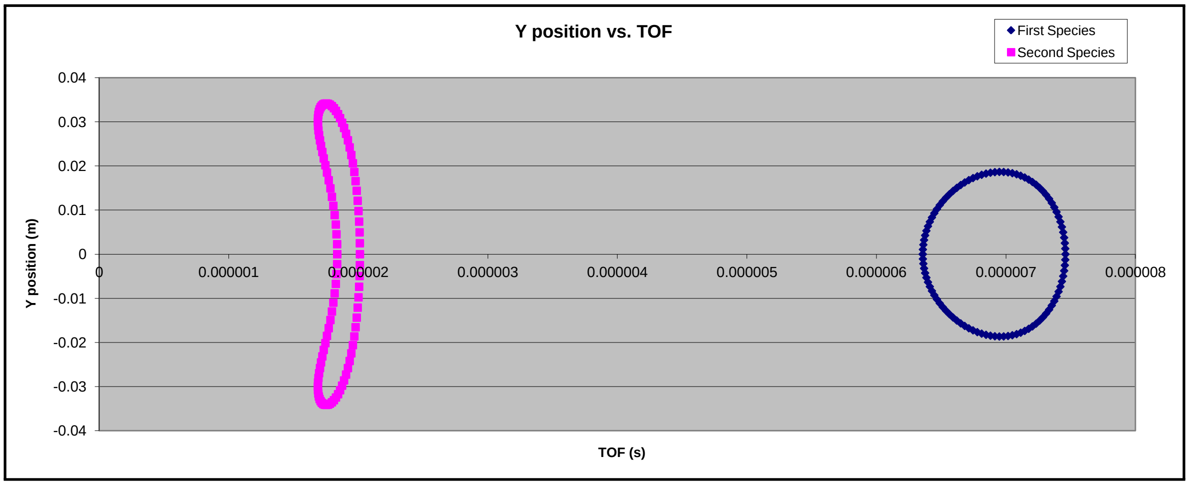

Figure 3.3: Position vs. TOF for simulated ions. The blue distribution (O^-) is spread out in time and there is a single-valued relationship between time-of-flight and detector position on the top (or bottom) half of the detector. Therefore, the initial momentum of those ions in the time-of-flight direction may be determined from their time-of-flight alone. In the pink distribution (H^-), ions landing at different places on the detector land at the same time, so that the ions' initial momenta cannot be uniquely determined from just the time-of-flight.

a circular array to represent initial momentum in the full range of angles in a plane perpendicular to the detector plane. The result of the calculation is the time of flight (TOF) of the ions as a function of their initial angle. This information is necessary to determine if the TOF of a particular ion can be used reliably to calculate the initial momentum direction and magnitude.

Figure 3.2 shows the resulting time of flight distribution for the settings in Fig. 3.1. Approximately the first 1 μs of the time in the graph falls within the electronic veto discussed in Chapter 2, so one requirement is that no part of the TOF distribution of the ions falls within that short time range. Any ions landing inside the veto will have their signals rejected and thus, in the actual observed TOF data, the distribution would be cut off on its lower end. Also, a larger spread in the TOF distribution is typically better since it affords greater resolution in the resulting momentum calculation in that direction.

Since the detector is of finite size (80 mm diameter), the simulation also helps ensure that all ions land on the detector, regardless of their initial direction. The blue distribution in Fig. 3.3 is typical of ions with constant kinetic energy formed inside such a spectrometer.

The key characteristic in this plot is that the distribution be constrained in position to well within ±40 mm in position, thus confining all ions to land on the detector, and that the distribution have a shape that is single-valued in each half (top and bottom) of the detector. For a distribution such as the pink in Fig. 3.3, many ions arriving at different positions on the detector will have the same time-of-flight. If the distribution in detector position is not a single-valued function of time, then the time-of-flight momentum will not be able to be determined just based on the time-of-flight. In this case, the time information would not yield an unambiguous momentum in the time-of-flight direction.

In some configurations, the position vs. TOF distribution may appear with a concavity in its side, as with the pink in Fig. 3.3, which would indicate that ions initially moving *away* from the detector would reach the detector *before* their counterparts that moved *towards* the detector initially. Since there is no force in the y (and x) direction, the y position on the detector is closely related to the initial velocity in the y direction (via the mass and TOF), while the relationship of the TOF itself to the TOF velocity also depends on the pulsing scheme. The purpose of plots like that in Fig. 3.3 is to ensure beforehand that this relationship is single-valued.

The pink distribution in Fig. 3.3 can result from the electric field magnitude being too high, such that ions that spend more time in the acceleration region are accelerated enough that they catch up and surpass ions that are initially directed towards the detector. Since ions that initially move away from the detector must be turned around, and because the ions typically have a finite kinetic energy, the ions that move away initially may emerge from the acceleration region with greater velocity than the ions that initially move towards the detector. With a long enough drift region, these faster moving ions can overtake the slower ones, destroying the regular relationship between TOF and initial velocity in the TOF direction. In such a case, the initial momentum in the time of flight direction would not be derivable from the ion's TOF.

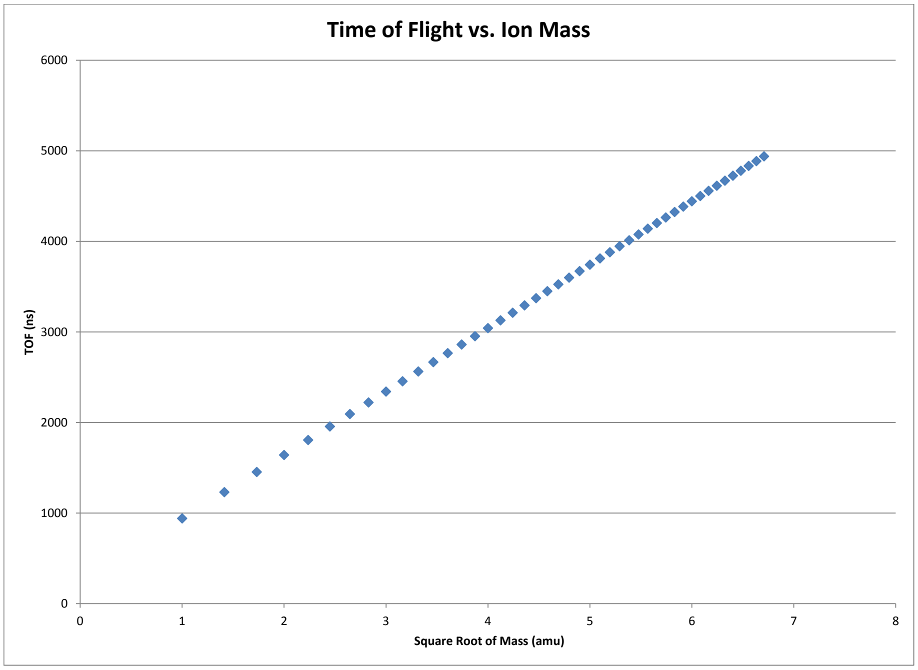

Figure 3.4: TOF vs. $\sqrt{m}$ for masses up to 45 amu. The TOF scales linearly with the square root of the mass-to-charge ratio in the current spectrometer scheme. In this way, unknown peaks in the TOF spectrum can be identified more easily against peaks for known masses.

In order to calibrate the experiment and have some expectation of where masses land in the TOF spectrum, the dependence of the TOF on the ion mass is helpful. In the current pulsing configuration in which the spectrometer pulse is kept on until the flight of the ions is complete, the kinematics of the spectrometer result in a linear relationship between the TOF and the square root of the mass of the ion. This is demonstrated by flying an array of integer masses (1-45 amu) and plotting their TOF, as in Fig. 3.4. If the spectrometer is used in the pulsed configuration, as alluded to above, the TOF would be proportional to the mass itself, although this configuration has not been used for the presented data. In either case, this information is important because it aids in the identifying of peaks in the actual measured TOF distribution, which will see contributions from not only from the DEA interaction of interest but also from background particles which land on the detector incidentally.

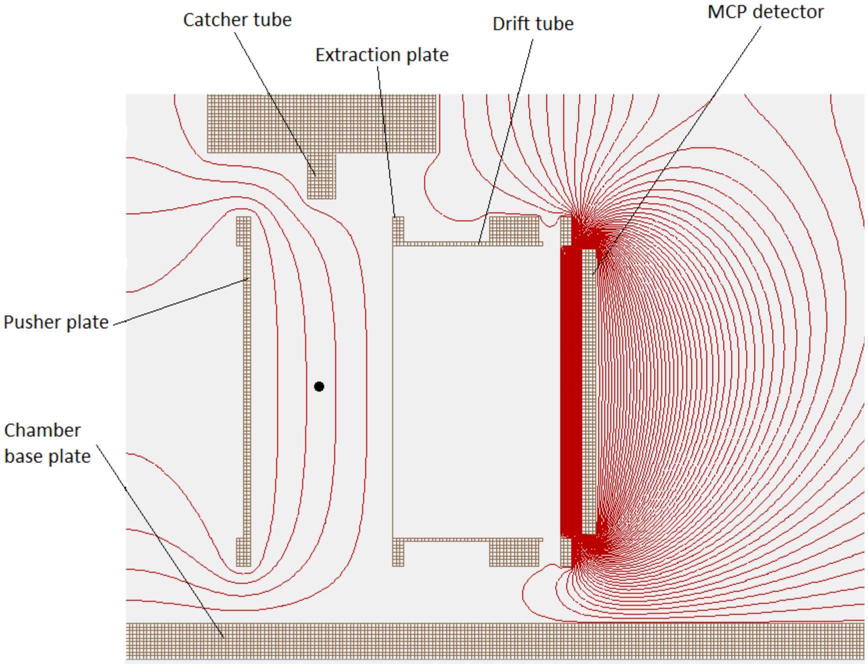

Figure 3.5: Simulation of the isopotential curves in the spectrometer during pulsing. Shown is a 2D view cut through the center of the spectrometer. The electron beam points into the page at the location of the black dot, with the Faraday cup in line with the beam.

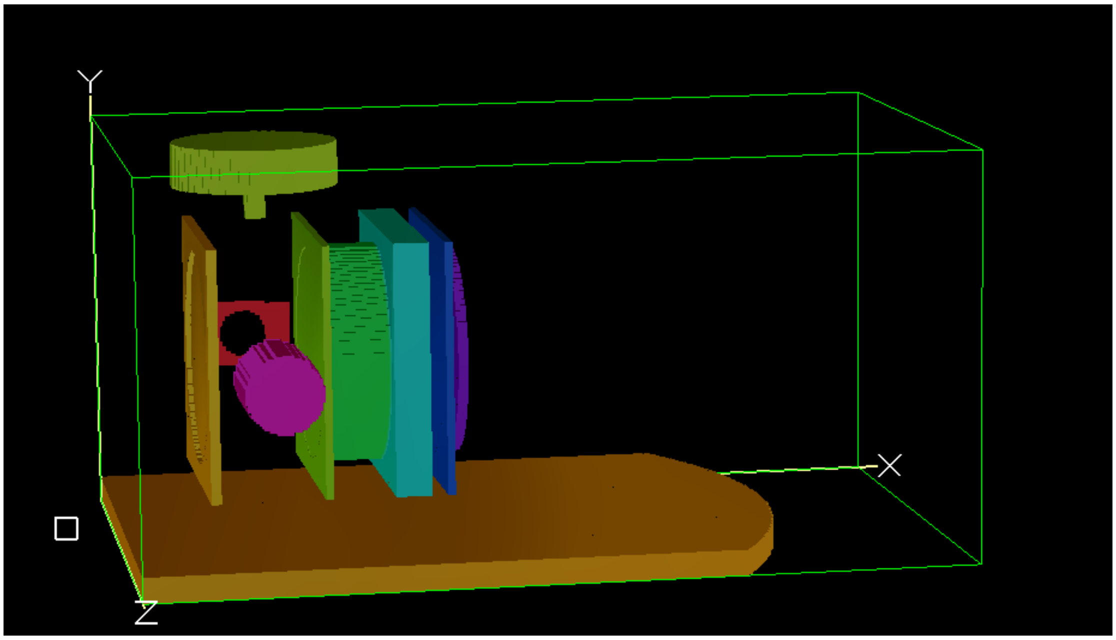

Figure 3.6: 3D model of the spectrometer for SIMION showing the spectrometer and surrounding conductive surfaces, including the electron gun (pink), the Faraday cup (red), the jet catcher (light green, top), and the MCP (purple).

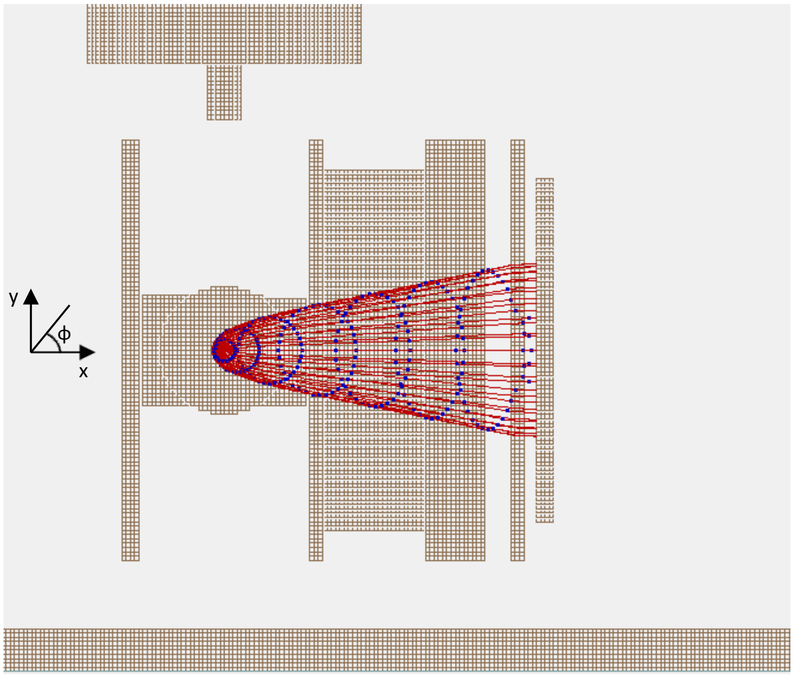

Figure 3.7: Flight paths of 0.55 eV O^- ions in SIMION. Blue dots indicate 1 μs time markers. The coordinates indicated in the figure are those used by SIMION and are different from those in the rest of this work. The elevation angle ϕ is measured from the horizontal. The ring of blue dots should not fold over as it propagates to the detector in order to maintain a single-valued relationship between TOF and momentum.

As stated above, several effects are not considered in the above simulation. One is any slight asymmetry or nonuniformity in the electric field lines resulting from objects surrounding the spectrometer. Another is that the size of the target is small but finite and not confined to a single point. Both of these points will be elaborated upon below, but the advantage of SIMION is that it calculates a numerical solution to Laplace's equation based on the potential surfaces provided to it. The entire spectrometer, including the pusher and extraction plate, drift region plates, detector mount, and the face of the detector itself are modeled as well as other objects such as the front face of the electron gun, the Faraday cup, the catcher tube, and the base plate upon which the spectrometer sits. Since these surfaces are grounded, they effect the shape of the field lines and are modeled to make sure the field is flat and symmetric in the interaction region. The surfaces and objects are defined functionally in a geometry file, imported into SIMION, and used to construct a set of "potential arrays" which the program then "refines" (solves Laplace's equation), and a workbench is then created which can fly ions, draw their trajectories, and output to a spreadsheet the results of the simulation. The left of Fig. 3.5 shows the simulation of the field structure in the spectrometer. The field in the center of the spectrometer, where ions are created, must be fairly flat and symmetric. The drift region should be field free, and the high field region on the right of the image results from the high voltage (350 V) on the front face of the detector intended to accelerate ions onto the channel plates. Figure 3.6 shows a 3D view including the model of the electron gun, catcher, and detector.

An advantage of this software is that the use of the Lua programming language allows "User Programs" to be written which instruct the software on how to handle flight parameters during the simulation. This means that the pulsing of the spectrometer need not be a simple on/off model, but can be defined functionally to more closely resemble the actual pulse shape, which is an imperfect step function in reality. Because the pulse is only 30 V and stays on for 10 μs, the rise time is a small fraction of the total pulse, so here a simple linear slope model is sufficient. The software is thus instructed to vary the voltage linearly for the chosen "turn-on time", then stay flat for the rest of its duration. Several adjustable variables declared by the user program allow the pulsing parameters, such as the pulse height, length, and delay, to be varied for each simulation. Also, the user program generates an Excel spreadsheet to record the simulation results. The source code of the user program is provided in Appendix C.

Figure 3.7 shows the flight paths of O^- ions with 0.55 eV kinetic energy to simulate anions from attachment to CO_2. The ions are flown at incremented angles about the normal to the figure plane, and the blue markers indicate the position of each ion every 1 μs, so the shape of the blue ring should approach that of Fig. 3.3. Of note is the fact that the distribution changes shape but can be scaled functionally to recover the distribution just after the ions' creation, and that the distribution covers enough of the detector for its shape to be discerned with 1 mm resolution. Figure 3.8 includes the simulated data (generated by the SIMION user program) about the individual ions.[2] The elevation angle is measured with respect to the $\pm x$ axis, which is horizontal and in the plane of Fig. 3.7, so the angles run from 0 to 90 degrees for ions moving towards the detector (distinguished by initial $p_x > 0$), then from 90 back to 0 degrees for ions moving away (initial $p_x < 0$). A key figure is the difference between the highest and the lowest time-of-flight. If all the ions land too close to each other in time (closer than $\sim$100 ns), the finite resolution of the experiment may make it difficult to distinguish them, and slicing the data by restricting the TOF would not be possible if all the times were collapsed to within the TOF resolution. This simulation shows a TOF spread for the entire distribution of roughly 1 μs, which is typically more than enough. These data only show flights above the x axis, which is why all the "Initial Py" values are positive, but by symmetry, the table would repeat itself for the other half.

As discussed in Chapter 2, the size of the supersonic jet at the interaction region can be calculated to be of roughly 1.5 to 2 mm in diameter. The size of the electron beam spot at the interaction region can be expected to be roughly 1 mm in diameter, although there is

---

[2] In SIMION, the x direction is the time of flight direction (perpendicular to the detector), while in the analysis x will be in the detector plane (along the electron beam direction), and the time of flight axis is called t. Surely this will cause *no* confusion.

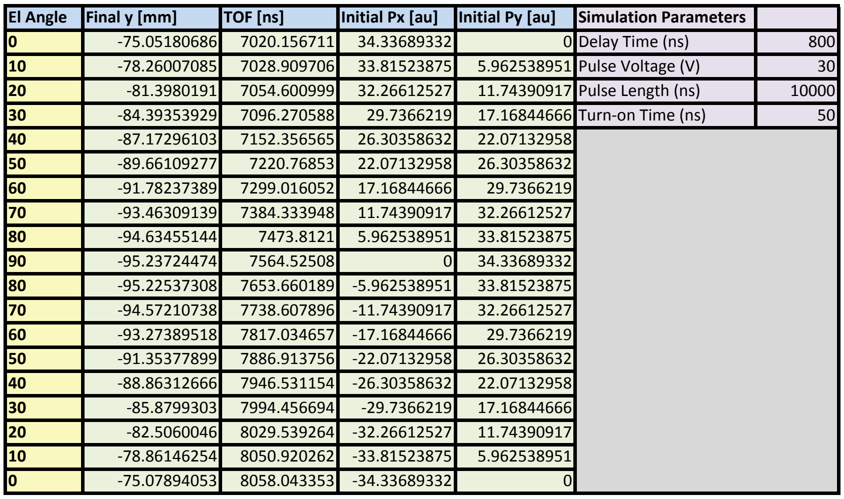

El Angle	Final y [mm]	TOF [ns]	Initial Px [au]	Initial Py [au]	Simulation Parameters	
0	-75.05180686	7020.156711	34.33689332	0	Delay Time (ns)	800
10	-78.26007085	7028.909706	33.81523875	5.962538951	Pulse Voltage (V)	30
20	-81.3980191	7054.600999	32.26612527	11.74390917	Pulse Length (ns)	10000
30	-84.39353929	7096.270588	29.7366219	17.16844666	Turn-on Time (ns)	50
40	-87.17296103	7152.356565	26.30358632	22.07132958		
50	-89.66109277	7220.76853	22.07132958	26.30358632		
60	-91.78237389	7299.016052	17.16844666	29.7366219		
70	-93.46309139	7384.333948	11.74390917	32.26612527		
80	-94.63455144	7473.8121	5.962538951	33.81523875		
90	-95.23724474	7564.52508	0	34.33689332		
80	-95.22537308	7653.660189	-5.962538951	33.81523875		
70	-94.57210738	7738.607896	-11.74390917	32.26612527		
60	-93.27389518	7817.034657	-17.16844666	29.7366219		
50	-91.35377899	7886.913756	-22.07132958	26.30358632		
40	-88.86312666	7946.531154	-26.30358632	22.07132958		
30	-85.8799303	7994.456694	-29.7366219	17.16844666		
20	-82.5060046	8029.539264	-32.26612527	11.74390917		
10	-78.86146254	8050.920262	-33.81523875	5.962538951		
0	-75.07894053	8058.043353	-34.33689332	0		

Figure 3.8: Spreadsheet with output of SIMION simulation for O^- with 0.55 eV initial kinetic energy. The angles in the top half of the table are measured with respect to the $+x$ axis, while the angles in the bottom half are measured with respect to the -x axis, referenced with respect to the initial momentum vector. The maximum minus the minimum values of the TOF give the spread in that direction, which is roughly 1 μs in this case. The TOFs should also increase monotonically for decreasing values of "Initial Px [au]".

no direct measurement of its size. Ultimately, this means that ions can be created anywhere inside that volume which is defined by the spatial overlap of the gas jet with the electron beam, while the Excel simulation creates all the ions at exactly the same point in space. This is significant because an ion starting slightly closer to the detector–by being created on the near side of the finite target volume–spends less time being accelerated by the extraction field than an ion created on the far side of the volume, even if both have the same initial momentum vector. This presents the problem that ions with the same momentum can have different times of flight depending on their initial position, which cannot be determined to any better precision than the target overlap size. Since the calculation of momentum depends on the time-of-flight, there must be a reliable relationship between the flight time and the initial momentum. This presents another condition for the spectrometer design and configuration.

In some cases, the differing initial position of ions can cause the ions created farther away to "catch up" to the ions created nearer to the detector because of the effect of the spectrometer's drift region. Since the farther away ions accelerate longer, they leave the acceleration region with greater velocity and, given enough room in the drift region, can overtake the nearer ions at some point during the flight. Ideally, that point would be when the ions hit the detector, because then the finite interaction volume is collapsed down to a point, so that ions created at different points in the volume would still arrive with the same flight time, provided their initial momentum in the TOF direction is the same. In some cases, a longer spectrometer is preferable, especially if the kinetic energy of the fragments is very small, but if the detector is placed far past the focus point mentioned above, the ions may be *overfocused* and ions starting initially farther from the detector would arrive earlier. This effect may be enough to make viewing the angular structure of the dissociation unfeasable. Figure 3.9 shows a flight of ions with the same initial momenta but slightly different starting positions. The placement of the detector near the focusing node of the ions offsets the effect of the finite interaction volume.

Ultimately, the purpose of the simulation is to provide a context in which to view the measured data. In the directions parallel to the detector plane, (ideally) no force is exerted on the ions, so their initial momentum is simply their final momentum, which is simple to calculate. In the TOF direction, however, there is a close-but-not-quite-linear relationship between the flight time and the initial momentum. Figure 3.10 shows this relationship from the above simulation. To generate a function that will translate the ion TOF to its initial momentum in the TOF direction, the results of the simulation are fit with a third-order polynomial, which will allow the calculation of the momentum for any time-of-flight in the simulated range. A simple Mathematica notebook is used to perform the fit and generate the formula in C code format for use in the analysis code. Mathematica also implements an offset to the time of flight data because the actual times of flight tend to differ from the simulation due to delays caused by electronics and the cables which carry the signals. This

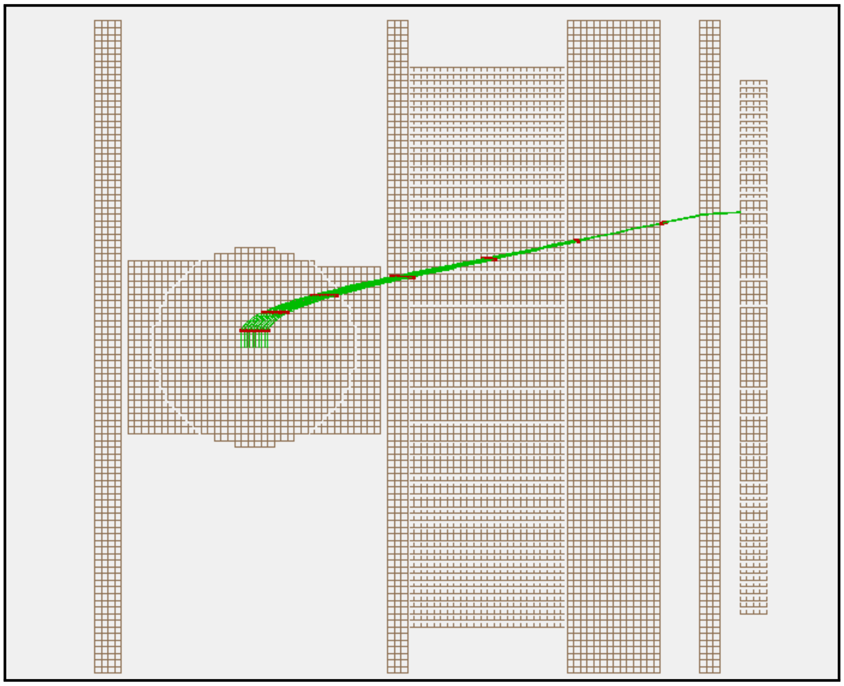

Figure 3.9: Ion flight simulation with ions created at varying points along a line but with identical momentum. The converging groups of red dots show that the finite interaction volume effectively collapses (in the T direction) on its way to the detector. The X and Y values for the position are unaffected by this focusing. Also the interaction volume is smaller in the X direction (because it is defined by the jet size, rather than the electron beam) so slicing the momentum is typically done in the XT plane, where the resolution is best, rather than in the XY plane.

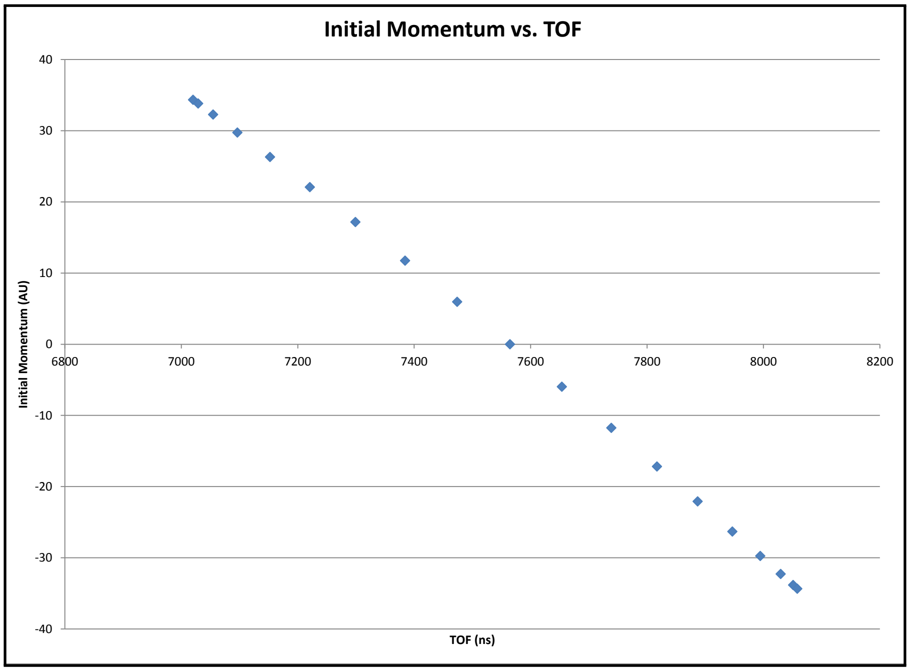

Figure 3.10: The initial momentum in the time-of-flight direction as a function of the time-of-flight. The points should decrease monotonically and be single-valued as a function of TOF in order for the momentum in that direction to be calculated from the flight time.

delay is the same for all ions and is selected to make the simulation results consistent with the measurement; it is a small fraction (typically 0.5%) of the total flight time.

The simulation process is sometimes iterative. The ion kinetic energy is often one of the measured quantities in the experiment, but the simulation itself requires the kinetic energy in order to fly the ions. This means that an initial guess must be made about the ion energy, then comparison with the measurement allows for calibration and resimulation. Fortunately, the ion kinetic energy is irrelevant with regard to the *center* of the TOF distribution, because ions in the center of the distribution have no momentum in the TOF direction, and their TOF is not affected by the energy released in the reaction. This means that ion formation can still be identified by peaks in the TOF spectrum, as well as information about the relative ion yield at a given energy, but the width of the distribution *is* affected by the ion energy. The energy, even if not known in the beginning, can be obtained because the momentum parallel to the detector can be easily calculated and compared to the TOF momentum until they form a round momentum sphere. This point will become more clear in light of the data on methane.

4 — Results and Discussion

> "I do not see it. It is interesting that people try to find meaningful patterns in things that are essentially random. I have noticed that the images they perceive sometimes suggest what they are thinking about at that particular moment. Besides, it is clearly a bunny rabbit."
>
> *–Lt. Commander Data*

Although the apparatus was designed to perform experiments on dissociative attachment, testing was initially done on positive ion production from dissociative ionization of molecular species including helium, oxygen, acetylene, and methane. In order to be assured that the spectrometer yields predictable ion signals corresponding to the correct charge states of ion fragments, testing was performed on varying gas species to produce positive ions via dissociative ionization from higher energy electrons.

4.1 Dissociative Ionization of CH_4

Dissociative ionization was observed for methane with 500 eV incident electrons. The total ionization cross section has been seen to have a peak at around 100 eV and an onset around 20 eV.[80–82] At an energy of 500 eV, far above the ionization threshold, no visible anisotropy should be present in the momentum images.[83] Yet, as a test of the new apparatus, CH_4 serves as a good test case for the measurement of the kinetic energy release of ion fragments, the

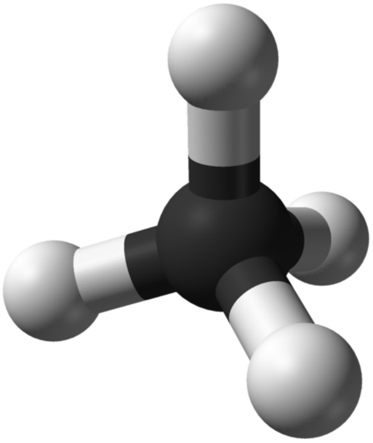

Figure 4.1: Ball-and-stick model of the methane molecule, showing the bond arrangement and symmetry.

planar imaging of the momentum distribution, and the coincidence measurement of multiple positive ions.

Figure 4.1 shows a basic model of the methane molecule, which has tetrahedral symmetry and belongs to the T_d point group. Electron impact ionization of methane is generally characterized by the following equation:

$$e^- + CH_4 \to CH_4^+ + 2e^- \tag{4.1}$$

The field produced by the incident electron in the vicinity of the molecule causes a bound electron in the molecule to be liberated, leaving a positively charged $\mathrm{CH_4^+}$ ion. The typical interaction time is very short ($\sim 10^{-16}$ s), so that the interaction causes a vertical Franck-Condon transition to the ionic state. Often, the ionic state is dissociative, and the molecule separates into fragments along one of several fragmentation channels. Two main channels are observed here:

$$CH_4^+ \to CH_3^+ + H^+ + e^- \qquad CH_4^+ \to CH_2^+ + H_2^+ + e^- \tag{4.2}$$

Of course, in experimental conditions, all the possible channels are realized with varying ion yields, and identification of the coincident fragments is done by using a correlation diagram. When the detector receives two hits in a single acquisition cycle, the problem is to determine whether both ions are from the same interaction with a common incident electron or whether two unrelated ions happened to reach the detector near the same time with no actual causal link. Figure 4.2 shows the time-of-flight correlation of first and second hits from electron impact on methane. By plotting the time-of-flight of the second hit versus that of the first hit, a correlation between the two can be observed, and distinctive patterns emerge for ion pairs which are actually coincident. In Fig. 4.2 (bottom), the downward-sloping diagonal lines indicate ion pairs which conserve momentum and have a finite kinetic energy release.[1] The length of the line indicates the amount of kinetic energy. The cluster of bands around (1000, 2750) are coincident fragment pairs from methane, and the islands around (1000, 1000) are coincident H^+ and H^+ ions. Since the TOF of the ions is proportional to the square root of the mass-to-charge ratio, the plot of one TOF versus the other forms a grid which can be used to identify pairs of hits corresponding to specific reactions. Points landing very near the diagonal represent like masses which reach the detector at around the same time, while points away from the diagonal belong to asymmetric mass pairs. Horizontal and vertical streaks of points, as well as blobs of points with no structure, are pairs of hits which are generally uncorrelated and don't conserve momentum.

Figure 4.3 shows the region of the time-of-flight correlation plot that is related to the CH_4 breakup channels. In order to isolate a particular channel, a gate (condition) is set on the sum and difference of the two ion flight times such that only events in a particular stripe are admitted. However, some level of background noise from non-coincident hits obscures the data, as is particularly evident in the CH_3^+ + H^+ channel. To filter out this noise, the restriction is placed on the particle pairs that they satisfy momentum conservation, since ions resulting from dissociation of one molecule would conserve momentum, while random ions

---

[1] No events exist below the diagonal because, by definition, the second hit must come after the first hit, so that the TOF for recoil 2 is always greater than the TOF for recoil 1.

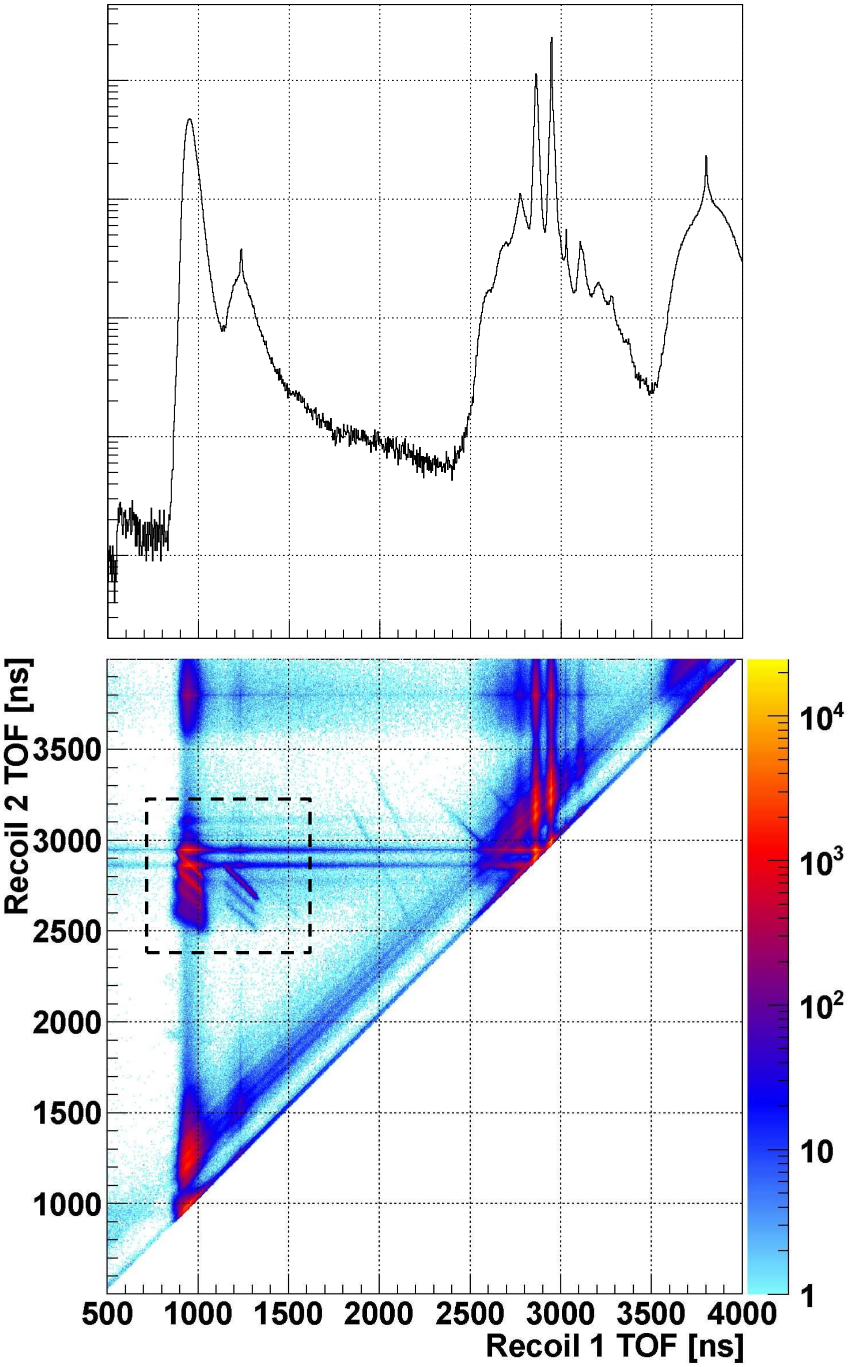

Figure 4.2: (bottom) Time-of-flight correlation plot of first and second hit ions from methane. Diagonal lines indicate correlated double-hits, while horizontal and vertical bands indicate random second hits. The dashed box in the figure contains ion pairs which have masses corresponding to fragments of methane. Each island of points in the group represents a particular breakup channel. (top) One-dimensional time-of-flight histogram including all hits. The top graph is a projection of the bottom data onto the horizontal axis (same x scale and arbitrary y axis scale).

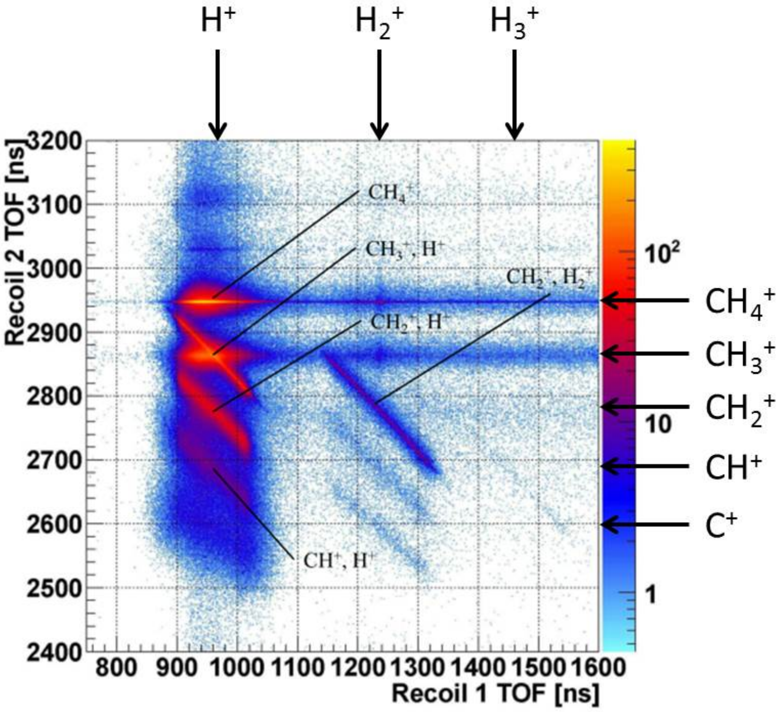

Figure 4.3: Time-of-flight correlation plot for flight times in the range of methane (zoomed in from Fig. 4.2) with the dominant channels labeled. Channels are separated by one H^+ of mass vertically and horizontally. The first column of lines corresponds to channels including an H^+, with the second column including an H_2^+. A faint diagonal stripe on the right indicates the presence of a $CH^+ + H_3^+$ channel. The horizontal bands are the result of single hits from CH_4^+ and CH_3^+ that appear with an uncorrelated, random second hit.

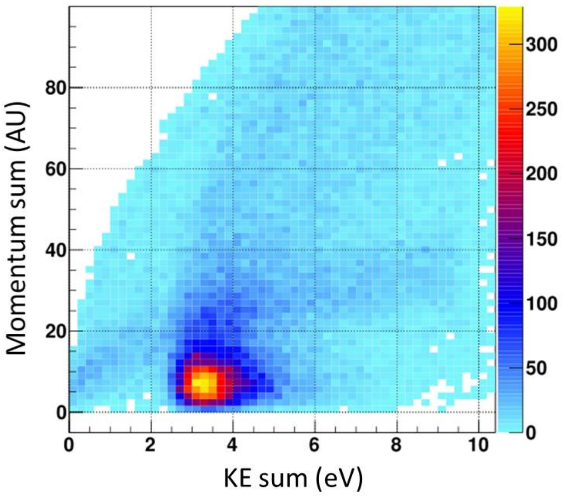

Figure 4.4: Momentum vs. kinetic energy for CH_3^+ + H^+. The momentum is the vector sum $|\vec{p}| = \sqrt{(p_{x1}+p_{x2})^2+(p_{y1}+p_{y2})^2+(p_{t1}+p_{t2})^2}$, and the energy sum is $\frac{|p|^2}{2m}$. The island of points near the bottom have a total momentum of nearly zero and a finite kinetic energy, indicating that they are the "good" events.

which hit the detector accidentally near each other in time would not conserve momentum. Figure 4.4 shows the total kinetic energy versus the total momentum of the two particles in the CH_3^+ + H^+ channel. An island exists at the bottom because actual correlated double hits will conserve momentum and will have a finite kinetic energy sum (due to the bond dissociation). Restricting the data to the events in this island keeps random double hits out of the final data[2].

From Fig. 4.4, it appears that the total kinetic energy will be between 3 and 4 eV for that channel. Figure 4.5 shows the yield as a function of kinetic energy for the two channels along with data from a similar experiment performed at Auburn with 1 MeV C^{5+} ions instead of electrons. The present results with electrons show a very similar energy distribution with peaks slightly lower than for the positive ion experiment, but within the experimental uncertainty of both data sets (as given by the half-width of the distributions).

---

[2] Still, occasionally two random particles will hit near the same time and also have momentum values which add to zero and give a finite kinetic energy sum out of pure chance. These events would be indistinguishable from real coincident hits, but they are obviously very unlikely.

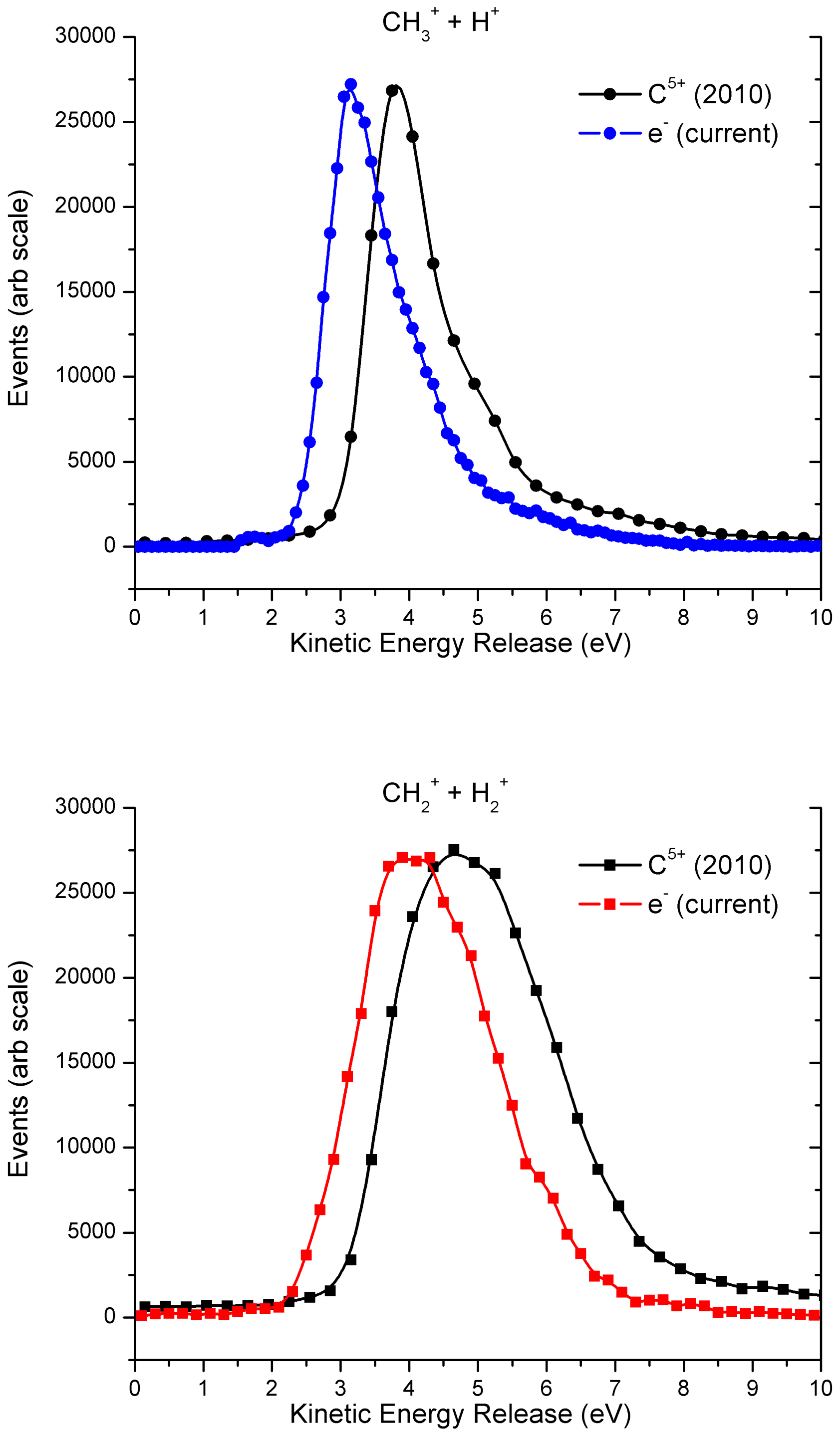

Figure 4.5: Yield as a function of total kinetic energy for the $CH_3^+ + H^+$ reaction (top) and the $CH_2^+ + H_2^+$ reaction (bottom). The blue and red lines are the present data, and the black line is data from a previous experiment which used positive ion projectiles at 1 MeV to charge exchange with a neutral target, leaving the same cation as in the present experiment (unpublished).

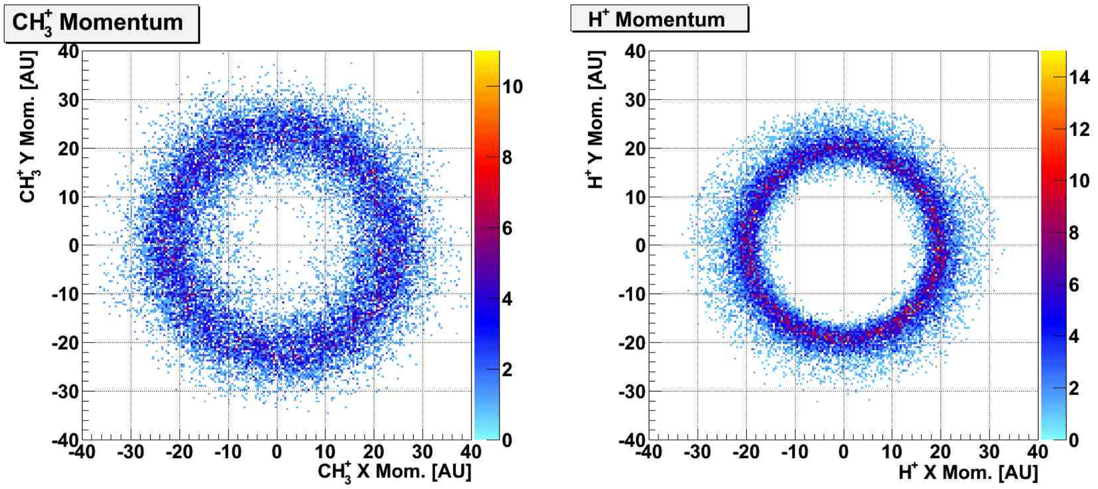

Figure 4.6: Momentum distributions of CH$_3^+$ (left) and H$^+$ (right) resulting from dissociative ionization. As expected, the distribution has no apparent angular anisotropy.

The momentum distributions of the two dissociation channels show an expected result. Figures 4.6 and 4.7 reveal no anisotropy in the momentum distributions in the plane of the detector. The X and Y axes are defined by the detector coordinates. The electron momentum in these figures points to the right, and by the symmetry of the experiment, it is certainly expected that the distributions have symmetry across the X axis. In order to be confident that the momentum calculations are valid, the images should be round, and coincident fragments should have roughly the same momentum.

In the dissociative ionization of methane, requiring that the pairs of ions conserve momentum allows the data to be separated from the background noise, while the single-ion collection used in the forthcoming dissociative attachment experiments does not contain enough information for such filtering, as the neutral species is uncollected. However, the analysis of the single-particle detection is simpler and, as we shall see, the resulting angular distributions in momentum can be compared to theoretical calculations to gain insight into the dissociation dynamics and the molecular states involved.

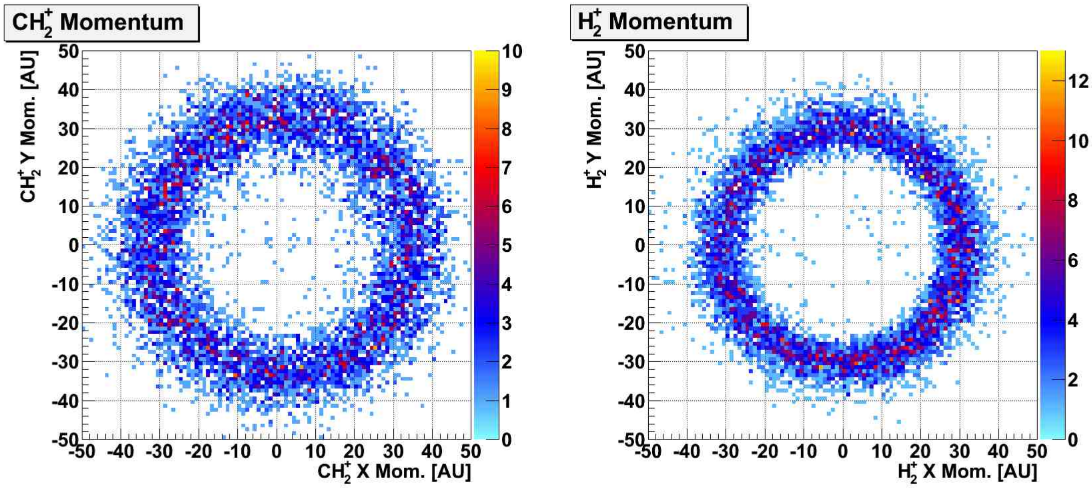

Figure 4.7: Momentum distributions of CH_2^+ (left) and H_2^+ (right) resulting from dissociative ionization. The distribution has no apparent angular anisotropy.

4.2 Dissociative Attachment to O_2

To measure anion production from dissociative attachment and observe angular anisotropies in the fragment anions, diatomic oxygen serves as an interesting case. As a homonuclear diatomic molecule, the one-dimensional structure and high symmetry of the molecule allows previously developed methods to be used for the prediction of angular dependences and the molecular states that cause them. O_2 has a dumbell-shaped, cylindrically symmetric structure (under rotation through any angle about the internuclear axis) with an inversion center, belonging to the $D_{\infty h}$ point group. (The term symbols for the ground state configuration are given in Chapter 1.) The general form of the dissociative attachment reaction to O_2 is:

$$O_2 + e^- \rightarrow (O_2^-)^* \rightarrow O + O^- \tag{4.3}$$

The data presented here focuses mainly on the appearance of a ${}^4\Sigma_u^-$ state previously presumed to exist at the higher energy end of a broad dissociative attachment peak in the cross section. Existing work with electrons under 15 eV indicates that the four resonances ${}^2\Pi_g$, ${}^2\Pi_u$, ${}^4\Sigma_u^-$, and ${}^2\Sigma_u^-$ are responsible for excitations in O_2.[85] For DEA, the 6.5 eV resonance

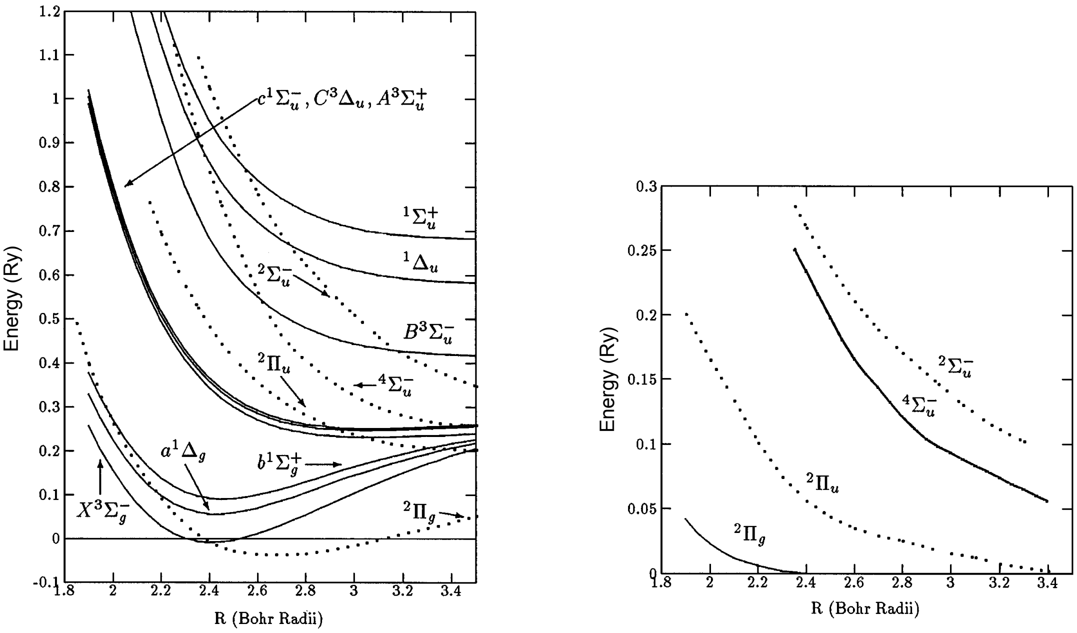

(a) (b)

Figure 4.8: (a) Calculated potential energy curves (in Ry) of the neutral states (solid lines) and resonances (dotted lines) for diatomic oxygen, (b) Calculated widths (in Ry) of the resonances.[84] From the ground state $X^3\Sigma_g^-$, a vertical transition of ~0.5 Ry (6.8 eV) to the $^2\Pi_u$ resonance is available, and starting at ~9 eV above the ground state, a transition to $^4\Sigma_u^-$ is also possible.

has been measured to result from the $^2\Pi_u$ state via observations of the angular distribution.[86] While R-matrix calculations from Noble et al. indicated that the autodetachment lifetime would preclude a contribution to the O^- yield from the $^4\Sigma_u^-$ state,[84] recent measurements by Prabhudesai et al.[85] seem to demonstrate a contribution from that state manifested as increased attachment probability in the forward and backward directions with respect to the incoming electron momentum. The earlier experiments were unable to measure angular distribution data in the extreme angles, and the selection rules codified by Dunn which determine symmetry requirements for resonant states would indicate such a contribution for the $^4\Sigma_u^-$ state but not the $^2\Pi_u$.[83]

Figure 4.8 shows the calculated potential energy curves for the target states and resonances of O_2.[84] The energy range observed in this experiment is from 5 eV to 9 eV, and in this range above the ground state shown in Fig. 4.8 is a $^2\Pi_u$ state which is accessible via a vertical transition from the ground state $X^3\Sigma_g^-$. Since this state has Π symmetry, the angular dependence of the products may be expected to be proportional to $\sin^2(2\theta)$, if they can be attributed entirely to this state.[83,86,87] A higher-lying $^4\Sigma_u^-$ state is also accessible through a vertical transition starting at around 8 eV above the ground state. This state has been suspected to contribute to the ion yield along the axis of the incoming electron momentum, increasing the ion production at 0° and 180°. This would be explained by the $\cos^2(\theta)$ angular dependence of the $^4\Sigma_u^-$ state.[87]

Figure 4.9 includes the momentum-space plots for O^- production at four energies. The lower energies (5 eV and 6.5 eV) show a clearly anisotropic distribution with minima in the forward and backward directions with respect to the incoming electron momentum (pointing up in all figures). A noticable asymmetry also exists in the forward/backward direction, showing a preference for ejection of O^- fragments in the backward direction. This effect had been noticed previously,[86] but was assumed to be the result an instrumental effect. Its appearance here may indicate otherwise and could be the result of an interaction between

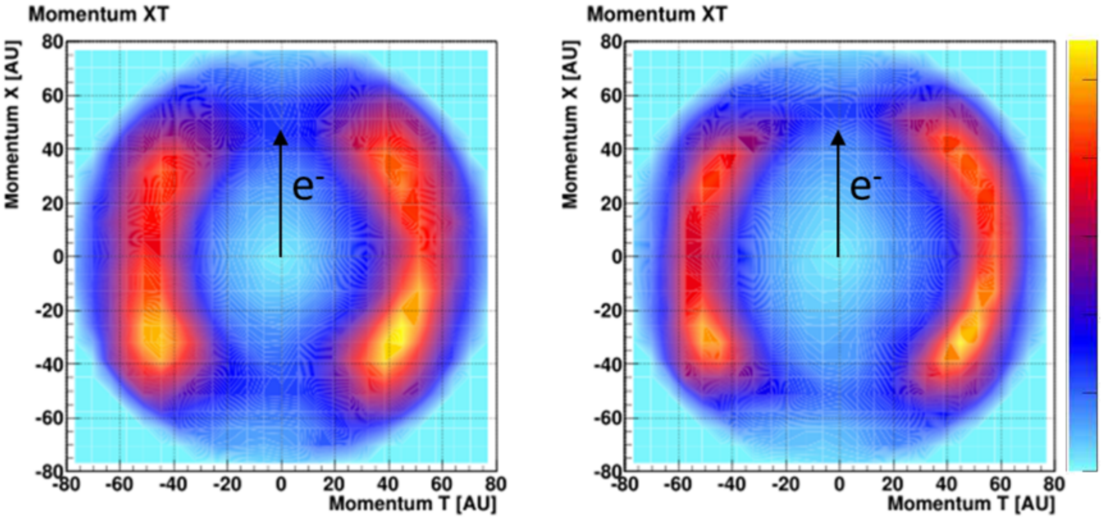

(a) 5 eV (b) 6.5 eV

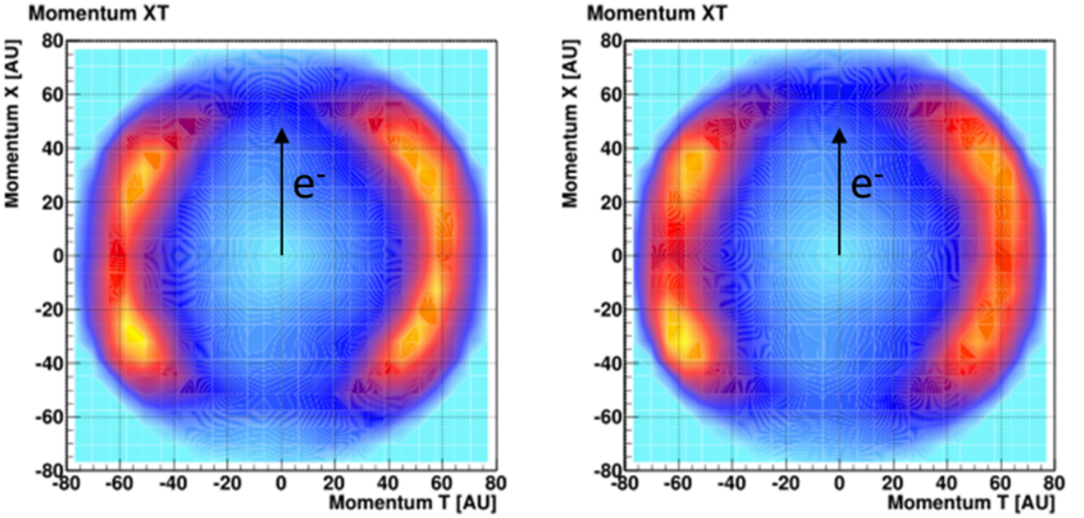

(c) 8 eV (d) 9 eV

Figure 4.9: Momentum distributions for O^- production from dissociative attachment to O_2 at four incident electron energies: (a) 5 eV, (b) 6.5 eV, (c) 8 eV, (d) 9 eV. The incident electron points up in all figures. All the distributions show minima in the forward and backward directions (defined by the incoming electron momentum), but the distribution changes at the higher energies to form a four-lobed structure. The distributions also spread out radially with higher energy, owing to the additional kinetic energy of the incoming electron.

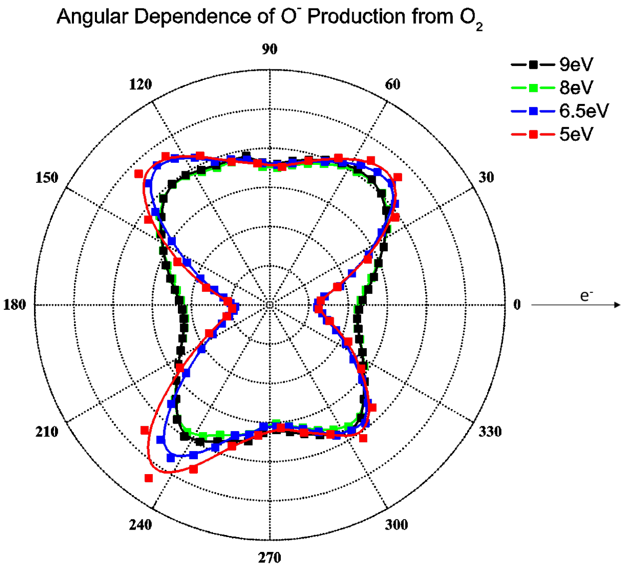

Figure 4.10: Polar distribution of O$^-$ ions from dissociative attachment to O$_2$ at four energies. 0° represents the direction of the incident electron (right). The two higher energies (green and black) show increased ion yield at 0° and 180° compared to that at 90°. This indicates attachment via the $^4\Sigma_u^-$ anion state. The curves are all normalized to 90°.

two different states. At the two higher energies, the distribution resembles a four-lobed petal structure with peaks also in the forward direction.

As mentioned above, production of O$^-$ from the $^4\Sigma_u^-$ state should manifest as an increased ion yield in the forward and backward directions. This subtle effect is not visible in the Fig. 4.9 momentum plots, but a polar plot of the angular distribution makes the effect more apparent. Figure 4.10 shows the angular distribution for the four energies. The polar data is generated by integrating the momentum plots from Fig. 4.9 radially in the energy range of the majority of the O$^-$ signal. The angular data, showing increased anion production in the forward and backward directions with respect to the incoming electron, indicate the attachment and dissociation via the $^4\Sigma_u^-$ state at higher energies.

4.3 CO_2 at the 8 eV Feshbach Resonance[88]

Dissociative electron attachment (DEA) is a dominant dissociation mechanism leading to the production of stable anions from electrons at energies below 10 eV. Extant literature on this mechanism in CO_2 provides information on cross sections and ion energy as well as angle specific dissociation utilizing electron beam monochromators and mass analyzers,[89–96] while newer experimental techniques have allowed three-dimensional imaging of the dissociation dynamics.[66,67,97] Dissociative attachment resonances for this system are well known, with a shape resonance appearing at 4 eV and a Feshbach resonance near 8 eV. The resonance at 8 eV was earlier attributed to a $^2\Sigma_g^+$ state,[95,98] but later researchers determined that a Feshbach resonance of $^2\Pi_g$ character is the likely resonant state.[93,96,99] Further, Slaughter et al. determined that a conical intersection exists between the $^2\Pi_g$ state of the transient anion at 8 eV and the $^2\Pi_u$ state at 4 eV,[100] so that the results for the 8 eV resonance are important to understanding the lower energy resonance as well.

Angle- and energy-resolved imaging on DEA to carbon dioxide, particularly at the 8 eV Feshbach resonance, have revealed an anisotropic angular distribution for the resulting O^- anion with a minimum in the direction of the incoming electron momentum. Additionally, a near-zero energy contribution is seen in the momentum distribution when confined to a plane containing the incoming electron's momentum vector.[95,96,100,101] Our work contends that the contribution from this near-zero energy contribution may be exaggerated by the treatment of the data. Also, recent attempts to explain the mechanism of dissocative attachment via the Renner-Teller effect by fitting the measured angular distributions with spherical harmonics are belied by observations of a clear non-axial recoil effect observed in the O^- angular fragment distribution.

The momentum-space plots in Fig. 4.11 show an anisotropic distribution with a minimum in the direction of the incoming electron momentum and small peaks appearing at 130°. The electron momentum is up in Fig. 4.11. The X direction defines the electron momentum

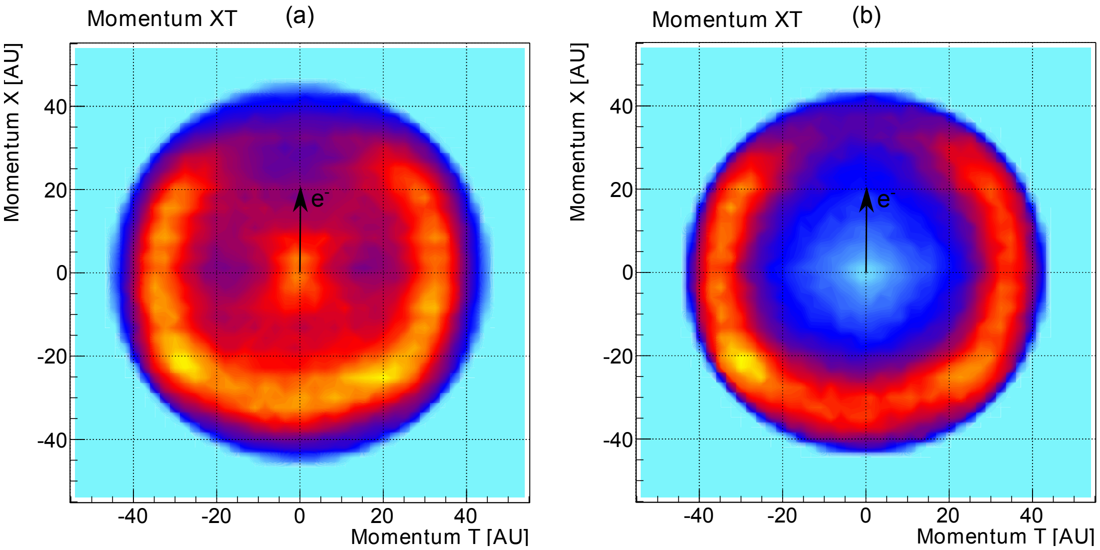

Figure 4.11: (a) Density plot of the unweighted momentum. (b) Density plot of the momentum weighted for equal solid angle. The X direction is along the electron momentum and the T direction is normal to the detector plane. The electron momentum direction is up. The low energy distribution in the center of (a) disappears when the distribution is weighted for solid angle. The distribution in (b) includes the same fraction of the momentum sphere regardless of energy.

vector and the T direction points toward the detector, so that the jet direction is out of the image plane. Figure 4.11(a) shows the momentum sphere sliced through the center by constraining the data to within ±5.4 AU momentum in the Y direction, while Fig. 4.11(b) is the same data weighted to account for the changing solid angle by constraining the elevation angle of the momentum to within ±5°. This angle is chosen to coincide with the expected momentum resolution of the experiment. As the radius increases, the angle of acceptance is held constant so that fragments of differing energy are treated equally.

The center, low-energy feature is clearly visible in the unweighted slice (Fig. 4.11(a)) but not in the weighted data (Fig. 4.11(b)). Since the zero-energy peak would appear as a small distribution of ions in the center of the momentum-space plot, a flat slice of the data would unduly weight the contribution of the lower energy ions against those of higher energy. Consider the extreme case of O^- produced in a point-like volume with a bimodal kinetic energy distribution, with one component having kinetic energy of nearly 0 eV and another component with equal yield having kinetic energy of exactly 0.6 eV. The 3D ion momentum image would appear as a dot surrounded by a thin spherical shell that we shall consider to be uniform over both azimuthal and polar angles for simplicity. A thin flat slice would include the entire contribution from the low kinetic energy component and only include a small fraction of ions having kinetic energy that is non-zero. If, instead of a thin flat slice, we confine the momentum to a solid angular range that is symmetrical in the detector plane the ion yields at different energies will be comparable.

Complementary velocity slice imaging techniques[101] collect ion data for a sufficiently narrow time-window in the center of the time-of-flight distribution to allow a 2D projection of the 3D ion distribution. The result is typically comparable to the flat slice of Fig. 4.11(a) that exaggerates the yield of ions having low kinetic energy. This could be corrected by weighting the results during offline analysis. Alternatively, Slaughter et. al[100] projected the full 3D momentum image onto a 2D plane to show the planar momentum distribution, which also exaggerates the small momentum contribution. The data from Slaughter et al., when weighted in the same manner as the present data, are consistent with the results in Fig. 4.11(b).

Figure 4.12 shows the ion yield as a function of kinetic energy from the referenced sources as well as the present work. The kinetic energy curve is obtained by integrating the ejection angle of the O^- and plotting the yield as a function of kinetic energy

$$KE = \frac{p^2}{2m} \tag{4.4}$$

where p is the absolute momentum and m is the mass of O^-.

The present unweighted data show qualitative agreement with each set of published data, except the original, uncorrected data of Dressler and Allan. The present weighted data are in reasonable agreement with the data of Dressler and Allan, however we found poor agreement between the present data and their suggested correction (not shown) for the

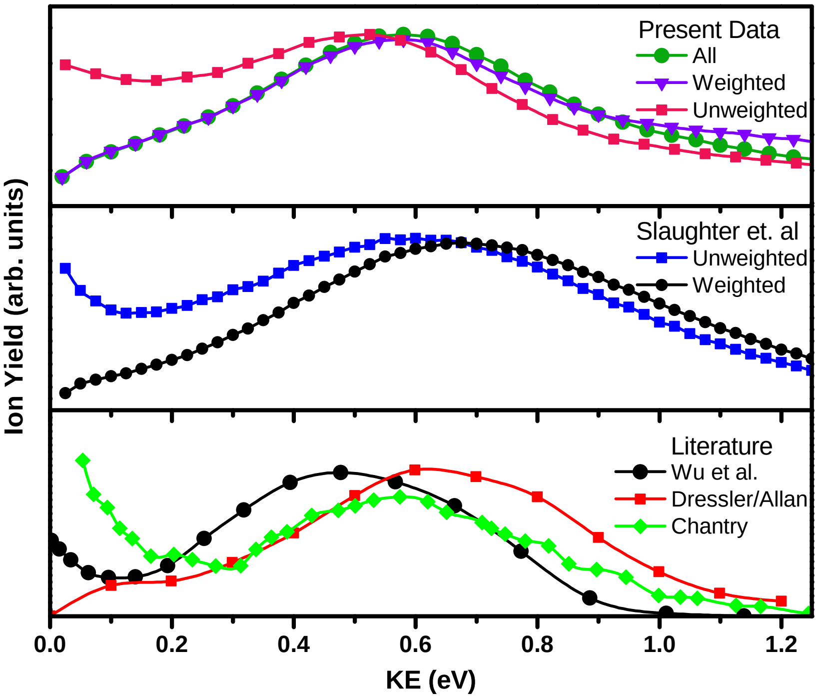

Figure 4.12: Kinetic energy distributions for oxygen anions from literature and present data. Top panel: Present data at 8.2 eV. The weighted data shows a diminished contribution from low energy anions compared to the unweighted data. Middle panel: Data from Slaughter et al.[100] weighted (black circles) and unweighted (blue squares) at 8.7 eV. Bottom panel: Data from Wu et al.[101] (black circles), Dressler/Allan[96] (red squares), and Chantry (green diamonds).

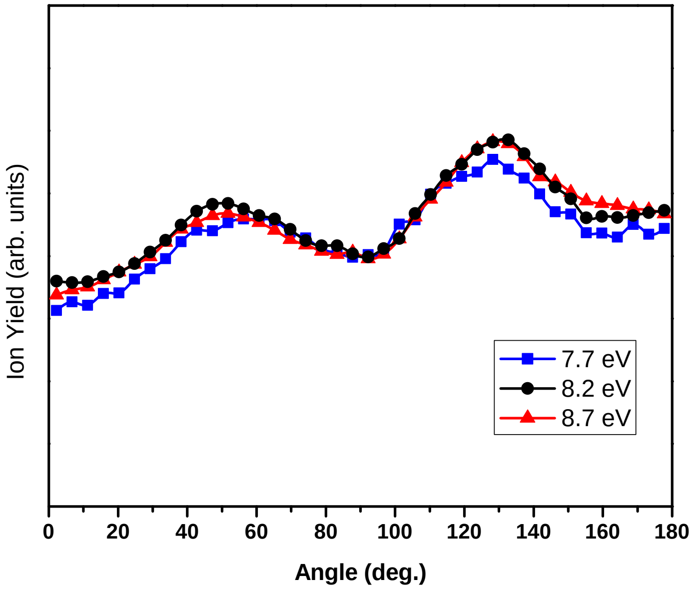

Figure 4.13: Angular distribution of O$^-$ ions for three electron impact energies, 7.7 eV (blue squares), 8.2 eV (black circles), and 8.7 eV (red triangles). The distributions show no significant dependence on energy in the observed range.

instrument used in that experiment.[96] Furthermore, if all the data in the entire momentum sphere are included so that the solid angle is certainly the same regardless of kinetic energy, the result is similar to the weighted data (see Fig. 4.12), showing that weighting provides an equivalent comparison to taking the full sphere. Earlier results by Dressler and Allan with 8.3 eV electrons also revealed the low-energy peak, but a correction the authors made to account for a systematic error in the spectrometer resulted in suppression of the peak. Wu et al. used an unweighted flat slice from a phosphor screen image, while Slaughter et al. used a coordinate transformation to plot the momentum's transverse and longitudinal components (with respect to the electron momentum vector).[97] Their results match the present data when a similar, weighted scheme is used.

Figure 4.13 shows the angular distribution of O$^-$ at 8.2 ±0.5 eV electron energy as well as 7.7 eV and 8.7 eV. The angular distributions in Fig. 4.13 indicate that the distributions are not visibly affected by the varying impact energy across the resonance. This is contrary to

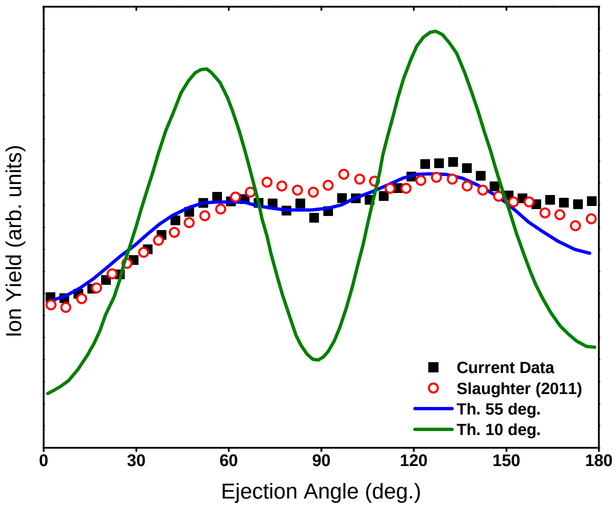

Figure 4.14: Angular distribution of O^- from the present experiment for 8.2 eV electrons (black squares). Measured data (red circles) and calculations convolved with a Gaussian of full width at half maximum of 10° (green line) and 55° (blue line) from Slaughter et al.[100] The data match the calculation convolved by 55° more closely than 10°, implying a non-axial recoil effect.

results presented by Wu et al. in which the angular distribution varied significantly with the electron energy. The experimental results by Slaughter et al.[100] are also in good agreement with the present results when analyzed with the appropriate weighting as shown.

The measured angular distribution of O^- anions from dissociative attachment to CO_2 are shown in Fig. 4.14 with theoretical calculations and measurement from Slaughter et al. The two theory curves show the angular distribution assuming root mean square (RMS) values of the nuclei positions under asymmetric stretch and bending modes which were then convolved with Gaussian distributions of 10° and 55° width to simulate the expected angular resolution of the experiment and to match the observed data, respectively. As with the experimental data of Slaughter et al.,[100] the current measurement clearly shows better agreement with the 55° convolved theory curve, implying a strong non-axial recoil effect due to the bend and stretch contributions to the dissociation dynamics. Wu et al.[101] utilized the theory formulated by O'Malley and Taylor[87] to express the O^- angular dependence as a function of spherical harmonics corresponding to a splitting of the rovibrational state upon excitation of the vibrational bending mode v_2. Under conditions where the axial recoil approximation is valid,[87] a description of the electron attachment process can be accurately determined with such a treatment. Slaughter et al.[100] employed an *ab initio* theoretical approach to detemine the entrance amplitude and predict the ion angular distribution for the axial recoil case, which was found to differ remarkably from their experimental data, suggesting a departure from axial recoil conditions.

The present data are in good agreement with the data of Adaniya et al.[97] and further support the conclusion that dynamics beyond simple axial recoil are responsible for the observed fragment angular distributions. Interestingly, the data in both experiments deviates noticeably from the theory, convolved with a Gaussian of full width at half maximum of 55°, near the backward scattering angle, although the reason for this has yet to be determined.

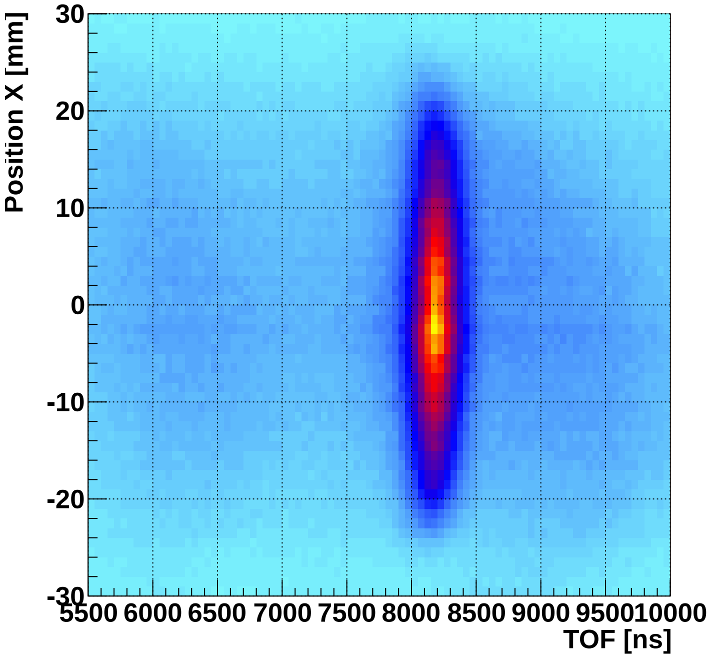

Figure 4.15: Position (in X) on the detector vs. Time of Flight for O^- ions from attachment to CO_2 at 4.4 eV. The electron beam points up (+X direction). The distribution is narrow in the TOF direction and distinct from the energetic dissociation seen in attachment to O_2 and CO_2 (at 8 eV).

4.4 CO_2 at the 4 eV Shape Resonance

A temporary negative ion (TNI) formed from attachment to CO_2 appears at around 3.8 eV electron energies, with a peak in its cross section at 4.4 eV. This O^- formation, at the lower incident electron energies, has been long attributed to a $^2\Pi_u$ shape resonance.[102–105] Because, in the linear CO_2 molecule, the vacant *p*-orbital in the O atom can be aligned parallel or perpendicular to the CO bond axis, states of $^2\Pi$ and $^2\Sigma$ symmetry are possible for the TNI.

Figure 4.15 shows the position/TOF correlation plot for the O^-. The distribution is confined in the TOF direction and appears to have very little momentum in that direction. Indeed, in Fig. 4.16, the momentum-space plot (subject to a weighted slice as explained in Section 4.3) shows an almost purely forward and backward contribution to the momentum distribution, with no ion yield (above background level) for angles deviating significantly from the incident electron momentum direction (pointing up in the figure). There is also a

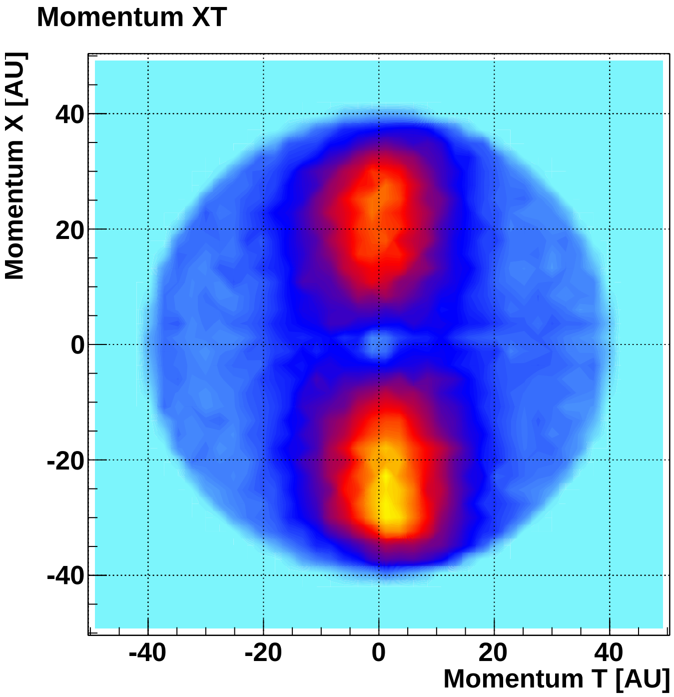

Figure 4.16: Momentum in the XT-plane for O^- ions from CO_2 at 4.4 eV. The distribution of O^- ions is almost purely in the forward-backward direction with respect to the incoming electron momentum (pointing up). Also, a clear asymmetry is shown with preference for O^- ejection in the backward (180°) angle.

fairly prominent asymmetry favoring anion ejection in the backward angle (180°), which has been also observed in a parallel experiment at Lawrence Berkeley National Laboratory[106] (LBNL).

The polar plot in Fig. 4.17(a) shows the same data integrated radially to reveal the attachment occurence as a function of angle (with the constant background level subtracted). The ratio of forward to backward yields in this plot implies roughly a 30% asymmetry effect. Figure 4.17(b) shows a three-dimensional visualization of the same data, using the full momentum data in all directions. The surface height (and color) from the center of the distribution represents the anion production at the corresponding angles (elevation and azimuth). The isotropic distribution in the YT-plane is to be expected from the symmetry of the experiment.

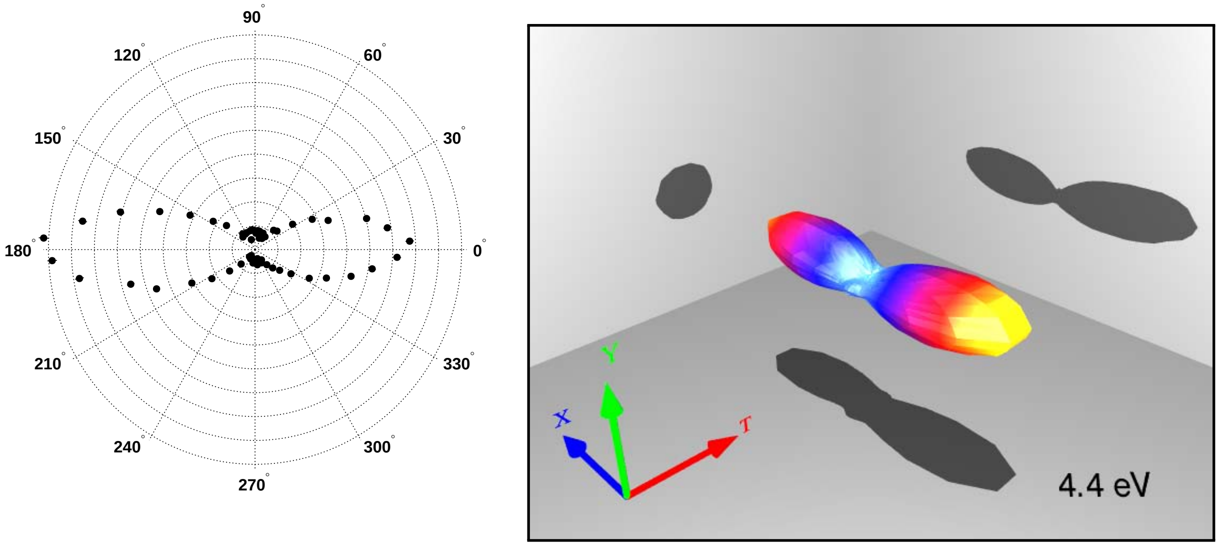

Figure 4.17: (left) Polar plot of the O^- ejection yield as a function of angle. A constant background, visible in Fig. 4.16, is subtracted. The incident electron direction is to the right (0°). (right) A 3D visualization of the attachment probability. The radial distance of the surface from the center of the distribution (as well as the color) represents the ion yield at the corresponding angle. The incident electron points in the +X direction. By symmetry, the distribution in the YT-plane is isotropic.

In Fig. 4.18, the calculated entrance amplitude is shown to differ significantly from the observed angular distribution of the anions. The entrance amplitude, $V_{\vec{a}}(\vec{Q})$, is calculated via

$$V_{\vec{a}}(\vec{Q}) = \langle \psi_P(\vec{Q}) \, | H_{el} | \, \psi_Q(\vec{q}_{int}) \rangle \tag{4.5}$$

with the electronic Hamiltonian H_{el}, the resonant (TNI) state wave function ψ_Q, and the nonresonant wave function ψ_P which incorporates the incident electron wave function and the initial electronic state of the target.[107] $\vec{Q}$ denotes the nuclear degrees of freedom, including the molecular orientation, and $\vec{q}$ denotes the internal degrees of freedom. Integration over $\vec{q}$ leaves the entrance amplitude in terms of the angular orientation part of $\vec{Q}$. Thus, the entrance amplitude gives the angular dependence of the attachment cross section, which should match the angular ion yield data, given axial recoil conditions (the molecule does not bend or rotate appreciably during dissociation).

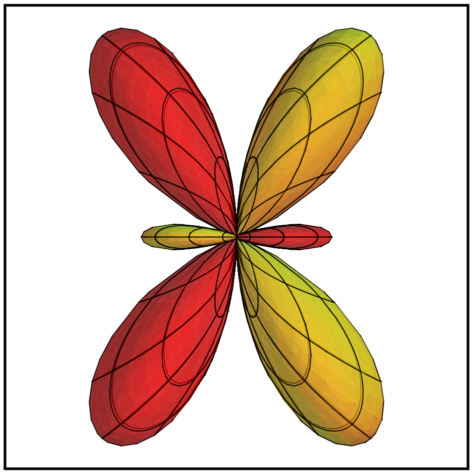

Figure 4.18: Electron attachment entrance amplitude for CO_2 at 4 eV in equlibrium geometry (no bond stretching or bending).[106] The C and O atoms would be aligned vertically in the center of the figure. The entrance amplitude is presumed to be proportional to the attachment probability, but the observed ion yield distribution is drastically different. This could be due to some geometric distortion or non-axial recoil after the attachment.

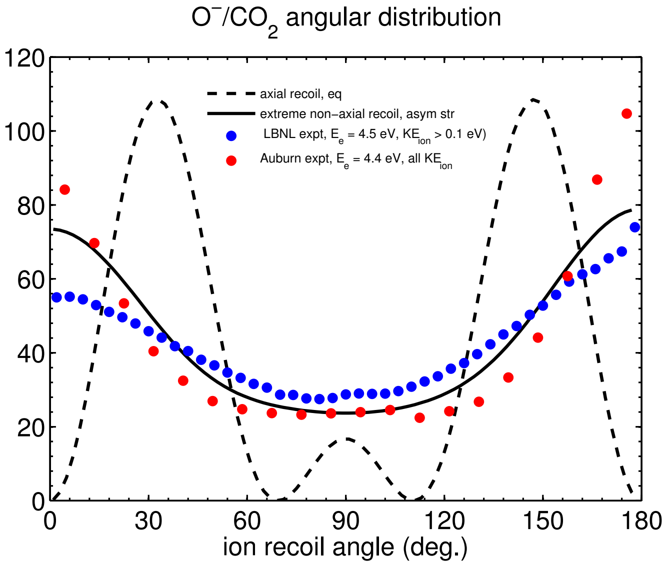

Figure 4.19: Angular distribution from the two experiments (AU and LBNL) compared to axial and non-axial recoil calculations.[106] The axial recoil curve is qualitatively different from both experiments, while the extreme non-axial recoil including an asymmetric stretch (stretching of one C-O bond with the other fixed) more closely approximates the data. The significant forward/backward asymmetry seen in both sets of data is thus far unexplained by the theory curve.

Figure 4.19 shows the data from the two experiments (Auburn University and LBNL) and the theory curve with axial recoil and non-axial recoil. The non-axial recoil curve involves an asymmetric bending mode which more closely resembles the angular distribution in the data. The Auburn angular data is more highly resolved, likely because the target molecules are colder than in the Berkeley experiment, which uses a diffuse target with higher initial temperature. The significant difference between the data and theory at equilibrium geometry indicates either that the dissociation involves a non-axial recoil effect, or that the long-accepted $^2\Pi_u$ state is a mischaracterization of the resonance.

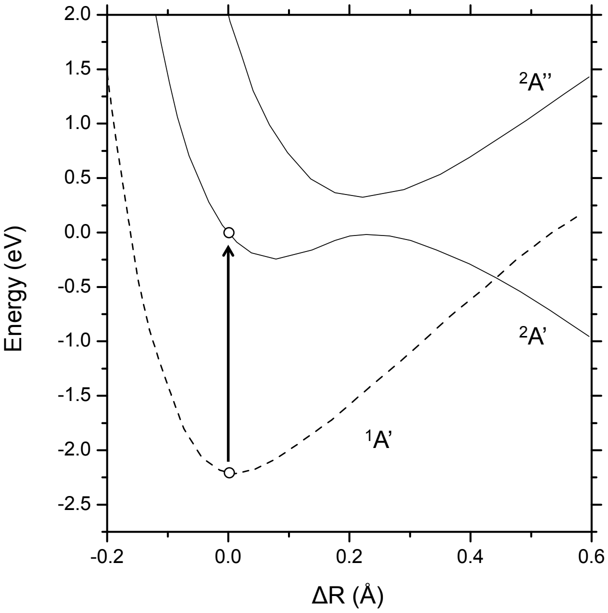

Figure 4.20: Potential energy curves for N_2O in linear geometry (bending angle $\gamma = 180°$) as a function of ΔR, the distance from equilibrium of the O atom to the center of the N-N bond. Attachment from the ground state ${}^1A'$ to the ${}^2A'$ state of N_2O^- leads to direct dissociation into N_2 + O^-. The ridge in the ${}^2A'$ curve at roughly 0.2 Å is presumed to lower in bent geometries.[108]

4.5 N_2O at the 2.3 eV Shape Resonance

Nitrous oxide is an asymmetric linear molecule belonging to the $C_{\infty v}$ point group. The $C_{\infty v}$ symmetry is broken upon bending, where specifically the ${}^2\Pi$ resonant state splits into ${}^2A'$ and ${}^2A''$ in the C_s point group. Dissociative attachment cross sections for N_2O show peaks at incident electron energies of 0.7 eV and 2.3 eV.[109,110] The cross section for the lower energy resonance has been shown to have a dramatic dependence on temperature, unlike the 2.3 eV resonance.[110,111] The 2.3 eV resonance, which is studied here, has a relatively large cross section ($\sim 10^{-17}$ cm^2, about 10 times that of the other DEA resonances shown in this work: O_2 near 7 eV and CO_2 at 4 and 8 eV).[109]

The angular dependence of the 2.3 eV resonance was measured by Tronc, and determined to have a combination of Σ and Π character from the partial wave scattering analysis.[112] However, these measurements were restricted in angular range (~30–130°) and did not include

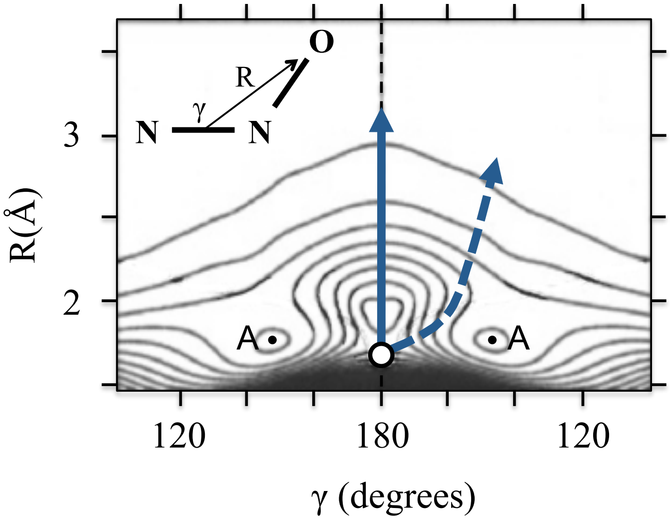

Figure 4.21: Potential energy plot of N_2O^- ($^2A'$) with the bent geometry as a function of the bending angle, γ, and the distance from the O atom to the center of mass of the N-N bond. The ridge at 180° lowers at the bent geometry, allowing for an around-the-ridge dissociation pathway (dotted line), as opposed to the direct dissociation in linear geometry (solid line).[108]

ions ejected near the forward and backward scattering angles. The full 4π measurements in this work can help to complete the picture of the angular dependence.

Figure 4.20 shows the potential energy curves for both N_2O and its anion N_2O^- in the linear geometry (no bending). The ground state, $^1A'$, is promoted vertically to the dissociative $^2A'$ curve of N_2O^-, which dissociates into the constituents N_2 and O^- through an avoided crossing with the higher-lying $^2A''$ state. The latter state dissociates into N_2^- and O, which would not be detected in this iteration of the present experiment. The hill in the $^2A'$ PE curve lowers in the bent geometry, as illustrated in Fig. 4.21. The $^2A'$ PE surface is plotted in Jacobi coordinates, using the distance R between the O and the center of mass of the N-N bond and the bending angle γ (180° in linear geometry). The lowered ridge away from the linear geometry implies that one dissociation pathway along this surface is for the anion to bend around the potential hill and dissociate at that non-linear geometry. The outgoing kinetic energy of the O^- is the same either way, but the partial wave scattering contributions to the angular distribution could help to elucidate the dominant pathway.

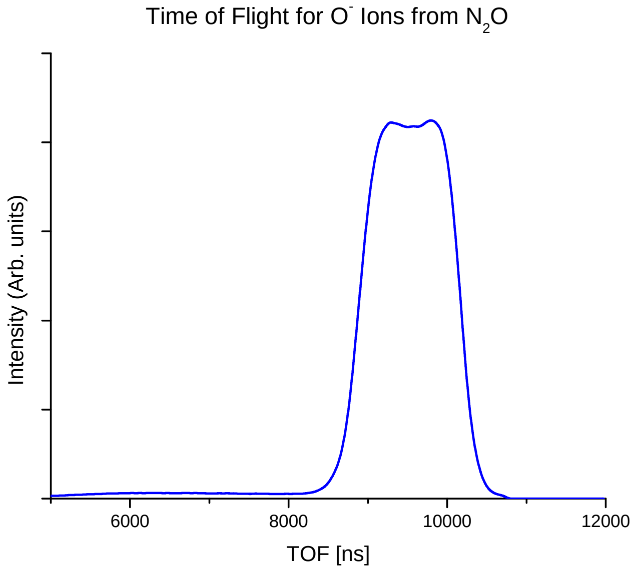

Figure 4.22: Time of flight spectrum for a N_2O gas target at an electron beam energy of 2.3 eV. The large cross section for attachment at this energy dominates the anion production.

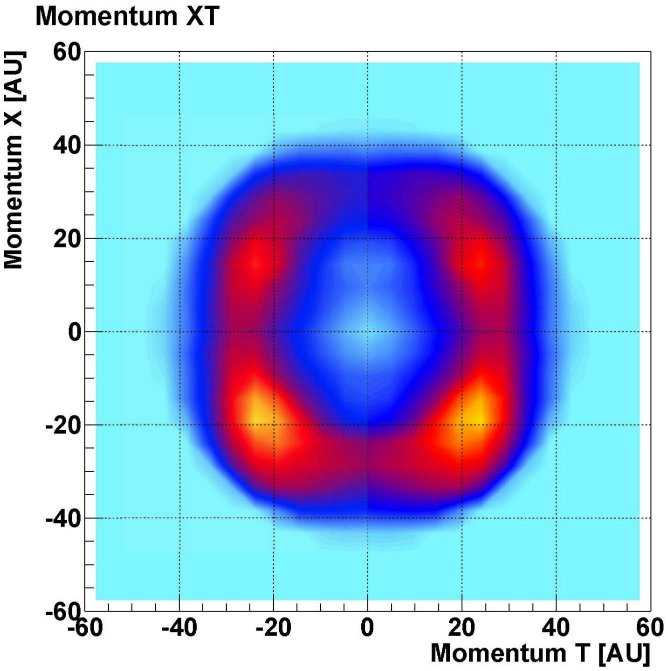

Figure 4.23: Momentum of O^- ions from dissociative attachment to N_2O. The incident electron direction (0°) is up. Peaks occur in the ion yield at 45° and 135°, with a preference for ion ejection in the backward direction and a clear minimum in the forward (0°) direction.

Figure 4.22 shows the time-of-flight spectrum for the present data. The spectrum is almost completely dominated by the O^- ions from attachment, since the electrons at this low energy tend not to interact with the background gas in the chamber to produce other negative ions.

In Fig. 4.23 is shown the momentum distribution of the measured O^- ions. The data show maxima in the ion yield at 45° and 135° with respect to the incoming electron momentum (up). There is also a preference for ion ejection in the backward angle. Figure 4.24 shows the corresponding kinetic energy distribution. The results are consistent with early measurements made by Chantry, while recent results from Xia have the peak slightly lower.[110, 113]

To interpret the angular distribution in momentum, the theoretical formulation of O'Malley and Taylor can be used by approximating the N_2O molecule as a diatomic molecule where only the distance between the oxygen atom and the center of mass of the N-N bond is considered, along with the bending angle. In this picture, the angular distribution of the dissociative attachment cross section can be written

$$\sigma_{DA}(\theta) \propto \sum_{\Lambda_r} \left| \sum_{L=|\mu|}^{\infty} C_{L\mu} e^{i\delta_{L\mu}} Y_{L\mu} \right|^2 \tag{4.6}$$

where Λ_r is the (axial) angular momentum quantum number of the final (resonant) state, L is the angular momentum of a single partial wave in the incoming electron's partial wave expansion, μ is the difference between the orbital angular momenta of the resonant and target states, $\Lambda_r - \Lambda_t$, and $\delta_{L\mu}$ and $C_{L\mu}$ are phase shifts and coefficients for each of the spherical harmonic terms[3]. Typically, for low energy electrons, it suffices to only use the first few partial wave contributions from the electron to describe the cross section.

---

[3] The dependence of cross section on the azimuthal angle ϕ is contained in $Y_{L\mu}$ as $e^{\mu\phi}$, but the expansion of the sum inside the squared modulus causes the terms to cancel, since the cross terms all have the same value of L.

The structure of the momentum distribution, with the basic four-lobed peak arrangement, can be mostly described using Σ and Π contributions from the above expansion. Explicitly, the terms are

$$\sigma_{DA}(\theta) \propto \left|a_0 Y_{00} + e^{i\delta_1} a_1 Y_{10} + e^{i\delta_2} a_2 Y_{20}\right|^2 + \left|b_0 Y_{11} + e^{i\delta_3} b_1 Y_{21} + e^{i\delta_4} b_2 Y_{31}\right|^2 \tag{4.7}$$

Then, by fitting the observed angular distribution with the partial waves, the predominant symmetric character of the resonant state can be determined from the fitting parameters.

An important effect to consider is the finite angular resolution of the experimental data. To compare the idealized partial wave scattering contributions to the measured angular distribution, the calculated distributions are convolved with a Gaussian of 20° variance to spread out the calculated distributions. Figure 4.25 (left) shows the angular distribution of the various terms in the spherical harmonic expansion, including the two-lobed Σ shape and the four-lobed Π shape. Also shown is the sum of the two terms and the convolved sum. On the right of Fig. 4.25 is the measured angular distribution with the fit of the form from Equation 4.7.

Nearly concurrent measurements by Xia et al. indicated a strong forward/backward asymmetry in the momentum distribution as well as a prominent Σ contribution to the differential scattering amplitude in angle.[113] The convolution in Fig. 4.25 (left) is intended to simulate the angular resolution of that experiment, which used a diffuse target and a two-dimensional velocity map imaging (VMI) configuration to map the momentum.[67] By contrast, the present data show a slight asymmetry and a very small Σ contribution, with the entire angular distribution being fairly well modeled using only Π scattering terms convoluted with the experimental angular resolution. Allan and Skalický pointed out that the Π contribution would arise from dissociation along the direct pathway, over the ridge in the

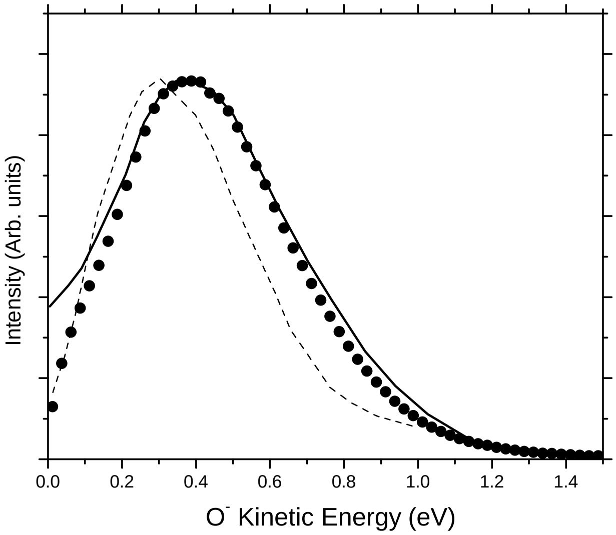

Figure 4.24: Distributions of kinetic energy of O^- fragments from dissociative attachment to N_2O. The current results (black dots) are consistent with earlier results by Chantry[110] (black line). Recent results by Xia[113] show a slightly lower peak in the KE distribution. All data have been normalized to the same peak height.

potential energy surface (see Fig. 4.21), while the Σ contribution would arise from dissociation along the bending pathway.[114] The present data, then, indicate that the dissociation at 2.3 eV proceeds mainly via the direct, non-bending geometry.

Figure 4.25: Polar angular distributions of O^- ions. (left) The spherical harmonics for the Σ (two-lobed) state and the Π (four-lobed) contributions. The larger solid curve is the sum of both contributions, and the large dotted curve is the sum convolved with the expected angular resolution of the Xia experiment.[113] (right) Angular distribution data with the Π angular distribution (solid line). The dotted line is that distribution convolved with the angular resolution of the present apparatus. The present data suggests that the dissociation can be characterized by a predominantly Π contribution.

5 — Summary and Future Work

This work has detailed the design and operation of a unique apparatus which allows for the study of electron-molecule interactions and its specific application to the study of dissociative electron attachment to a number of molecular species. In the context of recent developments in low-energy electron interactions with biological matter, the importance of dissociative electron attachment and the understanding of its dependence on molecular orientation, states, and incident electron energy is apparent. The present apparatus attempts to contribute to the body of knowledge by providing a dedicated DEA-focused apparatus with a low energy, spatially-confined target in the form of a skimmed, supersonic gas jet. The position-sensitive detection coupled with list-mode data acquisition makes the apparatus both flexible and powerful in its design. The present observations have aided in the theoretical understanding of the dissociation of negative ions formed by attachment and have also addressed some discrepancies in long-studied molecules.

In O_2, further evidence of a forward and backward contribution to the O^- ion yield (as a function of the ejection angle) has given credence to the involvement of the $^4\Sigma_u^-$ state in attachment to O_2 at 8-9 eV. For CO_2, observation of the resonance at 8 eV with improved angular resolution has shown a non-axial recoil effect in the O^- distribution following attachment. Additionally, the importance of properly weighting momentum data with a bimodal kinetic energy distribution is demonstrated. At 4 eV, a momentum distribution drastically different from the expected results (based on long-standing predictions) has prompted a new theoretical model for the dynamics of the transient negative ion along the potential energy surface. Finally, observations of O^- production from attachment to N_2O at the 2.3

eV resonance, along with analysis of the angular distributions using partial wave scattering amplitudes, have shown that the dissociation arises mainly from interactions with the molecule's Π state, implying a direct dissociation of the TNI with little contribution from the indirect, bending dissociation pathway.

Several opportunities for future exploration are available either using the present apparatus or with relatively minor modifications to the existing design. The study of the dynamics of dissociative attachment to acetylene (C_2H_2) is a possible experimental direction utilizing the present design with gas phase targets. Recent experimental and theoretical work on this system could benefit from the angle-resolved study of DEA at two known resonances.[115–117] Another experimental avenue may be to use a seeded target with an inert carrier gas to deliver the target, allowing alignment of the molecular target along the longitudinal axis during the supersonic expansion.[118,119] In moving beyond gas targets, the jet pedestal described in Chapter 2 is currently being modified to accept liquid targets so that species like formic acid (HCOOH) can be studied. In the specific case of formic acid, this could help resolve a standing dispute on the dissociative nature of the TNI into the formate anion, $HCOO^-$.[120–123]

With the development of new applications for DEA in the biological, health, and environmental sciences, experiments such as that described in this work should have a fruitful and important role in the study of electron-molecule interactions.

Appendix

A: Molecular Term Symbols for O_2

Since diatomic oxygen is one of the molecules observed in this work and it serves as a relatively simple case of term symbol determination in diatomic molecules, it is presented here as an example. Oxygen has atomic number 8, with two $1s$ electrons, two $2s$ electrons, and four p orbital electrons (see Figure 5.1). The ground state configuration of atomic oxygen is $1s^2 2s^2 2p^4$.

In the diatomic oxygen molecule, the $1s$ atomic orbitals form bonding (σ_{1s}) and anti-bonding (σ_{2s}) molecular orbitals with a total of four electrons, as do the $2s$ atomic orbitals. The atomic p_z orbitals form the σ_{2p_z} and $\sigma^*_{2p_z}$ with two electrons, and the atomic p_x and p_y orbitals form π and π^* bonds. The π bonds are filled by four electrons and the last π^* orbitals are occupied by one electron each from the two O atoms.

Since these π^* bonds are (doubly) degenerate, they are not distinguished from each other, but the arrangement of the two remaining electrons in these orbitals affects the energy and symmetry of the state. Since electrons are fermions and cannot have exactly the same set of quantum numbers (including spin), there is a limited number of possible configurations, and the quantum numbers, as well as how the states transform under reflection, determines the term symbols of the molecular states. Each electron can occupy the π state with either $m_l = +1$ or -1, and these states are often referred to as π_+ and π_-, respectively.[1] Each electron can then be in π_+ or π_- as well as having spin up ($\uparrow$) or spin down ($\downarrow$), but again, they cannot have the same value for both spin and m_l at the same time.[44]

---

[1] Classically, this corresponds to clockwise/counterclockwise rotation about the internuclear axis; quantum mechanically, it is the projection of the orbital angular momentum along that axis.

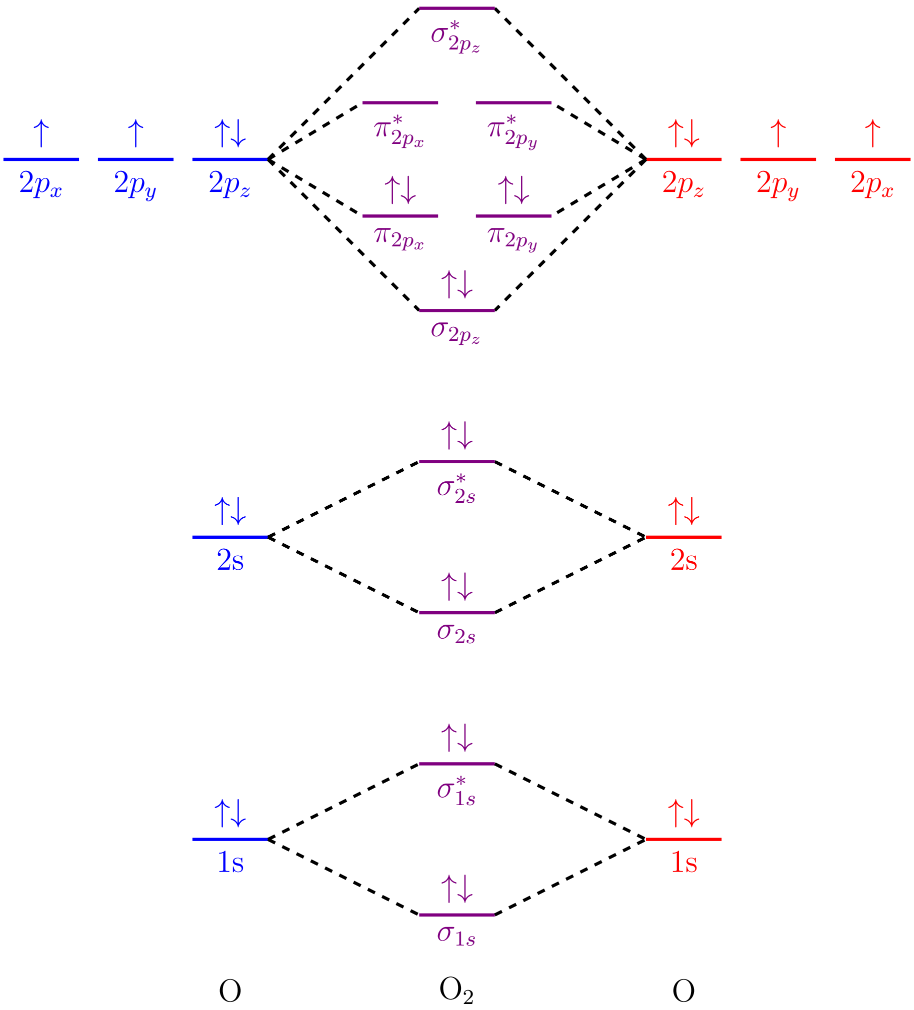

Figure 5.1: Energy level diagram for the O_2 molecule. Energy increases vertically and the molecular orbitals (middle) are formed by the mixing of atomic orbitals of like energy. The last two electrons in the molecule are left out, since several different configurations are possible for the ground state (see figure below).

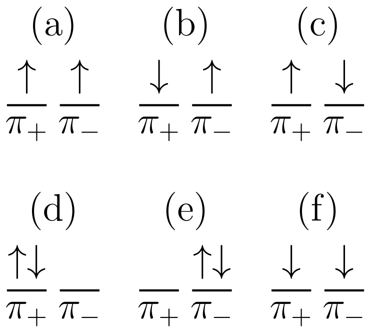

Figure 5.2: Possible electron configurations for the two unpaired electrons in diatomic oxygen. Configurations (d) and (e) have $\Lambda = \pm 2$, while the other four configurations form states with $\Lambda = 0$.

Figure 5.2 enumerates the possible electron configurations for the two unpaired electrons in diatomic oxygen. The states for which the arrows are antiparallel give $S = 0$ (singlet states) and those for which the arrows are parallel give $S = 1$ (triplet states). Due to the values of m_l for the π_+ and π_- orbitals, states (a), (b), (c), and (f) have $\Lambda = 0$ (Σ states) and states (d) and (e) have $\Lambda = \pm 2$ and $S = 0$ ($^1\Delta$ states). For (b) and (c), symmetric and antisymmetric sums of the two states must be constructed so that the total wave function has a definite symmetry. This results in both singlet and triplet states, $^1\Sigma$ and $^3\Sigma$.

The π^* (antibonding) orbitals are all of *gerade* inversion symmetry because the p orbitals that form them are of opposite phase, while the π (bonding) orbitals below them (in energy) are formed by like-phased p orbitals, giving overall *ungerade* parity. The two remaining electrons, then, are both filling *gerade* orbitals in each case. Therefore, all these molecular states are of *gerade* inversion parity, so the g subscript is left off for now.

The Σ states are further distinguished by a + or - symbol indicating their symmetry with respect to reflection. To determine this symbol, one examines the (b) and (c) states and observes that the reflection operator σ_v (which exchanges π_+ and π_-) turns (b) into (c) and vice versa. Thus, the sum of these states is symmetric under σ_v, so their term symbol has the (+) sign. In the case of (a) and (f), σ_v doesn't exchange the states, but rather leaves the spins opposite each other after the reflection, so these states and their term symbol receive the (-) sign. Thus, the three term symbols implied by the ground configuration of O_2 are:

$$^3\Sigma_g^- \quad ^1\Delta_g \quad ^1\Sigma_g^+ \tag{5.1}$$

The determination of the energy ordering is guided by *Hund's rules*. The first says that the term with the highest spin multiplicity (left superscript) is the lowest in energy. If the multiplicities are equal, the second rule says that the state with the highest orbital angular momentum quantum number (Λ) is lowest in energy.[44] From these, we see that the ground state is $^3\Sigma_g^-$, followed by $^1\Delta_g$ then $^1\Sigma_g^+$.

B: Analysis Software

The data acquisition program Cobold saves data in *list mode* format, which means that each pulse that is received by the TDC card is written and saved explicitly, so that the events can be analyzed and reconstructed in any manner offline. However, data analysis capability directly in Cobold is limited, so the data files must be converted to a format readable by ROOT,[77] a more robust analysis and visualization package.

Cobold itself uses a startup file which configures the program for both the viewing and acquisition of data. In either mode, the software reads the file *startup.ccf* for instructions on what data to retrieve, how to gate (filter) the data, and what to plot. The file contains mainly four different types of statements: parameters, coordinates, conditions, and define statements. Parameters are typically unchanged once the detector is fully operational. They include settings that, for example, tell the software which channel of the TDC serves as the time reference, or what type of TDC card is in use. Parameter statements include a first argument labeling the parameter to be set, and a second argument which sets its value. Coordinates represent the actual data retrieved from the card. These include low-level data such as an event counter, event rate, and pulse times for the individual TDC channels, as well as calculated values such as the time of flight and position information. A library file called *DAn_Standard.dll*, which is compiled seperately and used by the software during acquisition, calculates data such as TOF and passes it to the *startup.ccf* file sequentially. That is, the coordinates are passed sequentially via elements in an array from the .dll, so that they are unlabeled in the .ccf file and are retrieved in the same order. Conditions are statements which define limits on any coordinate retrieved by the .ccf file to allow the data to be gated during acquisition. For example, the line

Listing 5.1: Example condition in startup.ccf

```
condition sumx,-50,-45,sumx
condition sumy,-47,-41,sumy
condition sumx,and,sumy,sumxy
```

sets a condition on the x time sum to be between -50 ns and -45 ns and labels this condition "sum x". A similar condition is placed on the y signals. The two conditions are then combined with an AND operation to produce "sumxy". These conditions are determined by inspection of plots like in Fig. 2.16.

The last type of statement is a define statement, either define1 or define2, which instructs the software to create 1D and 2D histograms, respectively. One-dimensional histograms display the distribution of a particular value (coordinate), and two-dimensional histograms show correlations between two coordinates. These plots are called *spectra*, and their definitions accept the conditions defined above as arguments which restrict the data in the spectrum. For example,

Listing 5.2: Example spectra definitions in startup.ccf

```
define1 0,40000,5,TOF,TOF[ns],,always,TOF in ns
define2 0,9000,5,TOF,TOF[ns],-50,50,.5,PosX,PosX[mm],,sumxy,Xfish
```

defines a 1D histogram with range 0 to 40000 ns, a bin size of 5, for the coordinate TOF, axis label "TOF [ns]", and with no condition on the data ("always"). The double comma before "always" is a space for an unused weighting parameter, and the title of the histogram is "TOF in ns". The second line defines a 2D histogram with the condition sumxy imposed and title "Xfish" with a similar argument list for two axes.

As should be apparent, a large amount of data analysis and visualization in this manner could easily become cumbersome. LMF2Root allows both the conversion of the list-mode files to the ROOT format and the use of the C++ programming language to perform the calculations. The basic structure of LMF2Root from the user's perspective consists of a configuration file, a “sort and write” routine, and an analysis code file. The configuration file plays a similar role to *startup.ccf* in Cobold. It identifies the detector type(s), channels for the anode and MCP signal wires, and also tells LMF2Root whether the input file should be run through the sort and write routine or through the analysis. The sort and write code is the part of the software that reads the .lmf (list mode file) and writes it to a ROOT file, but in the process, it can also be used to identify different reaction channels in preparation for the analysis phase. This is useful because some experiments involve multiple reaction pathways, each with two or more ion fragments, and ions coincident from the same reaction must be identified via their momentum and species. Since this work focuses on dissociative attachment, which only produces an anion and a neutral fragment, this functionality is not normally used, and the sort and write routine is used to prepare the file for analysis without sorting or filtering the data. The analysis code is run on the ROOT file which results from the sort routine and performs the calculations of momentum, energy, and ion ejection angle and also fills the histograms which are opened by ROOT for display. The sort and write process is much slower and typically can take several hours to run through an entire data file, but this process only needs to be performed once for a given data set. Once the ROOT file has been written, the analysis code, which usually takes less than five minutes, can be run to reflect changes in any calculations. The configuration file informs the software whether it is in the sort and write phase or the analysis phase and identifies the file(s) that will be written to.

A representative sample of analysis code, for 4.4 eV electrons on CO_2, is provided in Appendix C. The compiled program runs through the analysis routine for each event. A manual shift in the position values is allowed in order to correct for a misalignment or offset in the momentum distribution with respect to the center of the detector. In this case, no such correction was needed. Then, the momentum in the x and y directions is calculated (p_x and p_y). This is simply calculated as

$$p_x = m\frac{x}{t} \qquad p_y = m\frac{y}{t} \tag{5.2}$$

where t is the time of flight, m is the ion mass, and x and y are the positions on the detector. This is multiplied by a conversion factor for atomic units. The momentum calculation for the time of flight direction, however, requires the fit and momentum conversion from the simulations. The Mathematica notebook fits the relationship of the initial momentum to the flight times with a third order polynomial which is imported into the analysis code to do the calculation. For the simulations shown above,

$$p_t = -267\,\mathrm{AU} + (0.2772\,{}^{\mathrm{AU}}\!/\!_{\mathrm{ns}})t - (4.752 \times 10^{-5}\,{}^{\mathrm{AU}}\!/\!_{\mathrm{ns}^2})t^2 + (1.812 \times 10^{-9}\,{}^{\mathrm{AU}}\!/\!_{\mathrm{ns}^3})t^3 \tag{5.3}$$

The components of the momentum in Cartesian coordinates are converted to spherical coordinates using the usual transformations in order to facilitate plotting of the angular dependence and gating by angle.

The above methods are useful for the analysis of interactions which produce a single ion, as in dissociative attachment, which comprises the bulk of this work. The next chapter will also include some results for dissociative ionization, for which several dissociation channels with more than one ionic fragment are accessible, and the analysis will be slightly more complicated because the different channels must be identified and analyzed seperately. This will reveal a unique challenge in the dissociative attachment experiments, where only a single anion is detected, and for which there is consequently less data from which to reconstruct the dissociation dynamics.

C: Analysis Code

LMF2Root

Listing 5.3: Example analysis code (LMF2Root) for 4.4 eV CO_2

```
#pragma warning(disable : 4800)
#include ”OS_Version.h”

#include ”TCanvas.h”
#include ”TH1D.h”
#include ”TH2D.h”
#include ”TApplication.h”
#include ”TFile.h”
#include ”TTree.h”
#include ”TNtupleD.h”

#include <math.h>
#include ”rootstuff.h”
#include ”Histo.h”
#include ”TF1.h”
#include ”TMinuit.h”

#include ”functions.h”
#include ”Ueberstruct.h”

//#include ”resort64c.h”

//4.4eV//

/////////////////////////////////////////////////////////////////////////////////////////////////////////////
int analysis(__int64 eventcounter, double  parameter[], TTree * Data, Ueberstruct * Ueber)
/////////////////////////////////////////////////////////////////////////////////////////////////////////////
{

        Histo * Hist = Ueber->Hist;
        Ueber->start_new_root_file = false;

        int plot=0;                                                                    //plot identifier
        double sumx=0,sumy=0;
        double r1x=0,r1y=0,r1tof=0;
        double px=0,py=0,pt=0,KE=0;
```

```
        double pmag=0;
        double pr=0,ptheta=0,pphi=0;
        const double amu = 1.66053886e-27;
        const double SItoAUmom = 1.992851565e-24;
        const double echarge = 1.60217646e-19;
        const double pi = acos(-1.0);

        double NTupleData[6];
        bool WriteNTuple = false;

        if(eventcounter == 0) {
                Ueber->EntriesInFile = 0;
                Ueber->eventswritten = 0;
        }

        if(Ueber->EntriesInFile == 0) {

                Data->SetBranchAddress(”r1x”,&r1x);
                Data->SetBranchAddress(”r1y”,&r1y);
                Data->SetBranchAddress(”r1tof”,&r1tof);
                Data->SetBranchAddress(”timesum_x”,&sumx);
                Data->SetBranchAddress(”timesum_y”,&sumy);
        }

        Data->GetEntry(Ueber->EntriesInFile);

        if(Ueber->EntriesInFile < Data->GetEntries()-1) {
                ++Ueber->EntriesInFile;
        } else {
                Ueber->EntriesInFile = 0;
        }

// Include your analysis here.
//-----------------------------------------------------------------------------------------------

//4.4eV CO2//

//shift detector positions to center the distribution
r1y = r1y - 1.5;
//r1x = r1x + 0.5;

///////begin calculate momenta////////

//x and y momenta calculated from m*(dx/dt), with appropriate conversions for atomic units
px = (16*amu*r1x*(0.001)/(r1tof*pow(10.0,-9.0)))/SItoAUmom;
py = (16*amu*r1y*(0.001)/(r1tof*pow(10.0,-9.0)))/SItoAUmom;

        //t momentum function is imported from fit with Simion results; units are already AU
pt =  253.983 - 0.00138749*r1tof - (2.74144e-6)*(r1tof)*(r1tof) - 1.07326e-10*(r1tof)*(r1tof)*(r1tof);

pmag = sqrt(px*px + py*py + pt*pt);

        //convert momenta to spherical coordinates to make angle plots easier
pr = pmag;
pphi = atan2(pt, px);
ptheta = acos(py/pr);
```

```
///////end calculate momenta//////////

//calculate kinetic energy
KE = (px*px + py*py + pt*pt)*27.211/(2*16.0*1836.152672);
//calculate kinetic energy

///////////////////////below: some preliminary plots with no sum gating, folder ”all” in ROOT tree///////

        //simple 1D time-of-flight histogram
        Hist->fill1(99,”TOF”,r1tof,1.,”TOF”,2000,2000,8000,”TOF [ns]”,”all”);

        //2D plots of momentum in each of the three planes
        Hist->fill2(100,”MomXY”,px,py,1.,”Momentum XY”,50,-80,80.,
                ”Momentum X [AU]”,50,-80.,80.,”Momentum Y [AU]”,”all”);

        Hist->fill2(101,”MomXT”,pt,px,1.,”Momentum XT”,50,-100,100.,
                ”Momentum T [AU]”,50,-100.,100.,”Momentum X [AU]”,”all”);

        Hist->fill2(102,”MomYT”,pt,py,1.,”Momentum YT”,50,-80,80.,
                ”Momentum T [AU]”,50,-80.,80.,”Momentum Y [AU]”,”all”);

        //2D plot of position on the detector
        Hist->fill2(103,”PosXY”,r1x,r1y,1.,”Position XY”,500,-50,50.,”Position X [mm]”,500,-50.,50.,
                ”Position Y [mm]”,”all”);

        //Plot of detector position in the TOF range of the main peak
        if(r1tof > 6200 && r1tof < 7200)
        {
                Hist->fill2(104,”PosXY tof”,r1x,r1y,1.,”Position XY”,250,-50,50.,
                        ”Position X [mm]”,250,-50.,50.,”Position Y [mm]”,”all”);
        }

        //”fish” plots: position on detector (x or y) vs time of flight
        Hist->fill2(105,”FishY”,r1tof,r1y,1.,”TOF”,1000,5000,8000,
                ”Position Y [mm]”,100,-50.,50.,”Position Y [mm]”,”all”);

        Hist->fill2(106,”FishX”,r1tof,r1x,1.,”TOF”,1000,5000,8000.,
                ”Position X [mm]”,100,-50.,50.,”Position X [mm]”,”all”);

        //”filet-o-fish” plots: position (x or y) on detector vs time of flight only for
        //small momenta in the other direction (y or x)
        //to form a ”slice” of the fish so the structure is more visible

        if(px > -5.0 && px < 5.0)
        {
                Hist->fill2(107,”FishY middle”,r1tof,r1y,1.,”TOF”,1000,5000,8000,
                        ”Position Y [mm]”,100,-50.,50.,”Position Y [mm]”,”all”);
        }

        if(py > -5.0 && py < 5.0)
        {
                Hist->fill2(108,”FishX middle”,r1tof,r1x,1.,”TOF”,1000,5000,8000.,
                        ”Position X [mm]”,100,-50.,50.,”Position X [mm]”,”all”);
        }

        //detector position plot for only the center (100 ns) of the main TOF peak
```

```
        if(r1tof > 6700 && r1tof < 6800)
        {
                Hist->fill2(109,"PosXY tof mid",r1x,r1y,1.,"Position XY",250,-50,50.,
                        "Position X [mm]",250,-50.,50.,"Position Y [mm]","all");
        }

///////////////////////above: some preliminary plots with no sum gating, folder "all" in ROOT tree////////


///////////////////////below: plots subject to the sum xy gates, folder "sumxy" in ROOT tree////////

        //actual sumx and sumy values come from initial sort and write routine plots
        if(sumx < -45 && sumx > -52 && sumy < -40 && sumy > -50)
        {
                //Momentum plots in three dimensions and position plot in detector
                //plane with no other gates

                Hist->fill2(200,"MomXY",px,py,1.,"Momentum XY",50,-60,60.,
                        "Momentum X [AU]",50,-60.,60.,"Momentum Y [AU]","sumxy");

                Hist->fill2(201,"MomXT",pt,px,1.,"Momentum XT",50,-100,100.,
                        "Momentum T [AU]",50,-100.,100.,"Momentum X [AU]","sumxy");

                Hist->fill2(202,"MomYT",pt,py,1.,"Momentum YT",50,-60,60.,
                        "Momentum T [AU]",50,-60.,60.,"Momentum Y [AU]","sumxy");

                Hist->fill2(203,"PosXY",r1x,r1y,1.,"Position XY",500,-50,50.,
                        "Position X [mm]",500,-50.,50.,"Position Y [mm]","sumxy");

                //Position for ions in the TOF peak for O-
                if(r1tof > 6200 && r1tof < 7200)
                {
                        Hist->fill2(204,"PosXY",r1x,r1y,1.,"Position XY",500,-50,50.,
                                "Position X [mm]",500,-50.,50.,"Position Y [mm]","sumxy");
                }

                //Fish plots in X and Y, no slicing
                Hist->fill2(205,"FishY",r1tof,r1y,1.,"TOF",1000,5000,10000.,
                        "TOF [ns]",120,-30.,30.,"Position Y [mm]","sumxy");

                Hist->fill2(206,"FishX",r1tof,r1x,1.,"TOF",1000,5000,10000.,
                        "TOF [ns]",120,-30.,30.,"Position X [mm]","sumxy");

                //Sliced X fish plot, within 3 au momentum from y=0
                if( r1y > -3.0 && r1y < 3.0)
                {
                        Hist->fill2(401,"FishX slice",r1tof,r1x,1.,"TOF",1000,6000,10000.,
                                "TOF [ns]",120,-30.,30.,"Position X [mm]","sumxy");
                }

                //Momentum collar gates, using +/- 5 degrees for acceptance angle,
                //also limiting the total momentum to 40 au for cleaner-edged figure

                if(asin(py/pmag)*180.0/pi < 5.0 && asin(py/pmag)*180.0/pi > -5.0 && pmag < 40.0 )
                {
                        Hist->fill2(207,"MomXT sliced (collar, large bins)",pt,px,1.,
```

```
                ”Momentum XT”,30,-50,50.,”mom. T [a.u.]”,30,-50.,50.,
                ”mom. X [a.u.]”,”sumxy”);

        Hist->fill2(2070,”MomXT sliced (collar, small bins)”,pt,px,1.,
                ”Momentum XT”,50,-50,50.,”mom. T [a.u.]”,50,-50.,50.,
                ”mom. X [a.u.]”,”sumxy”);

        //Kinetic energy plot subject to the same collar gates
        //for comparison with full 4pi KE plots

        Hist->fill1(223,”KE (collar gate, XT)”,KE,1.,
                ”Kinetic Energy”,2000,0,2.,”KE [eV]”,”sumxy”);

        //Angular data for polar plot; Ion yield as a function of
        //azimuthal angle (in XT plane)

        if(pmag > 10.0)
        {
                Hist->fill1(250,”Mom. Angle XT all angles”,pphi*180.0/pi,1.0,
                        ”Mom. Ang. Dep. (XT-plane)”,60,-180,180.,”#phi [deg]”,”sumxy”);
        }

        //For ions with momentum mostly in XT plane, plot the angular dependence as above.
        ==I had to split this up into
        //the positive pt and negative pt components to make it work
        if((px*px + pt*pt) > pow(23.0,2.0) && (px*px + pt*pt) < pow(48.6,2.0))
        {
                if(pt > 0)
                        {
                                Hist->fill1(208,”Mom. Angle XT”,
                                        acos(px/(sqrt(px*px + pt*pt)))*180.0/pi,1.,
                                        ”Mom. Ang. Dep. (XT-plane)”,40,0,180.,
                                        ”#Theta [deg]”,”sumxy”);
                        }
                if(pt < 0)
                        {
                                Hist->fill1(208,”Mom. Angle XT”,
                                        fabs(acos(px/(sqrt(px*px + pt*pt))))*180.0/pi,1.,
                                        ”Mom. Ang. Dep. (XT-plane)”,40,0,180.,
                                        ”#Theta [deg]”,”sumxy”);
                        }
        }

}


//Collar gate in YT plane with corresponding KE plot
if( asin(px/pmag)*180.0/pi < 5.0 && asin(px/pmag)*180.0/pi > -5.0 && pmag < 77.0 )
{
        Hist->fill2(209,”MomYT sliced (collar)”,pt,py,1.,”Momentum YT”,50,-60,60.,
                ”Momentum T [AU]”,50,-60.,60.,”Momentum Y [AU]”,”sumxy”);

        Hist->fill1(224,”KE (collar gate, YT)”,KE,1.,”Kinetic Energy”,
                2000,0,2.,”KE [eV]”,”sumxy”);
}
```

```
//Collar gate in XY plane with corresponding KE plot
if( asin(pt/pmag)*180.0/pi < 5.0 && asin(pt/pmag)*180.0/pi > -5.0 && pmag < 77.0 )
{
        Hist->fill2(210,"MomXY sliced (collar)",px,py,1.,"Momentum XY",50,-60,60.,
                "Momentum X [AU]",50,-60.,60.,"Momentum Y [AU]","sumxy");
        Hist->fill1(225,"KE (collar gate, XY)",KE,1.,"Kinetic Energy",
                2000,0,2.,"KE [eV]","sumxy");

        //For ions with momentum mostly in XY plane, plot the angular dependence as above.
        //I had to split this up into
        //the positive py and negative py components to make it work
        if((px*px + py*py) > pow(23,2.0) && (px*px + py*py) < pow(48.6,2.0))
        {
                if(py > 0)
                        {
                                Hist->fill1(211,"Mom. Angle XY",
                                        acos(px/(sqrt(px*px + py*py)))*180.0/pi,1.,
                                        "Mom. Ang. Dep. (XY-plane)",40,0,180.,
                                        "#Theta [deg]","sumxy");
                        }
                if(py < 0)
                        {
                                Hist->fill1(211,"Mom. Angle XY",
                                        fabs(acos(px/(sqrt(px*px + py*py))))*180.0/pi,1.,
                                        "Mom. Ang. Dep. (XY-plane)",40,0,180.,
                                        "#Theta [deg]","sumxy");
                        }
        }
}


//Just plane KE and TOF plots in wide ranges
Hist->fill1(213,"KE",KE,1.,"Kinetic Energy",2000,0,10.,"KE [eV]","sumxy");
Hist->fill1(214,"TOF",r1tof,1.,"TOF",2000,0,10000,"TOF [ns]","sumxy");

//Flat slices in momentum in all three planes for comparison to collar gates
if(pmag < 77.0 ){

        if(abs(py) < 5.4){
                Hist->fill2(215,"MomXT sliced (flat)",pt,px,1.,"Momentum XT",50,-60,60.,
                "Momentum T [AU]",50,-60.,60.,"Momentum X [AU]","sumxy");
                Hist->fill1(226,"KE (flat gate, XT)",KE,1.,"Kinetic Energy",
                2000,0,2.,"KE [eV]","sumxy");
        }
        if(abs(px) < 5.4){
                Hist->fill2(216,"MomYT sliced (flat)",pt,py,1.,"Momentum YT",50,-50,50.,
                "Momentum T [AU]",50,-50.,50.,"Momentum Y [AU]","sumxy");
                Hist->fill1(227,"KE (flat gate, YT)",KE,1.,"Kinetic Energy",
                2000,0,2.,"KE [eV]","sumxy");
        }
        if(abs(pt) < 5.4){
                Hist->fill2(217,"MomXY sliced (flat)",px,py,1.,"Momentum XY",50,-50,50.,
                "Momentum X [AU]",50,-50.,50.,"Momentum Y [AU]","sumxy");
                Hist->fill1(228,"KE (flat gate, XY)",KE,1.,"Kinetic Energy",
                2000,0,2.,"KE [eV]","sumxy");
        }
```

```
}


//Collar gates with smaller acceptance angle in XT plane and KE plot
if(asin(py/pmag)*180.0/pi < 1.0 && asin(py/pmag)*180.0/pi > -1.0 && pmag < 77.0 )
{
        Hist->fill2(218,"MomXT sliced (collar, thin)",pt,px,1.,"Momentum XT",50,-60,60.,
        "Momentum T [AU]",50,-60.,60.,"Momentum X [AU]","sumxy");

        if((px*px + pt*pt) > pow(43.8,2.0) && (px*px + pt*pt) < pow(77,2.0))
        {
                if(pt > 0)
                        {
                                Hist->fill1(219,"Mom. Angle XT thin",
                                        acos(px/(sqrt(px*px + pt*pt)))*180.0/pi,1.,
                                        "Mom. Ang. Dep. (XT-plane)",40,0,180.,
                                        "#Theta [deg]","sumxy");
                        }
                if(pt < 0)
                        {
                                Hist->fill1(219,"Mom. Angle XT thin",
                                        fabs(acos(px/(sqrt(px*px + pt*pt))))*180.0/pi,1.,
                                        "Mom. Ang. Dep. (XT-plane)",40,0,180.,
                                        "#Theta [deg]","sumxy");
                        }
        }

        Hist->fill1(220,"KE (collar gate)",KE,1.,"Kinetic Energy",2000,0,2.,
                "KE [eV]","sumxy");

}


//Momentum plots of transverse vs longitudinal momentum; keeps all the data (no gating),
//but leaves a hole along the center vertical

if(r1tof > 7600 && r1tof < 8800)
{
        if( (py < 0) ^ (pt < 0) )
        {
                Hist->fill2(501,"MomTL",-sqrt(py*py + pt*pt),px,1.,
                        "Mom. Long. v. Trans.",100,-50,50,
                        "Transverse Momentum",100,-50,50,"Longitudinal Momentum","sumxy");
        }
        else
        {
                Hist->fill2(501,"MomTL",sqrt(py*py + pt*pt),px,1.,
                        "Mom. Long. v. Trans.",100,-50,50,
                        "Transverse Momentum",100,-50,50,"Longitudinal Momentum","sumxy");
        }
}

//The phi angle is backwards; convert it to degrees and flip it around
pphi = pphi*(180/pi) + 180;
```

```
            //Plots of ion yield in both directions (elevation and azumuthal angles);
            //used for plotting the 3D data in Mathematica and POVRay
            //Need cos(theta) vs phi for Mathematica plotting routine to keep volume elements equal
            //theta vs phi plot is included just for viewing purposes

            if(pmag < 40.0 && pmag > 25.0)
            {
                  Hist->fill2(300,”Mom Theta Phi”,pphi,cos(ptheta),1.,”Momentum Angle Full”,
                  36,0,360,”Phi”,36,-1,1,”Cos(Theta)”,”sumxy”);
            }

            if(pmag < 40.0 && pmag > 25.5)
            {
                  Hist->fill2(301,”Mom Theta Phi”,pphi,ptheta,1.,”Momentum Angle Full”,
                  36,0,360,”Phi”,36,0,pi,”Theta”,”sumxy”);
            }

//////////////////////above: plots subject to the sum xy gates, folder ”sumxy” in ROOT tree//////


//////////////////////below: plots subject to the sum xy gates and TOF correction,
//folder ”sumxy and tof shift” in ROOT tree///////////////

            //Shift times of flight via a fitting function to straighten up the
            //fish plot to obey the symmetry of the experiment.
            //All the following plots are essentiall the same as in ”sumxy”,
            //just repeated to apply the TOF correction

            r1tof = r1tof - (-1.88712/2.5)*r1x - (0.13548)*r1x*r1x;

            //calculate momenta

            px = (16*amu*r1x*(0.001)/(r1tof*pow(10.0,-9.0)))/SItoAUmom;
            py = (16*amu*r1y*(0.001)/(r1tof*pow(10.0,-9.0)))/SItoAUmom;
            pt =  253.983 - 0.00138749*r1tof - (2.74144e-6)*(r1tof)*(r1tof)
                 - 1.07326e-10*(r1tof)*(r1tof)*(r1tof);
            pmag = sqrt(px*px + py*py + pt*pt);

            pr = pmag;
            pphi = atan2(pt, px);
            ptheta = acos(py/pr);

            //calculate momenta

            //calculate kinetic energy
            KE = (px*px + py*py + pt*pt)*27.211/(2*16.0*1836.152672);
            //calculate kinetic energy

            //fishes
            Hist->fill2(1001,”FishY”,r1tof,r1y,1.,”TOF”,1000,5000,10000.,”TOF [ns]”,
                  120,-30.,30.,”Position Y [mm]”,”sumxy and tof shift”);
            Hist->fill2(1002,”FishX”,r1tof,r1x,1.,”TOF”,1000,5000,10000.,”TOF [ns]”,
                  120,-30.,30.,”Position X [mm]”,”sumxy and tof shift”);

            if( r1y > -3.0 && r1y < 3.0)
```

```
{
        Hist->fill2(1003,"FishX slice",r1tof,r1x,1.,"TOF",1000,6000,10000.,
        "TOF [ns]",120,-30.,30.,"Position X [mm]","sumxy and tof shift");
}
//fishes

//flat slices in momentum//
if(pmag < 77.0 ){

        if(abs(py) < 5.4){
                Hist->fill2(1101,"MomXT sliced (flat)",pt,px,1.,"Momentum XT",50,-50,50.,
                        "Momentum T [AU]",50,-50.,50.,"Momentum X [AU]",
                        "sumxy and tof shift");

                Hist->fill1(226,"KE (flat gate, XT)",KE,1.,"Kinetic Energy",
                        2000,0,2.,"KE [eV]","sumxy and tof shift");
        }
        if(abs(px) < 5.4){
                Hist->fill2(1102,"MomYT sliced (flat)",pt,py,1.,"Momentum YT",50,-50,50.,
                        "Momentum T [AU]",50,-50.,50.,"Momentum Y [AU]",
                        "sumxy and tof shift");

                Hist->fill1(227,"KE (flat gate, YT)",KE,1.,"Kinetic Energy",
                        2000,0,2.,"KE [eV]","sumxy and tof shift");
        }
        if(abs(pt) < 5.4){
                Hist->fill2(1103,"MomXY sliced (flat)",px,py,1.,"Momentum XY",50,-50,50.,
                        "Momentum X [AU]",50,-50.,50.,"Momentum Y [AU]",
                        "sumxy and tof shift");

                Hist->fill1(228,"KE (flat gate, XY)",KE,1.,"Kinetic Energy",
                        2000,0,2.,"KE [eV]","sumxy and tof shift");
        }

}
//flat slices in momentum//

Hist->fill1(1004,"KE",KE,1.,"Kinetic Energy",2000,0,10.,"KE [eV]","sumxy and tof shift");
Hist->fill1(1005,"TOF",r1tof,1.,"TOF",2000,0,10000,"TOF [ns]","sumxy and tof shift");



// collar gates on momentum
if(asin(py/pmag)*180.0/pi < 10.0 && asin(py/pmag)*180.0/pi > -10.0 && pmag < 40.0 )
{
        Hist->fill2(1201,"MomXT sliced (collar)",pt,px,1.,"Momentum XT",50,-60,60.,
                "Momentum T [AU]",50,-60.,60.,"Momentum X [AU]","sumxy and tof shift");

        Hist->fill2(3207,"MomXT sliced (collar, large bins)",pt,px,1.,
                "Momentum XT",30,-50,50.,
                "mom. T [a.u.]",30,-50.,50.,"mom. X [a.u.]","sumxy");

        Hist->fill2(3070,"MomXT sliced (collar, small bins)",pt,px,1.,
                "Momentum XT",50,-50,50.,
                "mom. T [a.u.]",50,-50.,50.,"mom. X [a.u.]","sumxy");
```

```
        Hist->fill1(1202,"KE (collar gate, XT)",KE,1.,"Kinetic Energy",2000,0,2.,
                "KE [eV]","sumxy and tof shift");

        //Angular data for polar plot
        if(pmag > 27.0)
        {
                Hist->fill1(1301,"Mom. Angle XT all angles",pphi*180.0/pi,1.0,
                "Mom. Ang. Dep. (XT-plane)",60,-180,180.,"#phi [deg]",
                "sumxy and tof shift");
        }
        //Angular data for polar plot

        if((px*px + pt*pt) > pow(23.0,2.0) && (px*px + pt*pt) < pow(48.6,2.0))
        {
                if(pt > 0)
                        {
                                Hist->fill1(1302,"Mom. Angle XT",
                                        acos(px/(sqrt(px*px + pt*pt)))*180.0/pi,1.,
                                        "Mom. Ang. Dep. (XT-plane)",
                                        40,0,180.,"#Theta [deg]","sumxy and tof shift");
                        }
                if(pt < 0)
                        {
                                Hist->fill1(1302,"Mom. Angle XT",
                                fabs(acos(px/(sqrt(px*px + pt*pt))))*180.0/pi,1.,
                                "Mom. Ang. Dep. (XT-plane)",40,0,180.,"#Theta [deg]",
                                "sumxy and tof shift");
                        }
        }

}



if( asin(px/pmag)*180.0/pi < 5.0 && asin(px/pmag)*180.0/pi > -5.0 && pmag < 77.0 )
{
        Hist->fill2(1204,"MomYT sliced (collar)",pt,py,1.,"Momentum YT",50,-60,60.,
                "Momentum T [AU]",50,-60.,60.,"Momentum Y [AU]","sumxy and tof shift");

        Hist->fill2(2090,"MomYT sliced (collar) smaller bins",pt,py,1.,
                "Momentum YT",100,-60,60.,
                "Momentum T [AU]",100,-60.,60.,"Momentum Y [AU]","sumxy and tof shift");

        Hist->fill2(2091,"MomYT sliced (collar) smallest bins",pt,py,1.,
                "Momentum YT",200,-60,60.,
                "Momentum T [AU]",200,-60.,60.,"Momentum Y [AU]","sumxy and tof shift");

        Hist->fill1(1205,"KE (collar gate, YT)",KE,1.,"Kinetic Energy",
                2000,0,2.,"KE [eV]","sumxy and tof shift");
}

if( asin(pt/pmag)*180.0/pi < 5.0 && asin(pt/pmag)*180.0/pi > -5.0 && pmag < 77.0 )
{
        Hist->fill2(1206,"MomXY sliced (collar)",px,py,1.,"Momentum XY",50,-60,60.,
                "Momentum X [AU]",50,-60.,60.,"Momentum Y [AU]","sumxy and tof shift");
```

```
            Hist->fill1(1207,"KE (collar gate, XY)",KE,1.,"Kinetic Energy",
            2000,0,2.,"KE [eV]","sumxy and tof shift");

            if((px*px + py*py) > pow(43.8,2.0) && (px*px + py*py) < pow(77,2.0))
            {
                if(py > 0)
                    {
                        Hist->fill1(1208,"Mom. Angle XY",
                        acos(px/(sqrt(px*px + py*py)))*180.0/pi,1.,
                        "Mom. Ang. Dep. (XY-plane)",40,0,180.,"#Theta [deg]",
                        "sumxy and tof shift");
                    }
                if(py < 0)
                    {
                        Hist->fill1(1208,"Mom. Angle XY",
                        fabs(acos(px/(sqrt(px*px + py*py))))*180.0/pi,1.,
                        "Mom. Ang. Dep. (XY-plane)",40,0,180.,"#Theta [deg]",
                        "sumxy and tof shift");
                    }
            }
        }
        //collar gates on momentum

        //angular plots for 3d images
        pphi = pphi*(180/pi) + 180;

        if(pmag < 40.0 && pmag > 25.0)
        {
            Hist->fill2(1401,"Mom Theta Phi",pphi,cos(ptheta),1.,
            "Momentum Angle Full",36,0,360,"Phi",36,-1,1,"Cos(Theta)","sumxy and tof shift");
        }

        if(pmag < 40.0 && pmag > 25.5)
        {
            Hist->fill2(1402,"Mom Theta Phi",pphi,ptheta,1.,
            "Momentum Angle Full",36,0,360,"Phi",36,0,pi,"Theta","sumxy and tof shift");
        }
        //angular plots for 3d images

    }

///////////////////////below: plots subject to the sum xy gates and TOF correction,
folder "sumxy and tof shift" in ROOT tree///////////////

//-----------------------------------------------------------------------------------------------


    if(WriteNTuple) {
        Hist->NTupleD(9999,"Data","H20BESSY08","r1x:r1y:r1tof:sumgood", 32000, NTupleData);
        Ueber->eventswritten++;
    }

    if(parameter[57]>0.5) {
        unsigned __int64 max_events = (unsigned __int64)(parameter[56]+0.1);
        if(Ueber->eventswritten > (__int64)max_events && max_events > 0) {
            Ueber->start_new_root_file = true;
            Ueber->eventswritten = 0;
```

```
                    Hist->Reset();
                }
        }

        return 0;
}
```

User Program (SIMION)

Listing 5.4: User program for SIMION

```
simion.workbench_program()

--Error Warnings
--1. If you get an "arithmetic on nil" or "compare number with nil" error
        --from Simion on flying the ions, check that the particle definitions are
        --reasonable and originate where they should

adjustable delay_time_ns = 0
adjustable turn_on_time_ns = 0
adjustable pulse_voltage = 0
adjustable pulse_length_ns = 0
adjustable Excel_Plot_True1_False0 = 0
Ion_initialize_count = 1
Ion_count = 1
--initial_Px = 100000 --au momentum
--initial_Py = 100000 --au momentum
--initial_Pz = 100000 --au momentum

function segment.tstep_adjust()

        local ion_time_step_ns = 0.1
        ion_time_step = ion_time_step_ns * 10^-3

end

function segment.initialize()

        pulse_length = pulse_length_ns * 10^-3
        delay_time = delay_time_ns * 10^-3
        turn_on_time = turn_on_time_ns * 10^-3

        local vx = ion_vx_mm * (1/1000) * ( 1/( 10^(-6) ) ) -- convert to SI
        local vy = ion_vy_mm * (1/1000) * ( 1/( 10^(-6) ) ) -- convert to SI
        local vz = ion_vz_mm * (1/1000) * ( 1/( 10^(-6) ) ) -- convert to SI

        local ion_mass_kg = ion_mass * 1.660538782e-27
        initial_Px = ion_mass_kg * vx / 1.992851565e-24 --au momentum
        initial_Py = ion_mass_kg * vy / 1.992851565e-24 --au momentum
        initial_Pz = ion_mass_kg * vz / 1.992851565e-24 --au momentum

        if ion_number == 1 and Excel_Plot_True1_False0 == 1 then
                excel = luacom.CreateObject("Excel.Application")
                excel.Visible = false

                wb = excel.Workbooks:Add()

                ws2 = wb.Worksheets(1)

                ws2.Cells(1,1).Value2 = "Ion mass [amu]"
```

```
                ws2.Cells(1,2).Value2 = "El Angle"
                ws2.Cells(1,3).Value2 = "Az Angle"
                ws2.Cells(1,4).Value2 = "Initial KE [eV]"
                ws2.Cells(1,5).Value2 = "Initial x [mm]"
                ws2.Cells(1,6).Value2 = "Initial y [mm]"
                ws2.Cells(1,7).Value2 = "Initial z [mm]"
                ws2.Cells(1,8).Value2 = "Final x [mm]"
                ws2.Cells(1,9).Value2 = "Final y [mm]"
                ws2.Cells(1,10).Value2 = "Final z [mm]"
                ws2.Cells(1,11).Value2 = "Sqrt(Ion mass [amu])"
                ws2.Cells(1,12).Value2 = "Final KE [au]"
                ws2.Cells(1,13).Value2 = "Radius [mm]"
                ws2.Cells(1,14).Value2 = "TOF [ns]"
                ws2.Cells(1,15).Value2 = "Initial Px [au]"
                ws2.Cells(1,16).Value2 = "Initial Py [au]"
                ws2.Cells(1,17).Value2 = "Initial Pz [au]"
                ws2.Cells(1,19).Value2 = "Simulation Parameters"
                ws2.Cells(2,19).Value2 = "Delay Time (ns)"
                ws2.Cells(2,20).Value2 = delay_time_ns
                ws2.Cells(3,19).Value2 = "Pulse Voltage (V)"
                ws2.Cells(3,20).Value2 = pulse_voltage
                ws2.Cells(4,19).Value2 = "Pulse Length (ns)"
                ws2.Cells(4,20).Value2 = pulse_length_ns
                ws2.Cells(5,19).Value2 = "Turn-on Time (ns)"
                ws2.Cells(5,20).Value2 = turn_on_time_ns

        end

        if Excel_Plot_True1_False0 == 1 then

                Ion_initialize_count = Ion_initialize_count + 1
                ws2.Cells(Ion_initialize_count,1).Value2 = ion_mass
                ws2.Cells(Ion_initialize_count,2).Value2 = (180/math.pi) *
                        atan2(vy, (vx^2+vz^2)^(0.5) )
                ws2.Cells(Ion_initialize_count,3).Value2 = (180/math.pi) *
                        atan2(-vz, vx )
                ws2.Cells(Ion_initialize_count,4).Value2 = 0.5*
                        (ion_mass*1.660538782e-27 )*(vx^2 + vy^2 + vz^2) *
                        1.0/(1.602176487e-19) -- in eV
                ws2.Cells(Ion_initialize_count,5).Value2 = ion_px_mm
                ws2.Cells(Ion_initialize_count,6).Value2 = ion_py_mm
                ws2.Cells(Ion_initialize_count,7).Value2 = ion_pz_mm
                ws2.Cells(Ion_initialize_count,15).Value2 = initial_Px
                ws2.Cells(Ion_initialize_count,16).Value2 = initial_Py
                ws2.Cells(Ion_initialize_count,17).Value2 = initial_Pz

        end
end


function segment.init_p_values()
        --adj_elect00 = 0.0
        adj_elect01 = 0.0
        adj_elect02 = 0.0
        adj_elect03 = 0.0
        adj_elect04 = 0.0
```

```
        adj_elect05 = 0.0
        adj_elect06 = -350.0
        adj_elect07 = 0.0
        adj_elect08 = 0.0
        adj_elect09 = 0.0
        adj_elect10 = 0.0

end


function segment.fast_adjust()

        if ion_time_of_flight < delay_time then
                adj_elect01 = 0.0

        elseif ion_time_of_flight > delay_time and ion_time_of_flight <
                (delay_time + turn_on_time) and not (turn_on_time == 0) then

                adj_elect01 = (pulse_voltage/turn_on_time)*(ion_time_of_flight - delay_time )

                --print(string.format(”Ion number %d     ToF = %d         Voltage =
                        --%d”,ion_number,( ion_time_of_flight * 10^3), adj_elect01 ) )

        elseif ion_time_of_flight <= (delay_time + pulse_length + turn_on_time) then
                adj_elect01 = pulse_voltage

        else
                adj_elect01 = 0.0
        end

end


function segment.other_actions()
--      sim_update_pe_surface = 1

        --if ion_px_mm >= 144.9 and not (ion_splat == 0) then
                --print(string.format(”Ion number %d ToF = %d”,ion_number,
                        --( (ion_time_of_flight - delay_time) * 10^3) ) )
        --end

        --if ion_time_of_flight <  delay_time then
        --      ion_color = 0
        --elseif ion_time_of_flight < (delay_time + pulse_length) then
        --      ion_color = 1
        --else
        --      ion_color = 3
        --end

        if ion_splat ~= 0 then
                --print(string.format(”Particle (ion) number %d ToF =
                        --%06.4d”,ion_number,(ion_time_of_flight * 10^3) ) )


                local vx = ion_vx_mm * (1/1000) * ( 1/( 10^(-6) ) ) -- convert to SI
                local vy = ion_vy_mm * (1/1000) * ( 1/( 10^(-6) ) ) -- convert to SI
```

```
                local vz = ion_vz_mm * (1/1000) * ( 1/( 10^(-6) ) ) -- convert to SI

                if Excel_Plot_True1_False0 == 1 then
                        Ion_count = Ion_count + 1
                        ws2.Cells(Ion_count,8).Value2 = -ion_px_mm
                        ws2.Cells(Ion_count,9).Value2 = -ion_py_mm
                        ws2.Cells(Ion_count,10).Value2 = -ion_pz_mm
                        ws2.Cells(Ion_count,11).Value2 = sqrt(ion_mass)
                        ws2.Cells(Ion_count,14).Value2 = ion_time_of_flight * 10^3
                        ws2.Cells(Ion_count,13).Value2 = (ion_py_mm ^2 + ion_pz_mm^2)^(0.5)
                        ws2.Cells(Ion_count,12).Value2 = 0.5*(ion_mass * 1.660538782e-27 )*
                        (vx^2 + vy^2 + vz^2) * 1.0/(1.602176487e-19) -- in eV

                end
        end
end


-- SIMION terminate segment.
function segment.terminate()


   if ion_number == 1 and Excel_Plot_True1_False0 == 1 then  -- only do this once

                -- Create Excel chart for Ion Wiggles-----------------------------------------
                local chart2 = excel.Charts:Add()
                chart2.ChartType = -4169  -- scatter XY

                local xlColumns = 2
                local endletter = string.char(string.byte’N’ + 2 - 1)
                chart2:SetSourceData(ws2:Range(”N2”, endletter .. Ion_count), xlColumns)

                -- Set labels / formatting.
                -- chart.PlotArea.Interior.Color = 0xffffff  -- white (RGB)
                chart2.HasLegend = 0
                chart2.HasTitle = 1
                chart2.ChartTitle:Characters().Text = ”X Mom. vs. TOF”
                chart2.Axes(1,1).HasTitle = 1
                chart2.Axes(1,1).AxisTitle:Characters().Text = ”Tof ns”
                chart2.Axes(1,2).HasTitle = 1
                chart2.Axes(1,2).AxisTitle:Characters().Text = ”initial X Mom.”

                excel.Visible = true

                wb.Saved = true  -- don’t ask to save on close
        end

        sim_retain_changed_potentials = 1
end
```

Bibliography

[1] S. M. Pimblott and J. A. LaVerne. Production of low-energy electrons by ionizing radiation. *Rad. Phys. and Chem.*, 76(8):1244–1247, 2007.

[2] C. R. Arumainayagam, H. L. Lee, R. B. Nelson, D. R. Haines, and R. P. Gunawardane. Low-energy electron-induced reactions in condensed matter. *Surf. Sci. Rep.*, 65(1):1–44, 2010.

[3] A. Küller, W. Eck, V. Stadler, W. Geyer, and A. Gölzhäuser. Nanostructuring of silicon by electron-beam lithography of self-assembled hydroxybiphenyl monolayers. *App. Phys. Lett.*, 82(21):3776–3778, 2003.

[4] S. J. Randolph, J. D. Fowlkes, and P. D. Rack. Focused electron-beam-induced etching of silicon dioxide. *J. App. Phys.*, 98(3):034902, 2005.

[5] V. Vijayabaskar, S. Bhattacharya, V. K. Tikku, and A. K. Bhowmick. Electron beam initiated modification of acrylic elastomer in presence of polyfunctional monomers. *Rad. Phys. and Chem.*, 71(5):1045–1058, 2004.

[6] I. Banik and A. K. Bhowmick. Influence of electron beam irradiation on the mechanical properties and crosslinking of fluorocarbon elastomer. *Rad. Phys. and Chem.*, 54(2):135–142, 1999.

[7] S. Massey, P. Cloutier, L. Sanche, and D. Roy. Mass spectrometry investigation of the degradation of polyethylene terephtalate induced by low-energy (<100 eV) electrons. *Rad. Phys. and Chem.*, 77(7):889–897, 2008.

[8] J. Xu, W. J. Choyke, and J. T. Yates, Jr. Enhanced silicon oxide film growth on Si (100) using electron impact. *J. App. Phys.*, 82(12):6289–6292, 1997.

[9] S. F. Bent. Attaching organic layers to semiconductor surfaces. *J. Phys. Chem. B*, 106(11):2830–2842, 2002.

[10] Z. Ma and F. Zaera. Organic chemistry on solid surfaces. *Surf. Sci. Rep.*, 61(5):229–281, 2006.

[11] A. Lafosse, M. Bertin, A. Domaracka, D. Pliszka, E. Illenberger, and R. Azria. Reactivity induced at 25 K by low-energy electron irradiation of condensed NH_3–CH_3COOD (1:1) mixture. *Phys. Chem. Chem. Phys.*, 8(47):5564–5568, 2006.

[12] S. Solovev, A. Palmentieri, N. D. Potekhina, and T. E. Madey. Mechanism for electron-induced SF_5CF_3 formation in condensed molecular films. *J. Phys. Chem. C*, 111(49):18271–18278, 2007.

[13] T. W. Marin, C. D. Jonah, and D. M. Bartels. Reaction of OH^* radicals with H_2 in sub-critical water. *Chem. Phys. Lett.*, 371(12):144–149, 2003.

[14] D. Meisel, D. M. Camaioni, and T. M. Orlando. Radiation and chemistry in nuclear waste: The NO_x system and organic aging. In *ACS Symposium Series*, volume 778, pages 342–363. ACS Publications, 2001.

[15] Q. B. Lu and T. E. Madey. Giant enhancement of electron-induced dissociation of chlorofluorocarbons coadsorbed with water or ammonia ices: Implications for atmospheric ozone depletion. *J. Chem. Phys.*, 111:2861, 1999.

[16] Q. B. Lu and L. Sanche. Effects of cosmic rays on atmospheric chlorofluorocarbon dissociation and ozone depletion. *Phys. Rev. Lett.*, 87:078501, 2001.

[17] N. R. P. Harris, J. C. Farman, and D. W. Fahey. Comment on "effects of cosmic rays on atmospheric chlorofluorocarbon dissociation and ozone depletion". *Phys. Rev. Lett.*, 89:219801, 2002.

[18] Q. B. Lu. Correlation between cosmic rays and ozone depletion. *Phys. Rev. Lett.*, 102:118501, 2009.

[19] W. T. Sturges, T. J. Wallington, M. D. Hurley, K. P. Shine, K. Sihra, A. Engel, D. E. Oram, S. A. Penkett, R. Mulvaney, and C. A. M. Brenninkmeijer. A potent greenhouse gas identified in the atmosphere: SF_5CF_3. *Science*, 289(5479):611–613, 2000.

[20] Y. Zheng, P. Cloutier, D. J. Hunting, J. R. Wagner, and L. Sanche. Phosphodiester and N-glycosidic bond cleavage in DNA induced by 4–15 eV electrons. *J. Chem. Phys.*, 124:064710, 2006.

[21] B. Boudaïffa, P. Cloutier, D. Hunting, M. A. Huels, and L. Sanche. Resonant formation of DNA strand breaks by low-energy (3 to 20 eV) electrons. *Science*, 287(5458):1658–1660, 2000.

[22] B. Boudaïffa, P. Cloutier, D. Hunting, M. A. Huels, and L. Sanche. Cross sections for low-energy (10–50 eV) electron damage to DNA. *Radiation Research*, 157(3):227–234, 2002.

[23] F. Martin, P. D. Burrow, Z. Cai, P. Cloutier, D. Hunting, and L. Sanche. DNA strand breaks induced by 0–4 eV electrons: The role of shape resonances. *Phys. Rev. Lett.*, 93:068101, 2004.

[24] R. Barrios, P. Skurski, and J. Simons. Mechanism for damage to DNA by low-energy electrons. *J. Phys. Chem. B*, 106(33):7991–7994, 2002.

[25] J. Berdys, P. Skurski, and J. Simons. Damage to model DNA fragments by 0.25–1.0 eV electrons attached to a thymine π^* orbital. *J. Phys. Chem. B*, 108(18):5800–5805, 2004.

[26] J. Berdys, I. Anusiewicz, P. Skurski, and J. Simons. Theoretical study of damage to DNA by 0.2–1.5 eV electrons attached to cytosine. *J. Phys. Chem. A*, 108(15):2999–3005, 2004.

[27] X. Pan, P. Cloutier, D. Hunting, and L. Sanche. Dissociative electron attachment to DNA. *Phys. Rev. Lett.*, 90:208102, 2003.

[28] X. Pan and L. Sanche. Mechanism and site of attack for direct damage to dna by low-energy electrons. *Phys. Rev. Lett.*, 94:198104, 2005.

[29] S. Ptasińska and L. Sanche. Dissociative electron attachment to hydrated single DNA strands. *Phys. Rev. E*, 75:031915, 2007.

[30] S. Ptasińska and L. Sanche. Dissociative electron attachment to abasic DNA. *Phys. Chem. Chem. Phys.*, 9(14):1730–1735, 2007.

[31] L. Sanche. Low energy electron-driven damage in biomolecules. *The European Physical Journal D-Atomic, Molecular, Optical and Plasma Physics*, 35(2):367–390, 2005.

[32] H. Abdoul-Carime, S. Gohlke, and E. Illenberger. Site-specific dissociation of DNA bases by slow electrons at early stages of irradiation. *Phys. Rev. Lett.*, 92:168103, 2004.

[33] J. Gu, J. Wang, and J. Leszczynski. Electron attachment-induced DNA single-strand breaks at the pyrimidine sites. *Nucleic Acids Research*, 38(16):5280–5290, 2010.

[34] G. Hanel, B. Gstir, S. Denifl, P. Scheier, M. Probst, B. Farizon, M. Farizon, E. Illenberger, and T. D. Märk. Electron attachment to uracil: Effective destruction at subexcitation energies. *Phys. Rev. Lett.*, 90:188104, May 2003.

[35] Y. Zheng, P. Cloutier, J. Darel, L. Sanche, and J. R. Wagner. Chemical basis of DNA sugar-phosphate cleavage by low-energy electrons. *Journal of the American Chemical Society*, 127(47):16592–16598, 2005.

[36] Y. Zheng, D. J. Hunting, P. Ayotte, and L. Sanche. Role of secondary low-energy electrons in the concomitant chemoradiation therapy of cancer. *Phys. Rev. Lett.*, 100:198101, 2008.

[37] J. Berdys, I. Anusiewicz, P. Skurski, and J. Simons. Damage to model DNA fragments from very low-energy (<1 eV) electrons. *Journal of the American Chemical Society*, 126(20):6441–6447, 2004.

[38] P. W. B. Poon, P. Y. Y. Wong, P. Dubeski, T. D. Durance, and D. D. Kitts. Application of electron-beam irradiation pasteurization of ground beef, from steers fed vitamin E fortified diets: microbial and chemical effects. *Journal of the Science of Food and Agriculture*, 83(6):542–549, 2003.

[39] P. A. Smith, M. V. Sheely, S. J. Hakspiel, and S. Miller. Volatile organic compounds produced during irradiation of mail. *AIHA Journal*, 64(2):189–195, 2003.

[40] M. A. Huels, L. Parenteau, A. D. Bass, and L. Sanche. Small steps on the slippery road to life: Molecular synthesis in astrophysical ices initiated by low energy electron impact. *International Journal of Mass Spectrometry*, 277(1):256–261, 2008.

[41] V. Vuitton, P. Lavvas, R. V. Yelle, M. Galand, A. Wellbrock, G. R. Lewis, A. J. Coates, and J. E. Wahlund. Negative ion chemistry in Titan's upper atmosphere. *Planetary and Space Science*, 57(13):1558–1572, 2009.

[42] B. H. Bransden and C. H. Joachain. *Physics of Atoms and Molecules.* Pearson Education, Essex, 2nd edition, 2003.

[43] H. Haken and H. C. Wolf. *Molecular Physics and Elements of Quantum Chemistry.* Springer-Verlag, Berlin, 2nd edition, 2004.

[44] J. L. McHale. *Molecular Spectroscopy.* Prentice-Hall, New Jersey, 1st edition, 1999.

[45] D. J. Willock. *Molecular Symmetry.* John Wiley & Sons, 1st edition, 2009.

[46] S. F. A. Kettle. *Symmetry and Structure.* John Wiley & Sons, 1st edition, 1985.

[47] H. Deutsch, K. Becker, S. Matt, and T. D. Märk. Theoretical determination of absolute electron-impact ionization cross sections of molecules. *International Journal of Mass Spectrometry*, 197(1):37–69, 2000.

[48] G. A. Kimmel and T. M. Orlando. Low-energy (5–120 eV) electron-stimulated dissociation of amorphous D_2O ice: $D(^2S)$, $O(^3P_{2,1,0})$, and $O(^1D_2)$ yields and velocity distributions. *Phys. Rev. Lett.*, 75:2606–2609, 1995.

[49] N. Getoff, A. Ritter, F. Schwörer, and P. Bayer. Primary yields of CH_3O and CH_2OH radicals resulting in the radiolysis of high purity methanol. *Rad. Phys. and Chem.*, 41(6):797–801, 1993.

[50] H. Sambe, D. E. Ramaker, L. Parenteau, and L. Sanche. Image charge effects in electron stimulated desorption: O^- from O_2 condensed on Ar films grown on Pt. *Phys. Rev. Lett.*, 59:236–239, 1987.

[51] D. Nandi, V. S. Prabhudesai, and E. Krishnakumar. Velocity Map Imaging for Low-Energy Electron-Molecule Collisions. *Rad. Phys. and Chem.*, 75(12):2151–2158, 2006.

[52] C. von Ramsauer and R. Kollath. Über den wirkungsquerschnitt der nichtedelgasmoleküle gegenüber elektronen unterhalb 1 volt. *Annalen der Physik*, 396(1):91–108, 1930.

[53] R. E. Olson, J. Ullrich, and H. Schmidt-Bocking. Dynamics of multiply charged ion-atom collisions: U_{32}^{+} + Ne. *J. Phys. B*, 20(23):L809, 1987.

[54] R. Dörner, V. Mergel, L. Spielberger, M. Achler, K. Khayyat, T. Vogt, H. Bräuning, O. Jagutzki, T. Weber, and J. et al. Ullrich. Kinematically complete experiments using cold target recoil ion momentum spectroscopy. *Nuclear Instruments and Methods in Physics Research Section B: Beam Interactions with Materials and Atoms*, 124(2):225–231, 1997.

[55] A. Gensmantel, J. Ullrich, R. Dörner, R. E. Olson, K. Ullmann, E. Forberich, S. Lencinas, and H. Schmidt-Böcking. Dynamic mechanisms of He single ionization by fast proton impact. *Phys. Rev. A*, 45(7):4572, 1992.

[56] R. Dörner, V. Mergel, O. Jagutzki, L. Spielberger, J. Ullrich, R. Moshammer, and H. Schmidt-Böcking. Cold target recoil ion momentum spectroscopy: a momentum microscope to view atomic collision dynamics. *Phys. Rep.*, 330(23):95–192, 2000.

[57] V. Frohne, S. Cheng, R. Ali, M. Raphaelian, C. L. Cocke, and R. E. Olson. Measurements of recoil ion longitudinal momentum transfer in multiply ionizing collisions of fast heavy ions with multielectron targets. *Phys. Rev. Lett.*, 71(5):696–699, 1993.

[58] R. Dörner, V. Mergel, R. Ali, U. Buck, C. L. Cocke, K. Froschauer, O. Jagutzki, S. Lencinas, W. E. Meyerhof, and S. et al. Nüttgens. Electron-electron interaction in projectile ionization investigated by high resolution recoil ion momentum spectroscopy. *Phys. Rev. Lett.*, 72(20):3166–3169, 1994.

[59] W. C. Wiley and I. H. McLaren. Time of flight mass spectrometer with improved resolution. *Rev. Sci. Instrum.*, 26(12):1150 –1157, 1955.

[60] A. T. J. B. Eppink and D. H. Parker. Velocity map imaging of ions and electrons using electrostatic lenses: Application in photoelectron and photofragment ion imaging of molecular oxygen. *Rev. Sci. Instrum.*, 68(9):3477–3484, 1997.

[61] D. H. Parker and A. T. J. B. Eppink. Photoelectron and photofragment velocity map imaging of state-selected molecular oxygen dissociation/ionization dynamics. *J. Chem. Phys.*, 107:2357, 1997.

[62] M. Ahmed, D. S. Peterka, and A. G. Suits. Crossed-beam reaction of $O(^1D) + D_2 \rightarrow OD + D$ by velocity map imaging. *Chem. Phys. Lett.*, 301(3):372–378, 1999.

[63] J. Wei, A. Kuczmann, J. Riedel, F. Renth, and F. Temps. Photofragment velocity map imaging of H atom elimination in the first excited state of pyrrole. *Phys. Chem. Chem. Phys.*, 5(2):315–320, 2003.

[64] C. R. Gebhardt. Slice Imaging: A New Approach to Ion Imaging and Velocity Mapping. *Rev. Sci. Instrum.*, 72(10):3848–3853, 2001.

[65] V. Papadakis and T. N. Kitsopoulos. Slice imaging and velocity mapping using a single field. *Rev. Sci. Instrum.*, 77(8):083101, 2006.

[66] D. Nandi, V. S. Prabhudesai, E. Krishnakumar, and A. Chatterjee. Velocity Slice Imaging for Dissociative Electron Attachment. *Rev. Sci. Instrum.*, 76(5):053107, 2005.

[67] B. Wu, L. Xia, H. K. Li, X. J. Zeng, and S. X. Tian. Positive/negative ion velocity mapping apparatus for electron-molecule reactions. *Rev. Sci. Instrum.*, 83(1):013108, 2012.

[68] A. Moradmand, J. B. Williams, A. L. Landers, and M. Fogle. Momentum-imaging apparatus for the study of dissociative electron attachment dynamics. *Rev. Sci. Instrum.*, 84:033104, 2013.

[69] A Czasch, L Ph H Schmidt, T Jahnke, Th Weber, O Jagutzki, S Schössler, MS Schöffler, R Dörner, and H Schmidt-Böcking. Photo induced multiple fragmentation of atoms and molecules: Dynamics of coulombic many-particle systems studied with the coltrims reaction microscope. *Physics Letters A*, 347(1):95–102, 2005.

[70] Th Ergler, A Rudenko, B Feuerstein, K Zrost, CD Schröter, R Moshammer, and J Ullrich. Time-resolved imaging and manipulation of h_ {2} fragmentation in intense laser fields. *Physical review letters*, 95(9):093001, 2005.

[71] R Moshammer, J Ullrich, B Feuerstein, D Fischer, A Dorn, CD Schröter, JR Crespo López-Urrutia, C Höhr, H Rottke, C Trump, et al. Strongly directed electron emission in non-sequential double ionization of ne by intense laser pulses. *Journal of Physics B: Atomic, Molecular and Optical Physics*, 36(6):L113, 2003.

[72] N. Yoshimura. *Vacuum Technology.* Springer Publishing, 2008.

[73] J. R. Buckland, R. L. Folkerts, R. B. Balsod, and W. Allison. A simple nozzle design for high speed-ratio molecular beams. *Meas. Sci. Technol.*, 8:933, 1997.

[74] R. Campargue. Progress in overexpanded supersonic jets and skimmed molecular beams in free-jet zones of silence. *J. Phys. Chem.*, 88(20):4466–4474, 1984.

[75] H. R. Murphy and D. R. Miller. Effects of Nozzle Geometry on Kinetics in Free-Jet Expansions. *J. Phys. Chem.*, 88(20):4474–4478, 1984.

[76] Hans Pauly. *Atom, Molecule, and Cluster Beams II: Cluster Beams, Fast and Slow Beams, Accessory Equipment and Applications*, volume 1. Springer, 2000.

[77] F. Rademakers. ROOT v2.24/05, 1994–2012.

[78] A. Czasch, T. Jahnke, and M. Shoeffler. LMF2Root v1.6, 2008–2013.

[79] Roentdek Handels GmbH. Cobold PC 2008, 2008–2012.

[80] H. F. Winters. Dissociation of methane by electron impact. *The Journal of Chemical Physics*, 63:3462, 1975.

[81] S. Motlagh and J. H. Moore. Cross sections for radicals from electron impact on methane and fluoroalkanes. *J. Chem. Phys.*, 109:432, 1998.

[82] O. J. Orient and S. K. Strivastava. Electron impact ionisation of H_2O, CO, CO_2 and CH_4. *J. Phys. B*, 20(15):3923, 1987.

[83] G. H. Dunn. Anisotropies in Angular Distributions of Molecular Dissociation Products. *Phys. Rev. Lett.*, 8:62–64, 1962.

[84] C. J. Noble, K. Higgins, G. Wöste, P. Duddy, P. G. Burke, P. J. O. Teubner, A. G. Middleton, and M. J. Brunger. Resonant mechanisms in the vibrational excitation of ground state O_2. *Phys. Rev. Lett.*, 76:3534–3537, 1996.

[85] V. S. Prabhudesai, D. Nandi, and E. Krishnakumar. On the presence of the ${}^4\sigma_u^-$ resonance in dissociative electron attachment to O_2. *J. Phys. B*, 39(14):L277, 2006.

[86] R. J. Van Brunt and L. J. Kieffer. Angular distribution of O^- from dissociative electron attachment to O_2. *Phys. Rev. A*, 2:1899–1905, 1970.

[87] T. F. O'Malley and H. S. Taylor. Angular dependence of scattering products in electron-molecule resonant excitation and in dissociative attachment. *Phys. Rev.*, 176:207–221, 1968.

[88] A. Moradmand, D. S. Slaughter, A. L. Landers, and M. Fogle. Dissociative electron attachment dynamics near the 8 eV feshbach resonance of CO_2 (in prep.). 2013.

[89] A. Stamatovic and G. J. Schulz. Characteristics of the trochoidal electron monochromator. *Rev. Sci. Instrum.*, 41(3):423–427, 1970.

[90] D. Rapp and D. D. Briglia. Total cross sections for ionization and attachment in gases by electron impact. ii. negative-ion formation. *J. Chem. Phys.*, 43(5):1480–1489, 1965.

[91] R. Abouaf, R. Paineau, and F. Fiquet-Fayard. Dissociative attachment in NO_2 and CO_2. *J. Phys. B*, 9(2):303, 2001.

[92] M. Tronc, L. Malegat, and R. Azria. Zero kinetic energy ions in dissociative attachment on triatomic molecules: S/ocs, o/co2. *Chem. Phys. Lett.*, 92(5):551–555, 1982.

[93] S. K. Srivastava and O. J. Orient. Double e-beam technique for collision studies from excited states: Application to vibrationally excited CO_2. *Phys. Rev. A*, 27:1209–1212, 1983.

[94] C. R. Claydon, G. A. Segal, and H. S. Taylor. Theoretical interpretation of the electron scattering spectrum of CO_2. *J. Chem. Phys.*, 52(7):3387–3398, 1970.

[95] P. J. Chantry. Dissociative attachment in carbon dioxide. *J. Chem. Phys.*, 57(8):3180–3186, 1972.

[96] R. Dressler and M. Allan. Energy partitioning in the O^-/CO_2 dissociative attachment. *Chem. Phys.*, 92(23):449–455, 1985.

[97] H. Adaniya, D. S. Slaughter, T. Osipov, T. Weber, and A. Belkacem. A momentum imaging microscope for dissociative electron attachment. *Rev. Sci. Instrum.*, 83(2):023106, 2012.

[98] M. Sizun and S. Goursaud. A classical trajectory study of the fragmentation of CO_2^- Σ_g^+. *J. Chem. Phys.*, 71(10):4042–4049, 1979.

[99] M. A. Huels, L. Parenteau, P. Cloutier, and L. Sanche. Electron stimulated desorption of O^- and metastable CO^* from physisorbed CO_2. *J. Chem. Phys.*, 103(15):6775–6782, 1995.

[100] D. S. Slaughter, H. Adaniya, T. N. Rescigno, D. J. Haxton, A. E. Orel, C. W. McCurdy, and A. Belkacem. Dissociative electron attachment to carbon dioxide via the 8.2 eV feshbach resonance. *J. Phys. B.*, 44:205203, 2012.

[101] B. Wu, L. Xia, Y. F. Wang, H. K. Li, X. J. Zeng, and S. X. Tian. Renner-teller effect on dissociative electron attachment to carbon dioxide. *Phys. Rev. A*, 85(5):052709, 2012.

[102] M. J. W. Boness and G. J. Schulz. Vibrational excitation in CO_2 via the 3.8 eV resonance. *Phys. Rev. A*, 9:1969–1979, 1974.

[103] C. W. McCurdy, W. A. Isaacs, H.-D. Meyer, and T. N. Rescigno. Resonant vibrational excitation of co_2 by electron impact: Nuclear dynamics on the coupled components of the $^2\pi_u$ resonance. *Phys. Rev. A*, 67:042708, 2003.

[104] W. Vanroose, Z. Zhang, C. W. McCurdy, and T. N. Rescigno. Threshold vibrational excitation of CO_2 by slow electrons. *Phys. Rev. Lett.*, 92:053201, 2004.

[105] M. Allan. Vibrational structures in electron–CO_2 scattering below the $^2\Pi_u$ shape resonance. *J. Phys. B*, 35(17):L387, 2002.

[106] A. Moradmand, D. S. Slaughter, D. J. Haxton, A. L. Landers, C. W. McCurdy, T. N. Rescigno, M. Fogle, and A. Belkacem. Dissociative electron attachment to carbon dioxide via the $^2\Pi_u$ shape resonance (submitted). *Phys. Rev. A*, 2013.

[107] D. J. Haxton, C. W. McCurdy, and T. N. Rescigno. Angular dependence of dissociative electron attachment to polyatomic molecules: Application to the $^2B_1$ metastable state of the H_2O and H_2S anions. *Phys. Rev. A*, 73(6):062724, 2006.

[108] H. U. Suter and T. Greber. On the dissociation of N_2O after electron attachment. *J. Phys. Chem.*, 108(38):14511–14517, 2004.

[109] L. G. Christophorou, D. L. McCorkle, and A. A. Christodoulides. Electron-attachment processes. *Electron-Molecule Interactions and Their Applications*, 1, 1982.

[110] P. J. Chantry. Temperature dependence of dissociative attachment in NO. *J. Chem. Phys.*, 51:3369, 1969.

[111] JN Bardsley. Negative ions of N_2O and C_2O. *The Journal of Chemical Physics*, 51:3384, 1969.

[112] M. Tronc, F. Fiquet-Fayard, C. Schermann, and R. I. Hall. Angular distributions of O^- from dissociative electron attachment to N_2O between 1.9 to 2.9 eV. *J. Phys. B*, 10(12):L459, 1977.

[113] L. Xia, B. Wu, H.-K. Li, X.-J. Zeng, and S. X. Tian. Communication: Imaging the indirect dissociation dynamics of temporary negative ion: $N_2O \rightarrow N_2 + O^-$. *J. Chem. Phys.*, 137:151102, 2012.

[114] M. Allan and T. Skalický. Structures in elastic, vibrational, and dissociative electron attachment cross sections in N_2O near threshold. *J. Phys. B*, 36(16):3397, 2003.

[115] S. T. Chourou and A. E. Orel. Dissociative electron attachment to acetylene. *Phys. Rev. A*, 77:042709, 2008.

[116] O. May, J. Fedor, B. C. Ibănescu, and M. Allan. Absolute cross sections for dissociative electron attachment to acetylene and diacetylene. *Phys. Rev. A*, 77:040701, 2008.

[117] O. May, J. Fedor, and M. Allan. Isotope effect in dissociative electron attachment to acetylene. *Phys. Rev. A*, 80(1):012706, 2009.

[118] H. J. Saleh and A. J. McCaffery. Alignment of diatomic molecules in a free-jet expansion. *J. Chem. Soc., Faraday Trans.*, 89(17):3217–3221, 1993.

[119] V. Aquilanti, D. Ascenzi, M. de Castro Vitores, F. Pirani, and D. Cappelletti. A quantum mechanical view of molecular alignment and cooling in seeded supersonic expansions. *J. Chem. Phys.*, 111:2620, 1999.

[120] T. N. Rescigno, C. S. Trevisan, and A. E. Orel. Dynamics of low-energy electron attachment to formic acid. *Phys. Rev. Lett.*, 96(21):213201, 2006.

[121] G. A. Gallup, P. D. Burrow, and I. I. Fabrikant. Electron-induced bond breaking at low energies in HCOOH and glycine: The role of very short-lived Σ anion states. *Phys. Rev. A*, 79(4):042701, 2009.

[122] T. N. Rescigno, C. S. Trevisan, and A. E. Orel. Comment on “electron-induced bond breaking at low energies in HCOOH and glycine: The role of very short-lived Σ^* anion states”. *Phys. Rev. A*, 80:046701, 2009.

[123] G. A. Gallup, P. Burrow, and I. I. Fabrikant. Reply to comment on ”electron-induced bond breaking at low energies in HCOOH and glycine: The role of very short-lived Σ^* anion states”. *Phys. Rev. A*, 80:046702, 2009.

Index